Title
Highly Active Yeast MnSOD has a Novel Mechanism Involving Six-coordinate Mn(3+) Species

Author
Sheng, Yuewei

Publication Date
2012

Peer reviewed|Thesis/dissertation

UNIVERSITY OF CALIFORNIA

Los Angeles

Highly Active Yeast MnSOD has a Novel Mechanism Involving Six-coordinate Mn(3+) Species

A dissertation submitted in partial satisfaction of the

Requirements for the degree Doctor of Philosophy

in Chemistry

by

Yuewei Sheng

2012

ABSTRACT OF THE DISSERTATION

Highly Active Yeast MnSOD has a Novel Mechanism

Involving Six-coordinate Mn(3+) Species

by

Yuewei Sheng

Doctor of Philosophy in Chemistry

University of California, Los Angeles, 2012

Professor Joan Selverstone Valentine, Chair

Manganese-bound superoxide dismutase (MnSOD) is a very important antioxidant enzyme. The mechanism by which MnSOD removes O_2^- involves product inhibition, that is, reduction of O_2^- occurs through either a "prompt protonation" pathway, or an "inner-sphere" pathway, with the latter leading to formation of an observable Mn-peroxo complex. Human MnSOD is more gated toward the "inner-sphere" pathway than bacterial enzymes.

To study whether product inhibition is a common feature to eukaryotic MnSODs, we studied a mitochondrial MnSOD from the eukaryote model organism *Saccharomyces cerevisiae* (*Sc*MnSOD). To our surprise, *Sc*MnSOD was found to display the highest catalytic efficiency at high levels of O_2^- among MnSODs that had been characterized. To understand further the mechanism of product inhibition, we compared *Sc*MnSOD with another yeast MnSOD, the cytosolic MnSOD from *Candida albicans* (*Ca*MnSODc). *Ca*MnSODc, like *Sc*MnSOD, is less inhibited than human and bacterial MnSODs. Although the active site of yeast MnSODs closely

resembles that of MnSODs from other organisms, spectroscopic studies suggest the presence of a six-coordinate Mn^{3+} species in oxidized yeast MnSODs.

To explore further the origin of the fast catalysis by yeast MnSODs, the Y34F (a strictly conserved second-sphere residue) form of *Sc*MnSOD was created. Y34F *Sc*MnSOD has a novel catalytic mechanism, in which protonation of the Mn-peroxo complex occurs through a fast pathway at neutral pH, leading to a putative six-coordinate Mn^{3+} species, which actively oxidizes O_2^- in the catalytic cycle. Because wild-type and the mutant yeast MnSOD both rest in the 2+ state and become six-coordinate when oxidized up from Mn^{2+}, six-coordinate Mn^{3+} species could also actively function in the mechanism of wild-type yeast MnSODs.

*Sc*MnSOD is a tetramer, while *Ca*MnSODc is a dimer or loose tetramer, even though they are similar in many ways. Investigations of their crystal structures suggest that when *Ca*MnSODc is in the dimeric form, its N-terminal regions are highly disordered, hindering it from forming a tetramer in solution. To further investigate the physiological significance of the tetramer structure, we mutated two residues (Lys182/Ala183 in *Sc*MnSOD, Lys184/Leu185 in *Ca*MnSODc) at the dimer interface in the two yeast MnSODs. We find that the dimer interface, which is critical for MnSOD activity, is reinforced by tetramer formation.

The dissertation of Yuewei Sheng is approved.

_____

James U. Bowie

_____

Robert P. Gunsalus

_____

Joan Selverstone Valentine, Committee Chair

University of California, Los Angeles

2012

Table of Contents

List of Figures

Lists of Tables

Acknowledgements

I would like to express my sincere gratitude to my supervisor Professor Joan Selverstone Valentine. I studied Chemistry when I was in college back in China, and I had very little experience in biochemistry when I came to UCLA five years ago. From the beginning, my supervisor had her confidence in me, and she took me as her last graduate student in her long, successful career. She opened the door toward an entirely novel and challenging science world that I had never experienced before. She passed her passion and insight toward science to me, and inspired me to explore the unknowns bravely and deeply. She is always very encouraging and optimistic. Without her constant support, I would not have gone through the stress and difficulties from life and research.

I would also like to thank Dr. Edith B. Gralla for her support and her aid in addressing every of my questions in biology. Edie is always very patient and willing to offer her help. Her enthusiasm and broad interests not only make me a better scientist, but also inspire me to have a better life. I would like to thank Prof. Julian Whitelegge for his supervision on the hydroxyl radical footprinting project.

I appreciate greatly the supervision from Prof. Diane E. Cabelli (Brookhaven National Laboratories) on my dissertation projects. Diane not only has spent tremendous amounts of time and effort on helping me with the pulse radiolysis experiments, but also took great care of me every time I travelled to Brookhaven. I would like to thank Dr. Duilio Cascio (Department of Energy-Institute for Genomics and Proteomics, UCLA) for teaching me and giving me tremendous help in X-ray crystallography. I would like to thank Dr. Chris Ryan (Department of Psychiatry and Biobehavioral Sciences, UCLA) for training me on LC-MS and helping me address every difficulty I encountered when using mass spectrometer. I would like to thank Prof. R. David Britt and Dr. Troy A. Stich (University of California, Davis), for performing spectroscopic studies on my enzyme samples. I would like to thank Prof. Yi Tang, Dr. Zhen Gu and Dr. Yanran Li (Department of Chemical Engineering, UCLA) for our collaboration on several very interesting metalloenzyms that participate in the biosynthesis of natural products in fungi.

I also received a lot of help from my previous and present group members. I would like to particularly thank Dr. Kevin Barnese, who was my mentor when I joined the group. He gave me great guidance in how to express, purify and characterize proteins. What Kevin taught me has always been the fundamentals of my research in the following years. I would like to thank Mikhail Schumacher for helping me with protein purification. I would like to thank Dr. Armando Durazo for running my ICP-MS and LC-MS samples. I would like to thank Dr. Herman Lelie for training me on ICP-MS. I would like to thank Dr. Lindsay Kane and Dr. Jake Martins for helping me with cloning. I would like to thank Becky Chan for providing me protein samples for hydroxyl radical footprinting experiments.

Finally I would like especially to thank my dad, who raised me up and supports me from his heart all the time. I would like to thank my friends for their encouragement and support in the past five years.

VITA

2007	B. S., Chemistry, Nanjing University Nanjing, China
2010	M. S., Chemistry, University of California, Los Angeles Los Angeles, California

Work Experience

2008 – 2009	Teaching Assistant, UCLA
2009 – 2011	Teaching Associate, UCLA
2011	Grad Intern, Amgen Inc., Thousand Oaks, California

Awards

2011 – 2012	Dissertation Year Fellowship, UCLA
2011	John M. Jordan Memorial Award for Research in Biochemistry, UCLA
2012	Chinese Government Award for Outstanding Self-Financed Students Abroad

PUBLICATIONS

1. **Sheng, Yuewei**; Stich, Troy A.; Barnese, Kevin; Gralla, Edith B.; Britt, R. D.; Cascio, Duilio; Cabelli, Diane E.; Valentine, Joan S. Comparison of two yeast MnSODs: Mitochondrial *Saccharomyces cerevisiae* versus cytosolic *Candida albicans*. *J. Am. Chem. Soc.* **2011**, *133*, 20878-20889
2. **Sheng, Yuewei**; Gralla, Edith B.; Schumacher, Mikhail; Cascio, Duilio; Cabelli, Diane E.; Valentine, Joan S. Six-coordinate manganese(3+) in catalysis by yeast manganese superoxide dismutase. (submitted to PNAS)
3. **Sheng, Yuewei**; Schumacher, Mikhail; Armando Durazo, Gralla, Edith B.; Cascio, Duilio; Cabelli, Diane E.; Valentine, Joan S. Tetramerization in Yeast MnSOD and its Functional Significance (in preparation)
4. **Sheng, Yuewei**; Julian Whitelegge; Joan S. Valentine. SOD1 aggregation and ALS: role of metallation states and disulfide status. *Curr. Top. Med. Chem.* **2012** (invited review) (in preparation)
5. Li, Yanran; Chooi, Yit-Heng; **Sheng, Yuewei**; Valentine, Joan S.; Tang, Yi. Comparative characterization of fungal anthracenone and naphthacendione biosynthetic pathways reveals an α-hydroxylation-dependent Claisen-like cyclization catalyzed by a dimanganese thioesterase. *J. Am. Chem. Soc.* **2011**, *133*, 15773-15785
6. Gu, Zhen; Zhao, Muxun; **Sheng, Yuewei,** Bentolila, Laurent A.; Tang, Yi. Detection of mercury ion by infrared-fluorescent protein and its hydrogel-based paper assay. *Anal. Chem.* **2011**, *83*, 2324-2329
7. Barnese, Kevin; **Sheng, Yuewei (contributing equally)**; Stich, Troy A.; Gralla, Edith B.; Britt, R. David; Cabelli, Diane E.; Valentine, Joan Selverstone. Investigation of the highly active manganese superoxide dismutase from *Saccharomyces cerevisiae*. *J. Am. Chem. Soc.* **2010**, *132*, 12525-12527
8. Wang, Yan; **Sheng, Yue-Wei**; Sun, Wei-Yin. Synthesis and crystal structure of 1-bromo-3,5-bis(imidazol-1-ylmethyl)benzene-Cd(II) complexes with Br···π and Br···Br interactions. *Chin. J. Inorg. Chem.* **2009**, *25*, 1182-1186
9. Wang, Yan; Huang, Yong-Qing; Liu, Guang-Xiang; Okamura, Taka-aki; Doi, Mototsugu; **Sheng, Yue-Wei**; Sun, Wei-Yin; Ueyama, Norikazu. New metal-organic frameworks with large cavities: selective sorption and desorption of solvent molecules. *Chem. Eur. J.* **2007**, *13*, 7523-7531
10. **Sheng, Yue-Wei**; Wang, Yan; Okamura, Taka-aki; Sun, Wei-Yin; Ueyama, Norikazu. Synthesis, crystal structure, and nonlinear optical property of cadmium(II) and copper(II) complexes with novel chiral ligand. *Inorg. Chem. Commun.* **2007**, *10*, 432-436

Chapter 1

Introduction

Superoxide and Superoxide Dismutase

Superoxide (O_2^-) is generated in various in vivo processes through the attachment of a single electron to dioxygen. Mitochondrion is recognized as the major source for O_2^-, a byproduct of the respiratory chain (1). The reduction potential for the conversion of dioxygen to O_2^- is –0.16 V (2). Due to the highly reducing environment in the mitochondria, the one-electron reduction of dioxygen is thermodynamically favorable for numerous respiratory components. Even though O_2^- is not a strong oxidant, it is a precursor of most other reactive oxygen species (ROS), such as hydrogen peroxide (H_2O_2) and hydroxyl radical ($^{\bullet}OH$). Only several proteins containing [Fe–S] clusters, including aconitase, dehydrases, and fumarases, have been identified as targets for O_2^- reactivity in vivo.

Scheme 1.1. The Dismutase Mechanism

$$M^{n+} + O_2^- \rightarrow M^{(n-1)+} + O_2$$

$$M^{(n-1)+} + O_2^- + 2H^+ \rightarrow M^{n+} + H_2O_2$$

Superoxide dismutases (SODs) are enzymes that function to convert the superoxide (O_2^-) anion to dioxygen and hydrogen peroxide (H_2O_2) catalytically via sequential reduction and oxidation of a metal cofactor at virtually diffusion-controlled rate constants (Scheme 1.1). Based on the active-site metal, SODs are classified into copper-zinc SOD (CuZnSOD), nickel SOD (NiSOD), manganese SOD (MnSOD), and iron SOD (FeSOD). NiSOD is only found in prokaryotes. In eukaryotes CuZnSOD is located in the cytosol, nucleus, peroxisomes, mitochondrial intermembrane space, and extracellular space (3), while MnSOD is in

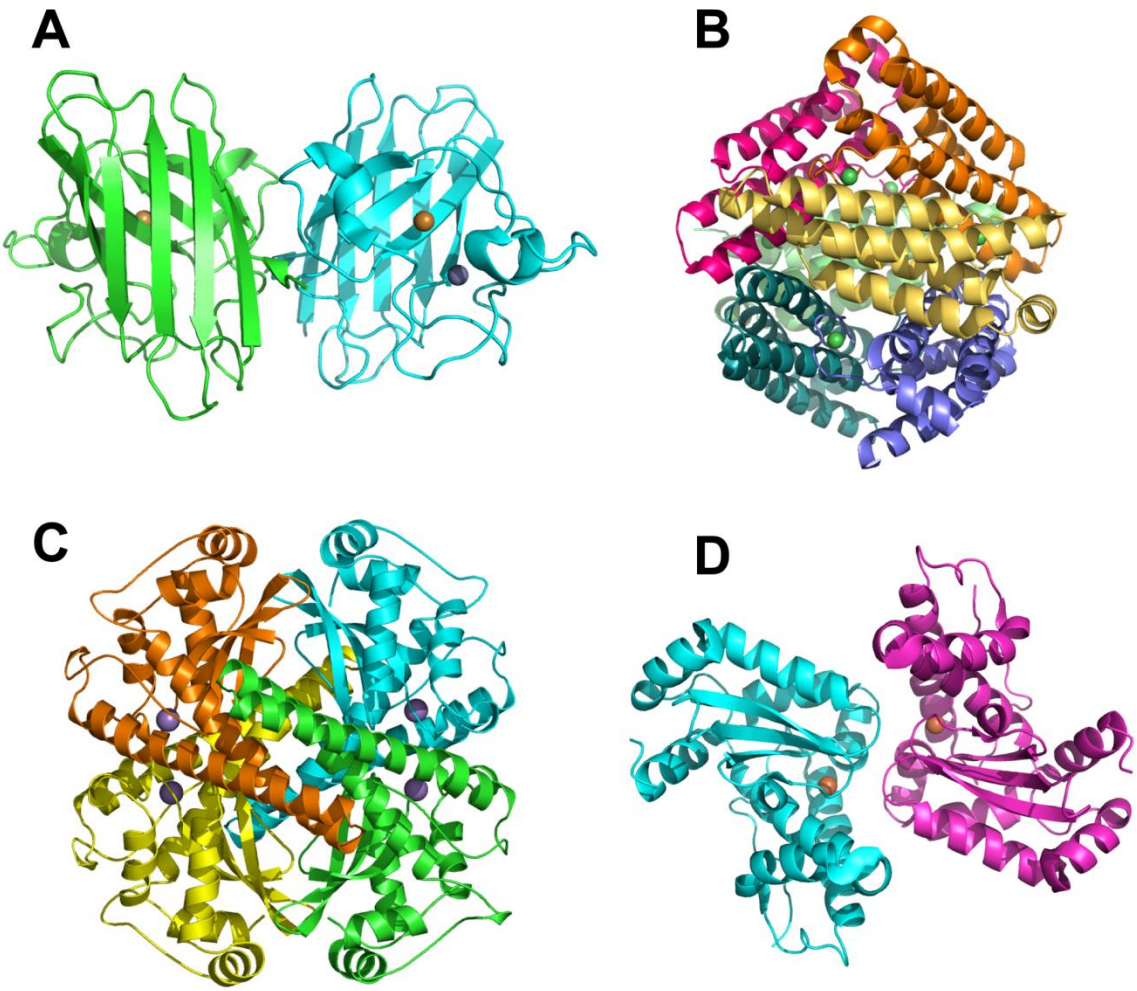

Figure 1.1. The enzyme structures of four classes of SOD. (A) *Homo sapien* CuZnSOD (pdb code: 1PU0); (B) *Streptomyces coelicolor* NiSOD (pdb code: 1T6U); (C) *Saccharomyces cerevisiae* MnSOD (pdb code: 3LSU); (D) *Anaplasma phagocytophilum* FeSOD (pdb code: 3JS4).

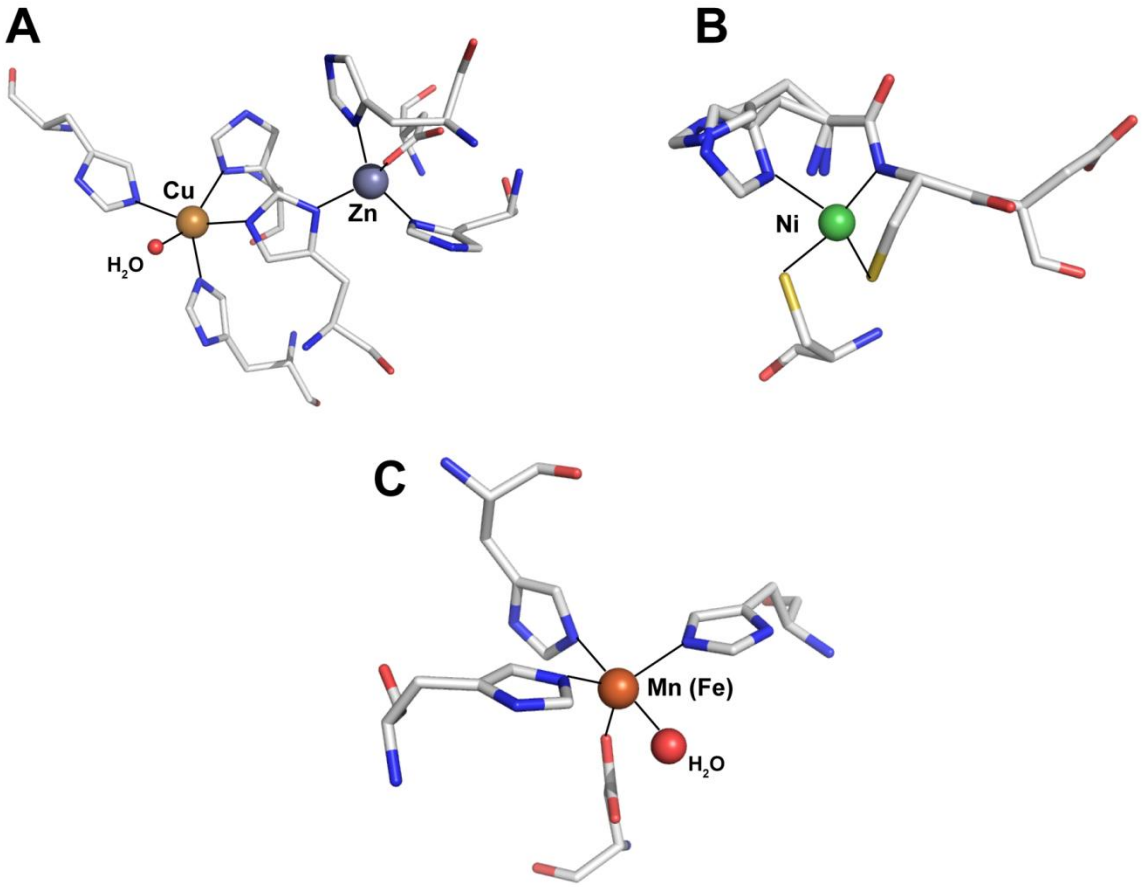

Figure 1.2. The active site structures of four classes of SOD. (A) *Homo sapien* CuZnSOD (pdb code: 1PU0); (B) *Streptomyces coelicolor* NiSOD (pdb code: 1T6U); (C) *Anaplasma phagocytophilum* FeSOD (pdb code: 3JS4).

mitochondria. CuZnSOD, MnSOD, and FeSOD can be found in the cytosol of prokaryotes, and in chloroplasts of plants (4).

Although CuZnSOD, NiSOD, and Mn(Fe)SOD display similar reactivity toward O_2^-, their protein structures and active site structures differ from each other dramatically. CuZnSOD from eukaryotes is a homodimer rich in β-barrel (Figure 1.1-A). Its binuclear active site consists of a copper and a zinc ion in close enough proximity to share an imidazolate ligand (Figure 1.2-A). The copper ion in the 2+ state is coordinated by three other histidines and a water molecule. The zinc ion binds two other histidines and an aspartate in a pseudo tetrahedral geometry. NiSOD is the most recently discovered form in the SOD family. The enzyme is a homohexamer, and each subunit contains a 4-helix bundle (Figure 1.1-B). It has a mononuclear active site with the nickel coordinated by a histidine and two cysteines in an N_2S_2 square planar geometry (Figure 1.2-B). Mn- and FeSOD are structure homologs. FeSOD is always a homodimer, while MnSOD is either a homodimer or a homotetramer (Figure 1.1-C). The Mn or Fe ion is coordinated by three histidines, one aspartate and a water molecule in an approximately trigonal bipyramidal geometry (Figure 1.2-C).

Biological Importance of Manganese-containing SOD (MnSOD)

MnSOD is the major antioxidant in the mitochondria. Numerous studies on animal models with a MnSOD deficiency suggest that MnSOD is critical for life. MnSOD (–/–) homogeneous knockout mice, which exhibit extensive mitochondrial injury that causes severe neurodegeneration and dilated cardiomyopathy, have a greatly shortened survival of 10-20 days after birth (5,6). The activities of succinate dehydrogenase (complex II) and aconitase are

reduced significantly in the heart (7). MnSOD (+/–) heterogeneous knockout mice, with a partial deficiency of MnSOD activity, also show an increase in oxidative damage to mitochondria and altered mitonchondria function (8).

MnSOD is associated with oxidative stress-related apoptosis and aging. Overexpression of MnSOD protects mammalian cells from tumor necrosis factor (TNF)–α–induced apoptosis by increasing the production of H_2O_2 (9). Overexpression of MnSOD also prevents neural apoptosis induced by Fe^{2+}, amyloid β-peptide (Aβ), and nitric oxide–generating agents (10). Mitochondria from MnSOD (+/–) heterogeneous knockout mice show evidence of age-related rapid accumulation of oxidative damage in relatively early life stages (11). MnSOD (+/–) mice show pronounced phenotypes, such as vascular dysfunction and mitochondrial DNA damage (12). Although several early studies suggested that overexpression of MnSOD increases the lifespan of animal models, more recent studies have shown that overexpression of major antioxidant enzymes, including CuZnSOD, MnSOD and catalase, have no effect on the lifespans of transgenic mice (13).

MnSOD is also implicated in several biomedical applications, including treatment of cancer. Although the role of MnSOD in cancer remains controversial, numerous cell line and animal model studies have shown the suppression of tumor formation and growth by increasing the expression or reactivity of MnSOD (14-17). Delivery of the MnSOD gene to the lungs of cancer mice prevents organ and tissue damage caused by ionizing irradiation (18). Increasing the MnSOD level in transgenic mice reduces ischemia/reperfusion injury by suppressing the basal level of oxidative stress in the brains (10,19).

Because MnSOD is such a critical antioxidant enzyme in vivo, it is important to investigate the mechanism and structure-function relationship of this enzyme, which is the main purpose of my project.

MnSOD has a Unique Mechanism

Like other SODs, MnSOD catalyzes the disproportionation of O_2^- via sequential oxidation (Mn^{3+}) and reduction (Mn^{2+}) of the metal. MnSOD is unique in that it is fast when [O_2^-] is low, and becomes slow when [O_2^-] is high.

Scheme 1.2. Catalytic Mechanism of MnSOD

$$Mn^{3+}SOD + O_2^- \xrightarrow{k_1} Mn^{2+}SOD + O_2 \quad (1)$$

$$Mn^{2+}SOD + O_2^- \xrightarrow{k_2, 2H^+} Mn^{3+}SOD + H_2O_2 \quad (2)$$

$$Mn^{2+}SOD + O_2^- \xrightarrow{k_3} Mn^{3+}(OO^{2-})SOD \quad (3)$$

$$Mn^{3+}(OO^{2-})SOD \xrightarrow{k_4, 2H^+} Mn^{3+}SOD + H_2O_2 \quad (4)$$

The mechanism by which MnSOD removes O_2^- involves product inhibition (4). Specifically, reduction of O_2^- by Mn^{2+}SOD (Scheme 1.2) occurs either through a pathway (called “prompt protonation” pathway here) (reaction 2), where protonation and dissociation of the peroxo moiety is instantaneous, or through an “inner-sphere” pathway (reaction 3), where a detectable intermediate is formed, which has been suggested to be a side-on Mn(III)-peroxo species (20). (We here refer to this intermediate as a Mn-peroxo complex instead of as a

"product-inhibited" complex, the latter term having been used frequently in previous reports.) When protonation of the Mn-peroxo complex (reaction 4) is rate limiting, the "inner-sphere" pathway has the effect of slowing down MnSOD catalysis.

The level of product inhibition is described by k_2/k_3, the gating ratio of the two pathways. The phenomenon of product inhibition is the most prominent in the MnSOD from human, while the enzymes from bacteria are relatively less inhibited at high O_2^- levels, as indicated by the k_2/k_3 in human, *E. coli*, *D. radiodurans* MnSOD as 1.6, 5.3, and 16, respectively (21). Although human and bacterial MnSODs display dramatically different catalytic efficiency at high O_2^- levels, their monomer assembly and active site structure are highly conserved. Numerous studies have been focused on exploring the origin of the different extent of product inhibition in MnSODs from different organisms, through investigating the MnSOD mutant proteins with substitutions at the second sphere of the Mn ion.

Tyr34 is highly conserved and structurally similar in all known MnSODs, where it participates in a hydrogen-bonding network at the active site. Computational studies suggest that Tyr34 provides one of the two protons needed to form H_2O_2 in the catalytic cycle (22). Deprotonation of Tyr34 is responsible for the spectroscopic changes, including the blue shift and decrease in intensity of the optical absorption maximum, that occurs for Mn^{3+}SOD with increasing pH (23). Wild-type human MnSOD and its Y34F mutant have similar k_{cat}/K_m, but k_{cat} is decreased by ~10 fold in the mutant (24). SOD activity, measured by the xanthine oxidase/cytochrome c assay, is only slightly reduced in *E. coli* Y34 mutants (25,26). Tyr34 also plays an interesting role in the "prompt protonation" pathway, as elucidated by the changes in the kinetics of human Tyr34 mutants (27).

Conserved in all Mn and FeSODs, Gln154 donates an H-bond to the metal-bound solvent molecule, and is the only contact of the metal-bound solvent molecule to the protein beyond the active site. Gln154 makes three hydrogen bonds to three highly conserved residues, Tyr34, Asn80 and Trp133 (numbering in *Saccharomyces cerevisiae* MnSOD (*Sc*MnSOD)). Its hydrogen bonding potential is fully utilized and Gln154 seems firmly fixed in place. Gln154 together with Asp168 that is an H-bond acceptor from the metal-coordinated H_2O or OH^-, determine the position of the coordinated solvent molecule. Mutagenesis on Gln154 often causes dramatic depression of reactivity (26,28,29), indicating the key role of the NE2(Gln154)···O(solv) bond.

Both Tyr34 and Gln154 are part of the hydrogen-bonding network extending from the active site to the dimer interface. This O(solvent ligand)···NE2(Gln143)···OH(Tyr34) ···OH2(solvent)···ND1(His30)···OH(Tyr175) (numbering in *Sc*MnSOD) hydrogen-bonding chain is conserved in all MnSODs and has been proposed to play an important role in proton transfer (30). Mutation of either His30 or Tyr174 in *Ec*MnSOD reduces the enzymatic activity to 30–40% of that of the wild-type enzyme (31). The H30V variant of human MnSOD exhibits increased product inhibition by 1–2 orders of magnitude (32). Its H30N variant is significantly more efficient than the wild-type enzyme at high levels of O_2^- due to the increased rate of dissociation of the Mn-peroxo complex; this increased enzymatic efficiency causes anti-tumor effects in animal models (15). By constrast, substitution of Tyr166 in human MnSOD prolongs the lifetime of the Mn-peroxo complex (33). Nevertheless, these results have not yet elucidated the reason for MnSOD being so inhibited in the human enzyme but not the others.

The only success in weakening product inhibition in human MnSOD is through the substitutions of Phe66 at the dimer interface of the human enzyme (34). Therefore, the origin of the product inhibition became the major interest of my project. Yeast is an important single-cell

model for studying human and other eukaryotic cells. Like human cells, *S. cerevisiae* expresses a homotetrameric MnSOD in its mitochondria (*Sc*MnSOD), which shares sequence similarity with human MnSOD. I have been trying to elucidate the mystery of the MnSOD mechanism through investigating the biochemical and biophysical properties of yeast MnSOD.

Product Inhibition in MnSOD and H_2O_2 Signaling

Efficient removal of high concentrations of O_2^- will, by necessity, produce high local concentrations of H_2O_2. H_2O_2 is a biologically important class of reactive oxygen species (ROS). It can be reduced to hydroxyl radical ($^{\bullet}OH$) through a Fenton-type reaction with a reduced metal ($M^{(n-1)+} + H_2O_2 \rightarrow M^{n+} + OH^- + {}^{\bullet}OH$), whose reaction with cellular components causes severe damage to lipids, proteins, and nucleotides. The oxidative damage caused both directly and indirectly by H_2O_2 is implicated in cancer and aging (35,36).

Human MnSOD is much less efficient at turning O_2^- into H_2O_2 than MnSOD isolated from bacteria when O_2^- levels are high. Mitochondria are recognized as the main source of O_2^- with the production occurring through respiratory chain. H_2O_2 is generated in mitochondrial matrix via the dismutation reaction of O_2^- catalyzed by MnSOD. The produced H_2O_2 then diffuses into cytosol. The roles of H_2O_2 are complex in higher organisms. In mammalian cells the upregulated expression of antioxidant enzymes is not a universal response to supraphysiologic levels of H_2O_2 (37). Instead, physiologic levels of H_2O_2 stimulate cell division, transformation, migration or apoptosis (37-40). This along with the fact that mammalian cells generate H_2O_2 in response to various stimuli supports that H_2O_2 is utilized as a signaling agent in numerous mammalian signaling pathways (37-43).

A well established H_2O_2-induced signaling is the modulation of the tyrosine phosphorylation of proteins by causing the oxidative inhibition of tyrosine phosphatases (43). Reversible inactivation of tyrosine phosphatases has been demonstrated to play a critical role in protein tyrosine phosphatase (PTP) and insulin signaling (44,45). Several mitochondrial signaling pathways are stimulated by increased H_2O_2, including tumor necrosis factor (TNF)-α-induced apoptosis (9) and c-Jun NH_2-terminal kinase (JNK)-induced apoptosis (41,46). The participation of H_2O_2 in signaling cascades may require tight regulation of its production in mitochondria.

A recent study demonstrates the production of large bursts of O_2^-, termed "superoxide flashes", in human mitochondria (47). The flash events occur randomly in space and time, last for 20–30 seconds and are confined to tiny elliptical areas (47). Under the conditions that were tested human MnSOD in mitochondrial matrix was expected to eliminate superoxide flashes in a shorter time scale, considering that the reactivity of human MnSOD was thought to be diffusion controlled ($k = 2.3 \times 10^9$ M^{-1} s^{-1}) and its intramitochondrial concentration is 10–40 μM (41,48). The observation of superoxide flashes indicates that human MnSOD is unable to maintain a steady-state concentration of O_2^- in tiny elliptical areas in mitochondria. The most likely explanation for this phenomenon is that human MnSOD is significantly inhibited at these high concentrations of O_2^-. Under these conditions, bursts of O_2^- are not translated into bursts of H_2O_2 that could result in aberrant oxidant-driven signaling in mitochondria.

Tetramer and Dimer Interfaces in MnSOD

MnSOD is either a homodimer or a homotetramer with a monomer size of ~23,000 Da. The enzymes located in eukaryote mitochondria (human (49), *S. cerevisiae* (50), *Caenorhabditis*

elegans (51), *Aspergillus fumigates* (52)) were found to be homotetramers, while MnSODs isolated from bacteria (*Thermus thermophilus* (53), *Escherichia coli* (54), *Deinococcus radiodurans* (55)) are homodimers. In all MnSODs, each subunit is composed of two domains, a predominantly α-helical N-terminal domain and a mixed α/β C-terminal domain (Figure 1.3). The Mn ion is coordinated by four strictly conserved residues, two from the N-terminal domain and two from the C-terminal domain, and one solvent molecule.

The difference in the quaternary structure between human and bacterial MnSOD lies in the N-terminus of the subunit. In human MnSOD the N-terminus of each subunit folds into a hairpin structure holding two long α-helixes, while in bacterial MnSODs these α-helixes are much shorter. In human MnSOD, the two N-terminal regions form one of the two 4-helix bundles at the tetramer interface, and this configuration has been proposed to be critical for tetramer formation (49,53).

Scheme 1.3. Alignment of MnSOD C-terminal Sequence. Conserved residues and unconserved residues at the dimer interface are highlighted in bold and shadowed in gray, respectively.

*Ca*MnSODc	AI**DAWEH**AY**YL**QY**N**VKLDYFKAIWN**V**INWAEAESRYSA------	206
*Sc*MnSOD2	AI**DAWEH**AY**YL**QY**N**KKADYFKAIWN**V**VNWKEASRRFDAGKI---	207
E. coli	GL**DVWEH**AY**YL**KF**N**RRPDYIKEFWN**V**VNWDEAAARFAAKK----	206
D. radiodurans	GV**DVWEH**AY**YL**NY**N**RRPDYLAAFWN**V**VNWDEVSKRYAAAK----	211
D. melanogaster	GI**DVWEH**AY**YL**QY**N**VRPSYVEAIWD**I**ANWDDISCRFQEAKKLGC	206
C. elegans	GI**DVWEH**AY**YL**QY**N**VRPDYVHAIWK**I**ANWKNISERFANARQ---	200
mouse	GI**DVWEH**AY**YL**QY**N**VRPDYLKAIWN**V**INWENVTERYTACKK---	205
human	GI**DVWEH**AY**YL**QY**N**VRPDYLKAIWN**V**INWENVTERYMACKK---	205

The MnSOD dimer is the basic unit for both dimeric and tetrameric MnSOD enzymes. A

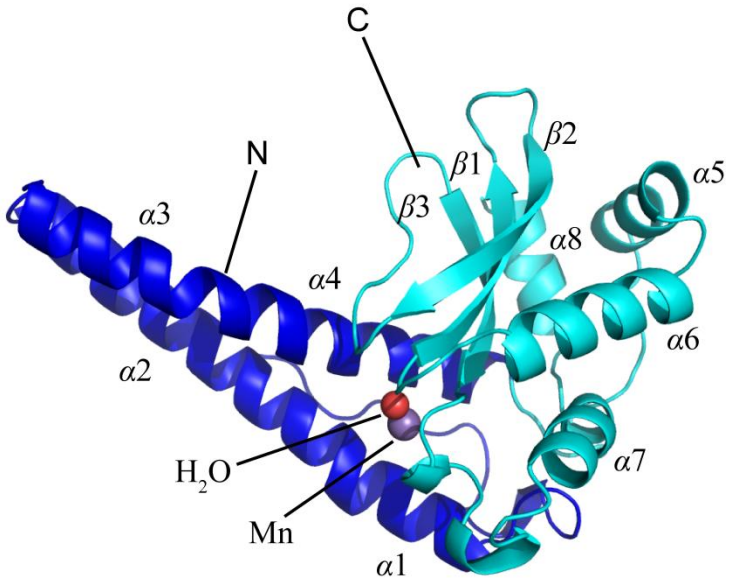

Figure 1.3. The monomer structure of MnSOD (from *S. cerevisiae*, pdb code: 3LSU). The N- and C-terminal are colored in dark and light blue, respectively.

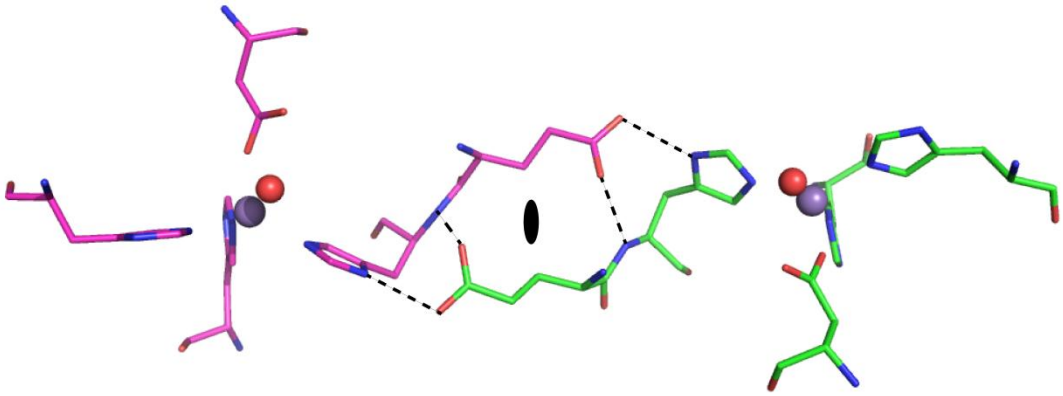

Figure 1.4. The structure of the double glutamate bridge at MnSOD dimer interface. The structure of *E. coli* MnSOD is shown (pdb code: 1VEW). The two subunit in the dimer are colored in red and green.

DXWEHXXYL motif is strictly conserved at the dimer interface of MnSOD (Scheme 1.3); it includes includes two metal-binding residues (Asp168 and His172, numbering in *Sc*MnSOD) and a glutamate (Glu173, numbering in *Sc*MnSOD) that forms hydrogen bond to His from the other subunit across the dimer interface (Figure 1.4).

Several studies suggest a significant role for the dimer interface in both catalysis and stability of MnSOD. Replacement of Glu170 in *Ec*MnSOD, which spans the dimer interface and forms the double glutamate bridge results in dissociation of the dimer, complete loss of catalytic activity, and a change in metal specificity (25). Substitutions of its counterpart in human MnSOD, Glu162, reduce the catalytic activity to 5–25% of that of the wild-type enzyme (56). The Y166F mutant human MnSOD shows a significant decrease in catalytic activity and a major unfolding transition at a lower T_m (33). Replacements of Phe66 at the dimer interface of human MnSOD reduced the extent of product inhibition in human MnSOD, and made it resemble *Ec*MnSOD (34).

Yeast MnSOD and Its Maturation

Baker's yeast, *S. cerevisiae*, expresses a CuZnSOD in the cytosol, and a MnSOD in the mitochondria (*Sc*MnSOD). Yeast cells lacking CuZnSOD (*sod1Δ*) exhibit a broad range of phenotypes, including impaired growth in air, no growth in oxygen, sensitivity to temperature, specific amino acid auxotrophies, etc (57). In contrast, deletion of the MnSOD gene (*sod2Δ*) is relatively benign to *S. cerevisiae*. The only known phenotype for *sod2Δ* strain is low growth on non-fermentable carbon sources or in the presence of superoxide-producing paraquat.

Much is known about the pathway that leads to mature CuZnSOD in vivo. Copper is inserted to the active site of CuZnSOD by CCS (copper chaperone for superoxide dismutase) (58). CCS delivers a copper to a SOD1 monomer through formation of a SOD1-CCS heterodimeric complex (59). In contrast, the mechanism by which the activation of MnSOD occurs in vivo remains unclear. Two metal transporters are known to participate in the post-translational modification of *Sc*MnSOD. The manganese trafficking to mitochondria requires the Nramp metal transporter, Smf2p, which is located in intracellular vesicles (60). The second transporter, MTM1, is located in the mitochondrial matrix. Although MTM1 has no effects on manganese levels in mitochondria, it is nevertheless required for proper insertion of manganese into mitochondrial *Sc*MnSOD (61). A more recent study showed that *Sc*MnSOD, if not imported into mitochondria, is largely apo and inactive in the cytosol, suggesting that a mitochondrial location is essential for manganese activation of *Sc*MnSOD (62). Manganese can only be inserted into a newly synthesized but not prefolded polypeptide of *Sc*MnSOD (62).

Reference

1. Raha, S., and Robinson, B. H. (2001) Mitochondria, oxygen free radicals, and apoptosis. *Am J Med Genet* **106**, 62-70

2. Wood, P. M. (1987) The 2 Redox Potentials for Oxygen Reduction to Superoxide. *Trends in Biochemical Sciences* **12**, 250-251

3. Valentine, J. S., Doucette, P. A., and Potter, S. Z. (2005) Copper-zinc superoxide dismutase and amyotrophic lateral sclerosis. *Annu Rev Biochem* **74**, 563-593

4. Abreu, I. A., and Cabelli, D. E. (2010) Superoxide dismutases-a review of the metal-associated mechanistic variations. *Biochim Biophys Acta* **1804**, 263-274

5. Huang, T. T., Carlson, E. J., Kozy, H. M., Mantha, S., Goodman, S. I., Ursell, P. C., and Epstein, C. J. (2001) Genetic modification of prenatal lethality and dilated cardiomyopathy in Mn superoxide dismutase mutant mice. *Free Radic Biol Med* **31**, 1101-1110

6. Lebovitz, R. M., Zhang, H., Vogel, H., Cartwright, J., Jr., Dionne, L., Lu, N., Huang, S., and Matzuk, M. M. (1996) Neurodegeneration, myocardial injury, and perinatal death in mitochondrial superoxide dismutase-deficient mice. *Proc Natl Acad Sci U S A* **93**, 9782-9787

7. Li, Y., Huang, T. T., Carlson, E. J., Melov, S., Ursell, P. C., Olson, J. L., Noble, L. J., Yoshimura, M. P., Berger, C., Chan, P. H., Wallace, D. C., and Epstein, C. J. (1995) Dilated cardiomyopathy and neonatal lethality in mutant mice lacking manganese superoxide dismutase. *Nat Genet* **11**, 376-381

8. Williams, M. D., Van Remmen, H., Conrad, C. C., Huang, T. T., Epstein, C. J., and Richardson, A. (1998) Increased oxidative damage is correlated to altered mitochondrial function in heterozygous manganese superoxide dismutase knockout mice. *Journal of Biological Chemistry* **273**, 28510-28515

9. Melendez, J. A., Dasgupta, J., Subbaram, S., Connor, K. M., Rodriguez, A. M., Tirosh, O., Beckman, J. S., and JourD'Heuil, D. (2006) Manganese superoxide dismutase protects from TNF-alpha-induced apoptosis by increasing the steady-state production of H2O2. *Antioxid Redox Sign* **8**, 1295-1305

10. Keller, J. N., Kindy, M. S., Holtsberg, F. W., St Clair, D. K., Yen, H. C., Germeyer, A., Steiner, S. M., Bruce-Keller, A. J., Hutchins, J. B., and Mattson, M. P. (1998) Mitochondrial manganese superoxide dismutase prevents neural apoptosis and reduces ischemic brain injury: suppression of peroxynitrite production, lipid peroxidation, and mitochondrial dysfunction. *J Neurosci* **18**, 687-697

11. Kokoszka, J. E., Coskun, P., Esposito, L. A., and Wallace, D. C. (2001) Increased mitochondrial oxidative stress in the Sod2 (+/-) mouse results in the age-related decline of mitochondrial function culminating in increased apoptosis. *P Natl Acad Sci USA* **98**, 2278-2283

12. Wenzel, P., Schuhmacher, S., Kienhofer, J., Muller, J., Hortmann, M., Oelze, M., Schulz, E., Treiber, N., Kawamoto, T., Scharffetter-Kochanek, K., Munzel, T., Burkle, A., Bachschmid, M. M., and Daiber, A. (2008) Manganese superoxide dismutase and aldehyde dehydrogenase

deficiency increase mitochondrial oxidative stress and aggravate age-dependent vascular dysfunction. *Cardiovasc Res* **80**, 280-289

13. Perez, V. I., Van Remmen, H., Bokov, A., Epstein, C. J., Vijg, J., and Richardson, A. (2009) The overexpression of major antioxidant enzymes does not extend the lifespan of mice. *Aging Cell* **8**, 73-75

14. Li, S., Yan, T., Yang, J. Q., Oberley, T. D., and Oberley, L. W. (2000) The role of cellular glutathione peroxidase redox regulation in the suppression of tumor cell growth by manganese superoxide dismutase. *Cancer Res* **60**, 3927-3939

15. Davis, C. A., Hearn, A. S., Fletcher, B., Bickford, J., Garcia, J. E., Leveque, V., Melendez, J. A., Silverman, D. N., Zucali, J., Agarwal, A., and Nick, H. S. (2004) Potent anti-tumor effects of an active site mutant of human manganese-superoxide dismutase. Evolutionary conservation of product inhibition. *J Biol Chem* **279**, 12769-12776

16. Zhao, Y., Xue, Y., Oberley, T. D., Kiningham, K. K., Lin, S. M., Yen, H. C., Majima, H., Hines, J., and St Clair, D. (2001) Overexpression of manganese superoxide dismutase suppresses tumor formation by modulation of activator protein-1 signaling in a multistage skin carcinogenesis model. *Cancer Res* **61**, 6082-6088

17. Church, S. L., Grant, J. W., Ridnour, L. A., Oberley, L. W., Swanson, P. E., Meltzer, P. S., and Trent, J. M. (1993) Increased manganese superoxide dismutase expression suppresses the malignant phenotype of human melanoma cells. *Proc Natl Acad Sci U S A* **90**, 3113-3117

18. Epperly, M., Bray, J., Kraeger, S., Zwacka, R., Engelhardt, J., Travis, E., and Greenberger, J. (1998) Prevention of late effects of irradiation lung damage by manganese superoxide dismutase gene therapy. *Gene Ther* **5**, 196-208

19. Macmillan-Crow, L. A., and Cruthirds, D. L. (2001) Invited review: manganese superoxide dismutase in disease. *Free Radic Res* **34**, 325-336

20. Jackson, T. A., and Brunold, T. C. (2004) Combined spectroscopic/computational studies on Fe- and Mn-dependent superoxide dismutases: insights into second-sphere tuning of active site properties. *Acc Chem Res* **37**, 461-470

21. Sheng, Y., Stich, T. A., Barnese, K., Gralla, E. B., Cascio, D., Britt, R. D., Cabelli, D. E., and Valentine, J. S. (2011) Comparison of two yeast MnSODs: mitochondrial Saccharomyces cerevisiae versus cytosolic Candida albicans. *J Am Chem Soc* **133**, 20878-20889

22. Jackson, T. A., Karapetian, A., Miller, A. F., and Brunold, T. C. (2005) Probing the geometric and electronic structures of the low-temperature azide adduct and the product-inhibited form of oxidized manganese superoxide dismutase. *Biochemistry* **44**, 1504-1520

23. Maliekal, J., Karapetian, A., Vance, C., Yikilmaz, E., Wu, Q., Jackson, T., Brunold, T. C., Spiro, T. G., and Miller, A. F. (2002) Comparison and contrasts between the active site PKs of Mn-superoxide dismutase and those of Fe-superoxide dismutase. *J Am Chem Soc* **124**, 15064-15075

24. Guan, Y., Hickey, M. J., Borgstahl, G. E., Hallewell, R. A., Lepock, J. R., O'Connor, D., Hsieh, Y., Nick, H. S., Silverman, D. N., and Tainer, J. A. (1998) Crystal structure of Y34F mutant

human mitochondrial manganese superoxide dismutase and the functional role of tyrosine 34. *Biochemistry* **37**, 4722-4730

25. Whittaker, M. M., and Whittaker, J. W. (1997) Mutagenesis of a proton linkage pathway in Escherichia coli manganese superoxide dismutase. *Biochemistry* **36**, 8923-8931

26. Edwards, R. A., Whittaker, M. M., Whittaker, J. W., Baker, E. N., and Jameson, G. B. (2001) Outer sphere mutations perturb metal reactivity in manganese superoxide dismutase. *Biochemistry* **40**, 15-27

27. Perry, J. J., Hearn, A. S., Cabelli, D. E., Nick, H. S., Tainer, J. A., and Silverman, D. N. (2009) Contribution of human manganese superoxide dismutase tyrosine 34 to structure and catalysis. *Biochemistry* **48**, 3417-3424

28. Hsieh, Y. S., Guan, Y., Tu, C. K., Bratt, P. J., Angerhofer, A., Lepock, J. R., Hickey, M. J., Tainer, J. A., Nick, H. S., and Silverman, D. N. (1998) Probing the active site of human manganese superoxide dismutase: The role of glutamine 143. *Biochemistry* **37**, 4731-4739

29. Leveque, V. J., Stroupe, M. E., Lepock, J. R., Cabelli, D. E., Tainer, J. A., Nick, H. S., and Silverman, D. N. (2000) Multiple replacements of glutamine 143 in human manganese superoxide dismutase: effects on structure, stability, and catalysis. *Biochemistry* **39**, 7131-7137

30. Perry, J. J., Shin, D. S., Getzoff, E. D., and Tainer, J. A. (2010) The structural biochemistry of the superoxide dismutases. *Biochim Biophys Acta* **1804**, 245-262

31. Edwards, R. A., Whittaker, M. M., Whittaker, J. W., Baker, E. N., and Jameson, G. B. (2001) Removing a hydrogen bond in the dimer interface of Escherichia coli manganese superoxide dismutase alters structure and reactivity. *Biochemistry* **40**, 4622-4632

32. Hearn, A. S., Stroupe, M. E., Cabelli, D. E., Ramilo, C. A., Luba, J. P., Tainer, J. A., Nick, H. S., and Silverman, D. N. (2003) Catalytic and structural effects of amino acid substitution at histidine 30 in human manganese superoxide dismutase: Insertion of valine C gamma into the substrate access channel. *Biochemistry* **42**, 2781-2789

33. Hearn, A. S., Fan, L., Lepock, J. R., Luba, J. P., Greenleaf, W. B., Cabelli, D. E., Tainer, J. A., Nick, H. S., and Silverman, D. N. (2004) Amino acid substitution at the dimeric interface of human manganese superoxide dismutase. *Journal of Biological Chemistry* **279**, 5861-5866

34. Zheng, J., Domsic, J. F., Cabelli, D., McKenna, R., and Silverman, D. N. (2007) Structural and kinetic study of differences between human and Escherichia coli manganese superoxide dismutases. *Biochemistry* **46**, 14830-14837

35. Valko, M., Rhodes, C. J., Moncol, J., Izakovic, M., and Mazur, M. (2006) Free radicals, metals and antioxidants in oxidative stress-induced cancer. *Chem Biol Interact* **160**, 1-40

36. Giorgio, M., Trinei, M., Migliaccio, E., and Pelicci, P. G. (2007) Hydrogen peroxide: a metabolic by-product or a common mediator of ageing signals? *Nat Rev Mol Cell Biol* **8**, 722-728

37. Veal, E. A., Day, A. M., and Morgan, B. A. (2007) Hydrogen peroxide sensing and signaling. *Mol Cell* **26**, 1-14

38. Stone, J. R., and Yang, S. (2006) Hydrogen peroxide: a signaling messenger. *Antioxid Redox Signal* **8**, 243-270

39. Finkel, T., and Holbrook, N. J. (2000) Oxidants, oxidative stress and the biology of ageing. *Nature* **408**, 239-247

40. Finkel, T. (2003) Oxidant signals and oxidative stress. *Curr Opin Cell Biol* **15**, 247-254

41. Cadenas, E. (2004) Mitochondrial free radical production and cell signaling. *Mol Aspects Med* **25**, 17-26

42. Droge, W. (2002) Free radicals in the physiological control of cell function. *Physiol Rev* **82**, 47-95

43. Rhee, S. G. (2006) Cell signaling. H2O2, a necessary evil for cell signaling. *Science* **312**, 1882-1883

44. Mahadev, K., Wu, X., Zilbering, A., Zhu, L., Lawrence, J. T., and Goldstein, B. J. (2001) Hydrogen peroxide generated during cellular insulin stimulation is integral to activation of the distal insulin signaling cascade in 3T3-L1 adipocytes. *J Biol Chem* **276**, 48662-48669

45. Tonks, N. K. (2005) Redox redux: revisiting PTPs and the control of cell signaling. *Cell* **121**, 667-670

46. Chen, K., Thomas, S. R., Albano, A., Murphy, M. P., and Keaney, J. F., Jr. (2004) Mitochondrial function is required for hydrogen peroxide-induced growth factor receptor transactivation and downstream signaling. *J Biol Chem* **279**, 35079-35086

47. Wang, W., Fang, H., Groom, L., Cheng, A., Zhang, W., Liu, J., Wang, X., Li, K., Han, P., Zheng, M., Yin, J., Mattson, M. P., Kao, J. P., Lakatta, E. G., Sheu, S. S., Ouyang, K., Chen, J., Dirksen, R. T., and Cheng, H. (2008) Superoxide flashes in single mitochondria. *Cell* **134**, 279-290

48. Cadenas, E., and Davies, K. J. (2000) Mitochondrial free radical generation, oxidative stress, and aging. *Free Radic Biol Med* **29**, 222-230

49. Borgstahl, G. E., Parge, H. E., Hickey, M. J., Beyer, W. F., Jr., Hallewell, R. A., and Tainer, J. A. (1992) The structure of human mitochondrial manganese superoxide dismutase reveals a novel tetrameric interface of two 4-helix bundles. *Cell* **71**, 107-118

50. Ravindranath, S. D., and Fridovich, I. (1975) Isolation and characterization of a manganese-containing superoxide dismutase from yeast. *J Biol Chem* **250**, 6107-6112

51. Trinh, C. H., Hunter, T., Stewart, E. E., Phillips, S. E., and Hunter, G. J. (2008) Purification, crystallization and X-ray structures of the two manganese superoxide dismutases from Caenorhabditis elegans. *Acta Crystallogr Sect F Struct Biol Cryst Commun* **64**, 1110-1114

52. Fluckiger, S., Mittl, P. R., Scapozza, L., Fijten, H., Folkers, G., Grutter, M. G., Blaser, K., and Crameri, R. (2002) Comparison of the crystal structures of the human manganese superoxide dismutase and the homologous Aspergillus fumigatus allergen at 2-A resolution. *J Immunol* **168**, 1267-1272

53. Wagner, U. G., Pattridge, K. A., Ludwig, M. L., Stallings, W. C., Werber, M. M., Oefner, C., Frolow, F., and Sussman, J. L. (1993) Comparison of the crystal structures of genetically engineered human manganese superoxide dismutase and manganese superoxide dismutase from Thermus thermophilus: differences in dimer-dimer interaction. *Protein Sci* **2**, 814-825

54. Edwards, R. A., Baker, H. M., Whittaker, M. M., Whittaker, J. W., Jameson, G. B., and Baker, E. N. (1998) Crystal structure of Escherichia coli manganese superoxide dismutase at 2.1-angstrom resolution. *J Biol Inorg Chem* **3**, 161-171

55. Abreu, I. A., Hearn, A., An, H., Nick, H. S., Silverman, D. N., and Cabelli, D. E. (2008) The kinetic mechanism of manganese-containing superoxide dismutase from Deinococcus radiodurans: a specialized enzyme for the elimination of high superoxide concentrations. *Biochemistry* **47**, 2350-2356

56. Greenleaf, W. B., Perry, J. J., Hearn, A. S., Cabelli, D. E., Lepock, J. R., Stroupe, M. E., Tainer, J. A., Nick, H. S., and Silverman, D. N. (2004) Role of hydrogen bonding in the active site of human manganese superoxide dismutase. *Biochemistry* **43**, 7038-7045

57. Sanchez, R. J., Srinivasan, C., Munroe, W. H., Wallace, M. A., Martins, J., Kao, T. Y., Le, K., Gralla, E. B., and Valentine, J. S. (2005) Exogenous manganous ion at millimolar levels rescues all known dioxygen-sensitive phenotypes of yeast lacking CuZnSOD. *J Biol Inorg Chem* **10**, 913-923

58. Culotta, V. C., Klomp, L. W., Strain, J., Casareno, R. L., Krems, B., and Gitlin, J. D. (1997) The copper chaperone for superoxide dismutase. *J Biol Chem* **272**, 23469-23472

59. Lamb, A. L., Torres, A. S., O'Halloran, T. V., and Rosenzweig, A. C. (2001) Heterodimeric structure of superoxide dismutase in complex with its metallochaperone. *Nat Struct Biol* **8**, 751-755

60. Luk, E. E. C., and Culotta, V. C. (2001) Manganese superoxide dismutase in Saccharomyces cerevisiae acquires its metal co-factor through a pathway involving the Nramp metal transporter, Smf2p. *Journal of Biological Chemistry* **276**, 47556-47562

61. Luk, E., Carroll, M., Baker, M., and Culotta, V. C. (2003) Manganese activation of superoxide dismutase 2 in Saccharomyces cerevisiae requires MTM1, a member of the mitochondrial carrier family. *Proc Natl Acad Sci U S A* **100**, 10353-10357

62. Luk, E., Yang, M., Jensen, L. T., Bourbonnais, Y., and Culotta, V. C. (2005) Manganese activation of superoxide dismutase 2 in the mitochondria of Saccharomyces cerevisiae. *J Biol Chem* **280**, 22715-22720

Chapter 2

Investigation of the Highly Active Manganese Superoxide Dismutase from *Saccharomyces cerevisiae*

Introduction

Manganese superoxide dismutase (MnSOD) enzymes catalyze superoxide (O_2^-) disproportionation by a mechanism that is more complex than those of the other SODs. In particular the reduction of superoxide can proceed via one of two pathways. One pathway dominates when the O_2^- concentration is low relative to the enzyme concentration (reaction 2), and the other pathway dominates when the ratio $[O_2^-]/[\text{MnSOD}]$ is high (reactions 3 and 4). The paradoxical finding is that MnSOD is a less effective SOD catalyst when O_2^- levels are elevated (1).

$$Mn^{3+}SOD + O_2^- \xrightarrow{k_1} Mn^{2+}SOD + O_2 \qquad (1)$$

$$Mn^{2+}SOD + O_2^- \xrightarrow{k_2, 2H^+} Mn^{3+}SOD + H_2O_2 \qquad (2)$$

$$Mn^{2+}SOD + O_2^- \xrightarrow{k_3} Mn^{3+}(OO^{2-})SOD \qquad (3)$$

$$Mn^{3+}(OO^{2-})SOD \xrightarrow{k_4, 2H^+} Mn^{3+}SOD + H_2O_2 \qquad (4)$$

The depressed catalytic activity at high O_2^- concentrations is known to be due to the formation of a product-inhibited Mn^{3+}-peroxo adduct resulting from the inner sphere oxidation of Mn^{2+}SOD by O_2^- (reaction 3). This pathway is considerably slower than the outer sphere oxidation and protonation pathway described in reaction 2. The relative levels of product inhibition are described kinetically by the value of k_2/k_3 for different MnSODs (Table 2.1). The contribution from this slower pathway is particularly pronounced in human MnSOD (1). Thus the O_2^- removal and H_2O_2 production rates are dependent on the relative levels of MnSOD and O_2^- and the degree of product inhibition of the specific MnSOD present.

Superoxide concentrations are known to be variable in cells; for example, it has recently been shown that transient O_2^- bursts, termed "superoxide flashes", are formed in human mitochondria (2), creating the possibility of even greater variability in H_2O_2 formation rates. However, a slower product-inhibited pathway in human MnSOD would allow for more constant H_2O_2 formation even when O_2^- concentrations vary. Low levels of H_2O_2 play an important role in signaling in mammalian cells, regulating numerous processes including rates of cell growth and division (3). It has been proposed that the slower pathway for human MnSOD appeared in response to an evolutionary pressure to control more tightly intracellular H_2O_2 levels,1 to reduce H_2O_2 mediated oxidative damage, and to optimize its signaling function (4). The k_2/k_3 values determined for human and bacterial MnSODs (Table 2.1) are consistent with this hypothesis. However, structural studies of different MnSODs, both wild type and mutant, have yet to reveal why k_2/k_3 differs so dramatically for this enzyme (1).

The budding yeast *Saccharomyces cerevisiae* is widely used as a single-cell model for higher eukaryotic organisms because it is remarkably similar to mammalian cells. *S. cerevisiae* also appears to be less sensitive to H_2O_2 than human cells, and the only currently known H_2O_2 sensing proteins in *S. cerevisiae* (YAP1p and Skn7p) are involved in regulating oxidative stress protection; a more general signaling role has yet to be found (3,5). Both human MnSOD and *S. cerevisiae* MnSOD (*Sc*MnSOD) are tetramers (6) and localized to the mitochondrial matrix (7), while most bacterial MnSODs are dimers. Moreover, human MnSOD shares greater sequence similarity with *Sc*MnSOD than with *Escherichia coli* or *Deinococcus radiodurans* MnSODs (62.2%, 52.9%, and 54.5% respectively) (8-10). Published reports of the activity of *Sc*MnSOD do not include a determination of the degree of product inhibition (6,11). We therefore turned

Table 2.1. Rate constants for the different MnSODs

Organism	k_1 (nMs^{-1})	k_2 (nMs^{-1})	k_3 (nMs^{-1})	k_4 (s^{-1})	k_2/k_3
Human (9)	1.4	0.6	0.5	130	1.6
E. coli (12)	1.1	0.9	0.17	60	5.3
D. radiodurans (8)	1.2	1.1	0.07	30	16
S. cerevisiae (this work)	1.1 - 1.5	0.8	0.04 -0.05	90 -140	16 - 20

our attention to characterizing the catalytic mechanism of *Sc*MnSOD with the expectation that the high contribution from the product-inhibited pathway would prove to be a property common to eukaryotic MnSODs. Surprisingly, we found instead that *Sc*MnSOD is even less product-inhibited than the bacterial MnSODs characterized to date, surpassing even the high activity of MnSOD from the radiation resistant bacterium *D. radiodurans* (8).

Materials and Methods

Isolation and Characterization of ScMnSOD. The MnSOD protein was grown in the native *S. cerevisiae* host. An over expression vector for the *Sc*MnSOD including the native mitochondrial matrix leader sequence (YEp352-SOD2, a yeast/*E. coli* shuttle vector containing the URA3 selectable marker and a 2-kb genomic *Bam*HI fragment containing the gene for *Sc*MnSOD) (13) was transformed in to wild type *S. cerevisiae* (EG103).

The strain was kept in frozen stocks at -80˚C. The yeast cells were streaked out on to SD-URA plates, which were then incubated at 30˚C for 3 days. A single colony was selected and used to inoculate a sterile test tube containing 4-mL SD-URA medium; the flask was then grown overnight. The first overnight was used to inoculate a second overnight (100 mL in 4- 125 mL flasks) to 0.05 OD_{600}. The second overnight was used to inoculate 1 L cultures to 0.05 OD_{600} in pH 4 YPEG medium (1% yeast extract, 2% peptone, 2% ethanol, 2% glycerol) supplemented with 500 µM Mn(II) acetate. Cells were grown for 3 days or until they reached an $OD_{600} \geq 25$.

We modified the purification from Ravindranath *et. al.* (6); most notably we omitted the heat treatment, and we used a gentler ammonium sulfate cut.

After growth, the cells were spun down (3500 RPM for 10 minutes at 4 ^{o}C, Sorvall H6000A rotor), re-suspended in 250 mL of lysis buffer (50 mM pH 7.4 tris-HCl, 5 mM EDTA, 200 µM PMSF, and 1 µg/mL of leupeptin and pepstatin) and lysed by bead (.5 mm glass beads) beating (10 cycles at 2 minutes of beating and 2 minutes of chilling on ice). The resulting lysate was clarified by centrifugation (30 minutes at 11000 RPM, Beckman JA-14 rotor). The supernatant was adjusted to 50% ammonium sulfate by slowly adding ammonium sulfate (29.5 g of ammonium sulfate per 100 mL of supernatant) to the lysate. The solution was then stirred on ice for 30 minutes and clarified by centrifugation (45 minutes at 8000 RPM, Beckman JA-14 rotor).

The lysate was loaded on to a Hydrophobic Interaction column (Phenyl Sepharose 6 Fast Flow, high sub) with 230-250 mL of column media, washed with 2 column volumes of wash buffer (50 mM pH 7 sodium phosphate, 150 mM NaCl, 100 µM EDTA, and 2 M $(NH4)_2SO4$), and then eluted with a gradient of elution buffer (50 mM pH 7 sodium phosphate, 150 mM NaCl, and 100 µM EDTA). The fractions with the highest SOD activities were pooled.

SOD activity was measured by a modification of the method of Quick and Dugan (14). 20 µL of each of the fractions were aliquoted into a 96-well microtiter plate. Each well contained 162.5 µL of a PBS solution containing 200 µM hypoxanthine, 100 µM XTT (2,3-Bis(2-methoxy-4-nitro-5-sulfophenyl)-2H-tetrazolium-5-carboxanilide inner salt), and 120 U/mL of bovine catalase. Then, 162.5 µL of a 6 x 10^{-3} U/mL solution of xanthine oxidase was added to each well. The plate was then monitored on a plate reader at 490 nm (orange color) for 30 minutes. The absence of color change indicates the inhibition of the reduction of XTT by O_2^-. Thus SOD activity inhibits the formation of the orange color.

The SOD active fractions were pooled and dialyzed twice against 4 L of water and then once again against 4 L of column buffer (25 mM potassium phosphate, pH 7.4). The dialyzed protein sample was then loaded on to an anion exchange DEAE column (150 mL of Whatman DEAE-52), washed with two column volumes of column buffer, and eluted with 4X column buffer (no gradient). Again the SOD activity of the fractions was measured, and the most active fractions were pooled.

For further purification the protein sample was concentrated to < 8 mL using a 10,000 Da MWCO Amicon filter, loaded on to a G300 (Sepharose HR300) gel filtration column, and eluted with column buffer. The SOD activity and protein purity (below) was measured, and the most pure fractions with the highest SOD activity were pooled.

The purity was analyzed by SDS poly acrylamide gel electrophoresis (PAGE) and HPLC (Agilent 1200 series) fitted with a size exclusion column (Tosoh Bioscience, TSK gel G2000SW 7.5 mm ID x 30 cm) with diode array spectrophotometer monitoring at 280 nm for detection of protein. The column was calibrated using five standard proteins: thyroglobulin (670 kDa), bovine g-globulin (158 kDa), ovalbumin (44 kDa), equine myoglobulin (17 kDa), and vitamin K (1.35 kDa). The running buffer was 25 mM sodium phosphate (pH 6.7) and 25 mM sodium chloride.

Pulse Radiolysis. The pulse radiolysis experiments were carried out using the 2 MeV Van de Graaf accelerator at Brookhaven National Laboratory. Superoxide (O_2^-) was generated in air-saturated aqueous solution containing sodium formate (15). The experiments to measure catalytic rates were carried out in two methods: (a) oxidizing the resting enzyme with substoichiometric concentration of O_2^- and following the appearance of Mn(III)SOD which has an absorbance band around 480 nm; (b) following the decay of various concentrations of O_2^- at 260 nm. k_2 was

determined by fitting the time trace of the generating Mn(III) to a first-order reaction. The other catalytic rates were determined by fitting the data obtained by using the Chemical Kinetics program in PRWIN (16). All samples were analyzed in 10 mM potassium phosphate, 10 mM sodium formate, and 10 μM EDTA at 25 ℃. Enzyme concentrations vary from 1 to 60 μM. In method a, hydrogen peroxide (2:1 ratio to enzyme) was added to sample buffer to ensure that the enzyme was fully reduced before each O_2^- flux. The pH of the buffer was adjusted using sodium hydroxide and sulfuric acid.

EPR Spectroscopy. X-band perpendicular-polarization ($B_0 \perp B_1$) and parallel-polarization ($B_0 \parallel B_1$) continuous-wave electron paramagnetic resonance (CW EPR) spectra were recorded using a Bruker ECS106 spectrometer equipped with a dual-mode cavity (ER 4116DM) operating at 9.69 and 9.39 GHz, respectively. Cryogenic temperatures were achieved and controlled using an Oxford Instruments ESR900 liquid helium cryostat in conjunction with an Oxford Instruments ITC503 temperature and gas flow controller. Spectra were acquired under slow-passage, non-saturating conditions. Additional spectrometer settings were: modulation frequency = 100 kHz; modulation amplitude = 0.5 mT.

Results and Discussion

The gene of *Sc*MnSOD (11), which includes the mitochondrial targeting sequence, was inserted into the plasmid YEp352. The enzyme was overexpressed in *S. cere*V*isiae* and purified using a protocol modified from that of Fridovich *et. al*. (6). The protein was isolated as a tetramer with the leader sequence removed and contained 0.6 equiv of Mn per monomer, as per size exclusion chromatography, mass spectrometry, and ICP-MS, respectively.

Although the fitting of the kinetic data reported here matches the experimental decay of pulsed O_2^-, out of the four rate constants, only k_2 has been measured directly by pulse radiolysis. k_2 was measured by oxidizing the resting enzyme with substoichiometric amounts of O_2^- and following the appearance of Mn^{3+}SOD (Figure 2.3), which has a characteristic absorption band near 480 nm. Unlike other MnSODs, *Sc*MnSOD was isolated in the reduced state, precluding direct measurement of k_1. k_1, k_3, and k_4 were determined by fitting the observed rate of O_2^- loss (ε_{260} = 2000 M^{-1} cm^{-1}) at multiple enzyme concentrations (1-10 μM) and initial O_2^- concentrations (2-48 μM) using PRWIN (16), conditions that, while not physiological, are necessary to study kinetics by pulse radiolysis.1,8 The rate constants are compared to those known for other MnSODs in Table 2.1.

The ability of *Sc*MnSOD to catalyze the dismutation of O_2^- was found to exceed that of the other characterized MnSODs. At low concentrations of O_2^- ($[O_2^-] \approx$ [MnSOD]), the observed rates of disappearance are similar for all the four enzymes (Figure 2.1A). However at high concentrations ($[O_2^-] >>$ [MnSOD]), the differences in activities are pronounced (Figure 2.1B). At the highest concentrations of O_2^- employed in pulse radiolysis, the order of the activities of the enzymes is *S. cerevisiae* > *D. radiodurans* > *E. coli* > human, which is identical to the ordering of k_2/k_3, indicating that the deciding factor is the tendency to form the product-inhibited state.

Most known MnSODs rest in the Mn^{3+} oxidation state (17), but our *Sc*MnSOD was consistently isolated as predominantly reduced Mn^{2+}SOD; the electronic absorption spectrum of as-isolated *Sc*MnSOD lacked the visible absorption band with a maximum near 480 nm. It was reported previously that the optical absorption spectrum of *Sc*Mn^{3+}SOD was unusual relative to those of other MnSODs (6), but the spectrum of *Sc*Mn^{3+}SOD that we obtained by reaction of as-

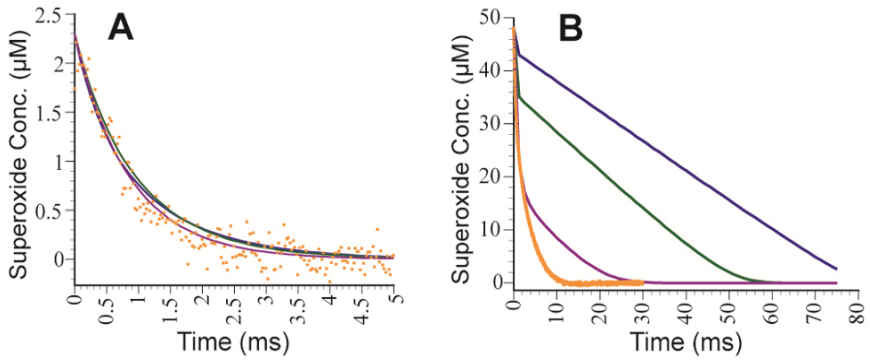

Figure 2.1. *Sc*MnSOD is a more effective catalyst than the other MnSODs studied to date. The first order decay of O_2^- at 2.3 μM (A) and 41 μM (B) O_2^- concentrations. Orange dots are data from pulse radiolysis, while the lines are from modeling using rate constants in Table I and the Kintecus computer-modeling program (18): MnSOD from *S. cerevisiae* (red); *D. radiodurans* (purple); *E. coli* (green); and human (blue); all at 1 μM Mn concentration.

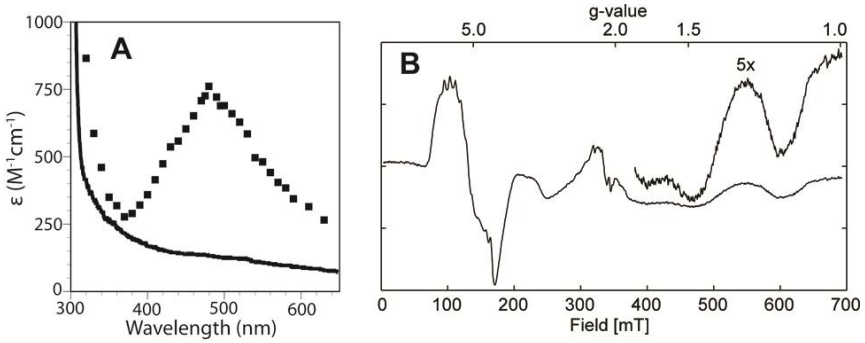

Figure 2.2. *Sc*MnSOD was isolated in the reduced Mn^{2+} oxidation state. A) Electronic absorption spectra of as-isolated *Sc*MnSOD (300 μM MnSOD, line), and that of Mn^{3+}SOD obtained after reaction with O_2^- in pulse radiolysis (dots). B) EPR spectrum of as-isolated *Sc*MnSOD. The instrumental parameters were: temperature, 4.7 K; microwave frequency, 9.685 GHz; microwave power, 1 mW; modulation amplitude, 5.01 G.

isolated *Sc*MnSOD with O_2^- using pulse radiolysis (Figure 2.2A, dots) was very similar to those of other Mn^{3+}SODs, with an extinction coefficient of ~800 M^{-1} cm^{-1}. The small measured absorbance at 480 nm (Figure 2.2A, line) corresponds to greater than 90% of the as-isolated enzyme being in the Mn^{2+} state.

The EPR spectrum of our as-isolated *Sc*MnSOD also indicates that the enzyme is reduced, since the perpendicular-mode EPR spectrum is similar to those of other Mn^{2+}SODs (19,20), with the usual six-line hyperfine splitting from the ^{55}Mn nucleus (I = 5/2) seen at g_{eff} = 6.0 (Figure 2.2B). We looked for evidence of the integer spin Mn^{3+} (S = 2) by parallel-mode EPR, but our spectrum lacked the sextet hyperfine pattern typically displayed by Mn^{3+}SOD (Figure 2.4) (21).

The only other MnSOD enzymes that have been isolated in the Mn^{2+} oxidation state are mutant MnSODs, most notably the Gln143 mutants of the human enzyme (22). However, the factors that determine the resting oxidation state are unknown.

Increased levels of MnSOD activity have been shown to slow tumor growth in cultured human cells and in animal studies (23,24), and it has been proposed that this effect is related to cellular H_2O_2 levels. For that reason and to improve our understanding of the basis of the observed product inhibition, human MnSOD has been repeatedly mutated in attempts to make its activity resemble that of the bacterial proteins, but with limited success (1,10). As described above, human MnSOD already shares greater sequence similarity with *Sc*MnSOD than with the bacterial enzymes, and the two eukaryotic proteins are tetramers while the bacterial ones are dimers. Also, *Sc*MnSOD resembles the bacterial ones in that k_3 is small but is similar to the human enzyme in that k_4 is large. Thus, to improve our understanding of what causes the unusual kinetic properties of human MnSOD, it may be more productive to compare/contrast it with *Sc*MnSOD than with the bacterial MnSODs. Investigation of the slight structural differences

between the enzymes may provide a key to understanding the chemical mechanism of product inhibition. We will also continue to study the evolutionary significance of product inhibition by studying MnSOD from other organisms.

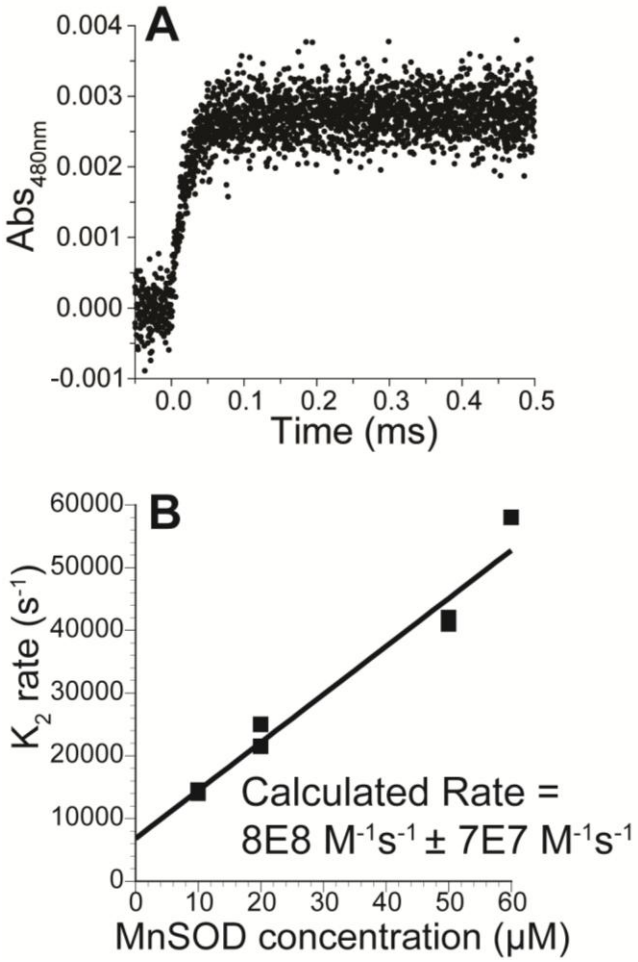

Figure 2.3. Oxidation of *Sc*Mn^{2+}SOD in pulse radiolysis (method a) is shown by the change of absorbance at 480 nm with time after 1.8 μM of O_2^- was generated. Solutions contained 60 μM enzyme (in Mn), 10 mM potassium phosphate (pH 7.5), 10 mM sodium formate, and 10 μM EDTA. The enzyme had been reduced prior to the experiment with 120 μM H_2O_2. **B.** The first order rate of the enzyme was determined at multiple different concentrations of enzyme. The rate was calculated by finding the slope of the least squares liner fitting. In addition to MnSOD the solutions contained 10 mM potassium phosphate (pH 7.5), 10 mM sodium formate, and 10 μM EDTA. The enzyme had been reduced prior to the experiments with at least 200 μM H_2O_2.

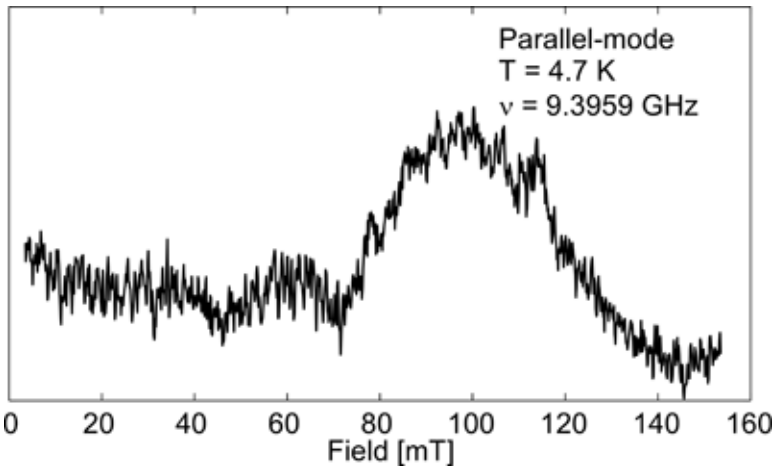

Figure 2.4. Parallel-mode CW-EPR spectrum of as-isolated *Sc*MnSOD. Instrument settings: ν = 9.3959 GHz; microwave power = 32 mW; sweep rate = 1.81 mT/s; temp = 4.7 K.

References

1. Abreu, I. A., and Cabelli, D. E. (2010) Superoxide dismutases-a review of the metal-associated mechanistic variations. *Biochim Biophys Acta* **1804**, 263-274

2. Wang, W., Fang, H., Groom, L., Cheng, A., Zhang, W., Liu, J., Wang, X., Li, K., Han, P., Zheng, M., Yin, J., Mattson, M. P., Kao, J. P., Lakatta, E. G., Sheu, S. S., Ouyang, K., Chen, J., Dirksen, R. T., and Cheng, H. (2008) Superoxide flashes in single mitochondria. *Cell* **134**, 279-290

3. Veal, E. A., Day, A. M., and Morgan, B. A. (2007) Hydrogen peroxide sensing and signaling. *Mol Cell* **26**, 1-14

4. Rhee, S. G. (2006) Cell signaling. H2O2, a necessary evil for cell signaling. *Science* **312**, 1882-1883

5. Stone, J. R., and Yang, S. (2006) Hydrogen peroxide: a signaling messenger. *Antioxid Redox Signal* **8**, 243-270

6. Ravindranath, S. D., and Fridovich, I. (1975) Isolation and characterization of a manganese-containing superoxide dismutase from yeast. *J Biol Chem* **250**, 6107-6112

7. Luk, E., Yang, M., Jensen, L. T., Bourbonnais, Y., and Culotta, V. C. (2005) Manganese activation of superoxide dismutase 2 in the mitochondria of Saccharomyces cerevisiae. *J Biol Chem* **280**, 22715-22720

8. Abreu, I. A., Hearn, A., An, H., Nick, H. S., Silverman, D. N., and Cabelli, D. E. (2008) The kinetic mechanism of manganese-containing superoxide dismutase from Deinococcus radiodurans: a specialized enzyme for the elimination of high superoxide concentrations. *Biochemistry* **47**, 2350-2356

9. Hearn, A. S., Stroupe, M. E., Cabelli, D. E., Lepock, J. R., Tainer, J. A., Nick, H. S., and Silverman, D. N. (2001) Kinetic analysis of product inhibition in human manganese superoxide dismutase. *Biochemistry* **40**, 12051-12058

10. Zheng, J., Domsic, J. F., Cabelli, D., McKenna, R., and Silverman, D. N. (2007) Structural and kinetic study of differences between human and Escherichia coli manganese superoxide dismutases. *Biochemistry* **46**, 14830-14837

11. Schrank, I. S., Sims, P. F., and Oliver, S. G. (1988) Functional expression of the yeast Mn-superoxide dismutase gene in Escherichia coli requires deletion of the signal peptide sequence. *Gene* **73**, 121-130

12. Zheng, J., Domsic, J. F., Cabelli, D., McKenna, R., and Silverman, D. N. (2007) Structural and Kinetic Study of Differences between Human and Escherichia coli Manganese Superoxide Dismutases,Ä†. *Biochemistry* **46**, 14830-14837

13. van Loon, A. P., Pesold-Hurt, B., and Schatz, G. (1986) A yeast mutant lacking mitochondrial manganese-superoxide dismutase is hypersensitive to oxygen. *Proc Natl Acad Sci U S A* **83**, 3820-3824

14. Quick, K. L., Hardt, J. I., and Dugan, L. L. (2000) Rapid microplate assay for superoxide scavenging efficiency. *J Neurosci Methods* **97**, 139-144

15. Fabrizio, P., Liou, L. L., Moy, V. N., Diaspro, A., Valentine, J. S., Gralla, E. B., and Longo, V. D. (2003) SOD2 functions downstream of Sch9 to extend longevity in yeast. *Genetics* **163**, 35-46

16. Schwarz, H., BNL Pulse Radiolysis Program. Brookhaven National Laboratory

17. Messerschmidt, A. (2001) *Handbook of metalloproteins*, Wiley, Chichester ; New York

18. Ianni, J. C. (2008) *Kinetecus, Windows ver. 3.95*, http://www.kintecus.com/

19. Whittaker, J. W., and Whittaker, M. M. (1991) Active-Site Spectral Studies on Manganese Superoxide-Dismutase. *J Am Chem Soc* **113**, 5528-5540

20. Whittaker, M. M., and Whittaker, J. W. (1999) Thermally triggered metal binding by recombinant Thermus thermophilus manganese superoxide dismutase, expressed as the apo-enzyme. *J Biol Chem* **274**, 34751-34757

21. Campbell, K. A., Yikilmaz, E., Grant, C. V., Gregor, W., Miller, A. F., and Britt, R. D. (1999) Parallel polarization EPR characterization of the Mn(III) center of oxidized manganese superoxide dismutase. *J Am Chem Soc* **121**, 4714-4715

22. Leveque, V. J., Stroupe, M. E., Lepock, J. R., Cabelli, D. E., Tainer, J. A., Nick, H. S., and Silverman, D. N. (2000) Multiple replacements of glutamine 143 in human manganese superoxide dismutase: effects on structure, stability, and catalysis. *Biochemistry* **39**, 7131-7137

23. Church, S. L., Grant, J. W., Ridnour, L. A., Oberley, L. W., Swanson, P. E., Meltzer, P. S., and Trent, J. M. (1993) Increased manganese superoxide dismutase expression suppresses the malignant phenotype of human melanoma cells. *Proc Natl Acad Sci U S A* **90**, 3113-3117

24. Davis, C. A., Hearn, A. S., Fletcher, B., Bickford, J., Garcia, J. E., Leveque, V., Melendez, J. A., Silverman, D. N., Zucali, J., Agarwal, A., and Nick, H. S. (2004) Potent anti-tumor effects of an active site mutant of human manganese-superoxide dismutase. Evolutionary conservation of product inhibition. *J Biol Chem* **279**, 12769-12776

Chapter 3

Comparison of Two Yeast MnSODs:

Mitochondrial *Saccharomyces cerevisiae* versus Cytosolic *Candida albicans*

Introduction

Superoxide dismutases (SODs) are enzymes that function to convert the superoxide (O_2^-) anion to dioxygen and hydrogen peroxide (H_2O_2) catalytically via sequential reduction and oxidation of a metal cofactor at virtually diffusion-controlled rate constants (Scheme 3.1).

Scheme 3.1. The Dismutase Mechanism

$$M^{n+} + O_2^- \rightarrow M^{(n-1)+} + O_2$$

$$M^{(n-1)+} + O_2^- + 2H^+ \rightarrow M^{n+} + H_2O_2$$

Manganese-containing superoxide dismutases (MnSODs) are found in a wide variety of species and, in these species, it can be localized either in the cytosol or the mitochondria or both. In bacteria, MnSOD is cytosolic while in yeast both mitochondrial and cytosolic forms exist. In mammalian cells it is mitochondrial. MnSOD catalyzes the disproportionation of O_2^- by a mechanism that distinguishes it from the other SODs in that it becomes a less effective antioxidant when O_2^- levels are high relative to enzyme concentration (1). Specifically, human MnSOD (2) has been shown to be very inefficient at removal of high concentrations of O_2^- whereas the MnSOD from bacteria (*Escherichia coli* (2) and *Deinococcus radiodurans* (3)) and yeast (*Saccharomyces cerevisiae*) (4) are more efficient under the same conditions. It is this feature of differential efficiency at O_2^- removal that led to our interest in exploring the activity of MnSODs from different cellular sources and locations.

Efficient removal of high concentrations of O_2^- will, by necessity, produce high local concentrations of H_2O_2. H_2O_2 is a biologically important class of reactive oxygen species (ROS). It can be reduced to hydroxyl radical ($^{\bullet}OH$) through a Fenton-type reaction with a reduced metal

($M^{(n-1)+} + H_2O_2 \rightarrow M^{n+} + OH^- + {}^{\bullet}OH$), whose reaction with cellular components causes severe damage to lipids, proteins, and nucleotides. The oxidative damage caused both directly and indirectly by H_2O_2 is implicated in cancer and aging (5,6). Besides its toxic effects, the roles of H_2O_2 in aiding phagocytes in the killing of ingested microorganisms as well as in some oxidative biosynthesis are well known (7). In addition in recent years there is rising evidence of H_2O_2 functioning as a signaling agent in higher organisms (7-11).

Scheme 3.2. Catalytic Mechanism of MnSOD

$$Mn^{3+}SOD + O_2^- \xrightarrow{k_1} Mn^{2+}SOD + O_2 \qquad (1)$$

$$Mn^{2+}SOD + O_2^- \xrightarrow{k_2, 2H^+} Mn^{3+}SOD + H_2O_2 \qquad (2)$$

$$Mn^{2+}SOD + O_2^- \xrightarrow{k_3} Mn^{3+}(OO^{2-})SOD \qquad (3)$$

$$Mn^{3+}(OO^{2-})SOD \xrightarrow{k_4, 2H^+} Mn^{3+}SOD + H_2O_2 \qquad (4)$$

The mechanism by which MnSOD removes high O_2^- concentrations less efficiently than other SODs involves product inhibition. The overall reduction of O_2^- by an oxidized metal (Scheme 3.2), when carried out by Mn^{2+}SOD, occurs either through a pathway (reaction 2) where delivery of protons to the bound peroxo moiety is effectively instantaneous (an "outer-sphere" pathway), or through a pathway (reaction 3) where an identifiable transient is formed (an "inner-sphere" pathway), defined here as a "product-inhibited" complex that has been described as a side-on Mn(III)-peroxo species (12). The inner-sphere pathway can become significant at high O_2^- concentrations and, if the dissociation of peroxide (k_4) is relatively slow, this can lead to reduced catalytic efficiency of MnSOD. The level of product inhibition is described by k_2/k_3, the gating ratio of the two pathways.

S. cerevisiae is an important single-cell model for studying human and other eukaryotic cells. Like human cells, it expresses a homotetrameric MnSOD in its mitochondria (*Sc*MnSOD), which shares sequence similarity with human MnSOD. To our surprise, our previous study showed *Sc*MnSOD to be the most efficient at removing high O_2^- concentrations, among MnSODs that have been characterized to date (4). However, the origins of the low level of product inhibition are unclear.

S. cerevisiae and humans have a common cellular localization of their SODs. They both have MnSODs only in their mitochondrion and copper-zinc SODs (CuZnSOD) in their cytosol. In contrast, a closely related yeast *Candida albicans* expresses a MnSOD that lacks the mitochondrial leader sequence and is active in the cytosol (*Ca*MnSODc)* in addition to its mitochondrial *Ca*MnSOD and cytosolic *Ca*CuZnSOD. *Ca*MnSODc shares 70% sequence similarity with *Sc*MnSOD and has been proposed to be important for survival of *C. albicans* in nutrient-limiting conditions (13). Overexpression of *Ca*MnSODc has been shown to rescue the phenotypes of *S. cerevisiae* strain lacking the cytosolic CuZnSOD (13).

In order to understand further the mechanism of product inhibition in MnSOD and its implication in H_2O_2 signaling in higher organisms, we isolated and characterized *Sc*MnSOD and *Ca*MnSODc. Herein we report the first comparison of the catalytic activity of the two yeast MnSODs, the crystal structures of their metal-binding sites, and their spectroscopic characterization. We discuss how these factors relate to the function of yeast MnSODs; we

*We have chosen for the sake of convenience to distinguish between cytosolic and mitochondrial MnSODs by adding a "c" to the MnSOD to indicate that it is a cytosolic enzyme. This distinction becomes important in those organisms (*C. albicans*) where MnSOD is found in both locations. This distinction is not relevant to human and *S. cerevisiae* as all of the MnSOD is mitochondrial.

further compare human, bacterial, and yeast MnSODs; and we explore the implications with respect to the evolution of H_2O_2 signaling.

Materials and Methods

DNA Manipulation of CaMnSODc and Transformation into S. cerevisiae. The pVT102U-*Ca*MnSODc (with *URA*3 and *AMP* marker) vector containing the complete coding sequence of *Ca*MnSODc was generously provided by Prof. Bourbonnais (13). Sequencing shows that it is an I169V mutant of the wild-type protein accidentally created during cloning. The primers 5'-GTTCCAATTATTGCC**A**TCGATGCTTGG-GAA-C-3' and 5'-GTTCCCAAGCATCGA**T**GGC-AATAA-TTGGA-AC-3' were used to create the wild-type cDNA (mutations are in bold type). The PCR products were transformed into *E. coli* DH5α strain and screened by ampicillin selection. The purified pVT102U-*Ca*MnSODc vector was transformed into *S. cerevisiae sod*2Δ strain (EG110; *Mat-alpha, ura3, leu2, trp1, his3, sod2::TRP1*).

Expression and Purification of ScMnSOD and CaMnSODc. Yeast cells carrying Yep352-*Sc*MnSOD (4) were grown in YPEG media (1% yeast extract, 2% peptone, 3% glycerol, 2% ethanol, pH 4) supplemented with 0.5 mM Mn(II) sulfate at 30 ℃ to O.D. > 20, and then harvested by centrifugation at 12,000 × g for 10 min. *Sc*MnSOD was-isolated as previously described (4).

Yeast cells carrying pVT102U-*Ca*MnSODc were grown in YPD (1% yeast extract, 2% peptone, 2% dextrose, pH 4) media supplemented with 0.5 mM Mn(II) sulfate at 30 ℃ to O.D. > 10, and then harvested by centrifugation at 12,000 × g for 10 min. The procedures for isolation of *Ca*MnSODc and *Sc*MnSOD were the same (4) except that the procedures of the DE52 column were different. *Ca*MnSODc does not bind tightly to the DE52 resin while most other proteins in

the crude extract do. The active fractions from the hydrophobic interaction column were pooled and dialyzed against water and then 5 mM potassium phosphate, pH 8 at 4 ℃. The protein then was loaded on a DE52 column, washed with 2 column volumes of 5 mM potassium phosphate, pH 8. *Ca*MnSODc fell into the load and wash during the chromatography. The load and wash were combined, concentrated, and loaded onto a G300 gel filtration column.

Pulse Radiolysis. The pulse radiolysis experiments were carried out using the 2 MeV Van de Graaff accelerator at Brookhaven National Laboratory. Upon irradiation of water with a pulse of energetic electrons, hydrated electrons (e_{aq}^-), hydroxyl radicals ($^{\bullet}OH$) and, in lesser yield, hydrogen atoms ($H^{\bullet}$) are the primary radicals produced. Superoxide radical is then generated in air-saturated aqueous solution containing sodium formate through the following reactions: $^{\bullet}OH + HCO_2^- \rightarrow H_2O + CO_2^{\bullet-}$, $O_2 + CO_2^{\bullet-} \rightarrow O_2^{\bullet-} + CO_2$, $e_{aq}^- + O_2 \rightarrow O_2^{\bullet-}$, $H^{\bullet} + O_2 \rightarrow HO_2^{\bullet}$.

The experiments to measure catalytic rates were carried out using two methodologies. One set of studies involved oxidizing the resting enzyme with substoichiometric quantities of O_2^- and following the appearance of Mn^{3+}SOD which has an absorbance band at around 480 nm (extinction coefficient ≈ 800 $M^{-1}cm^{-1}$). The rate of reaction 2 (k_2) was determined by fitting the resultant time trace of Mn^{3+} growth to a first-order reaction. In this set of experiments, 2:1 [H_2O_2]:[MnSOD] was added as previous studies had shown that H_2O_2 effectively reduces Mn^{3+}SOD to Mn^{2+}SOD. The other method involved following the decay of various concentrations of O_2^- at 260 nm using a 1:1 to 1:50 ratio of [MnSOD]:[O_2^-]. Here, all the rate constants except k_2 were calculated by fitting the data obtained to a mechanism described in Scheme 3.2 using the Chemical Kinetics program in PRWIN (14).

All pulse radiolysis samples were prepared in 10 mM potassium phosphate, 10 mM sodium formate and 10 or 100 μM EDTA at 25 °C. All MnSOD concentrations were taken as the

ICP-measured concentration of manganese in the sample. As all of the manganese concentrations were less than the corresponding protein concentrations, we assumed that all of the manganese was bound. This had the advantage of allowing direct comparison of activity of a tetrametric and a dimeric enzyme as everything is normalized to a monomeric unit. However, it also assumes no cooperativity between metal sites. The pH of the buffer was adjusted using ultrapure (Baker Ultrex) sodium hydroxide and sulphuric acid as needed.

EPR Spectroscopy. X-band (9.47 GHz) perpendicular-polarization ($B_0 \perp B_1$) continuous-wave electron paramagnetic resonance (CW EPR) spectra were recorded using a Bruker ECS106 spectrometer equipped with a TE102 cavity (ER3902ST). Parallel-polarization ($B_0 \parallel B_1$) data were acquired using a dual-mode cavity (ER 4116DM) operating at 9.39 GHz. Cryogenic temperatures were achieved and controlled using an Oxford Instruments ESR900 liquid helium cryostat in conjunction with an Oxford Instruments ITC503 temperature and gas flow controller. Spectral simulations were performed in MatLab using EasySpin 3.1 (15,16).

Crystallization of ScMnSOD and CaMnSODc. The apoprotein of *Sc*MnSOD aggregates after the native protein is heated at 70 ℃ in MOPS, while the metallated *Sc*MnSOD stays folded in solution. Fully metallated *Sc*MnSOD was obtained by heating as-isolated protein (20 mM MOPS, pH 7) at 70 ℃ for 1 hr and removing aggregated protein by centrifugation. The reductive methylation of lysine residues of *Sc*MnSOD was carried out as described, in order to improve the diffraction of protein crystals (17). The activity of native and methylated *Sc*MnSOD is similar in SOD activity assay (18). All the free amino groups of lysine residues and the N-terminal were methylated as confirmed by mass spectrometry (Figure S3.1).

Methylated *Sc*MnSOD was crystallized by hanging-drop vapor diffusion at 4 ℃ against a well solution of 0.2 M sodium malonate (pH 7) in 20% (w/v) polyethylene glycol 3,350 with a

protein concentration of 7 mg/mL. Native *Ca*MnSODc was crystallized by hanging-drop vapor diffusion at 4 ℃ against a solution of 0.1 M magnesium chloride, 0.1 M sodium chloride and 0.1 M tri-sodium citrate (pH 5.5) in 30% (w/v) polyethylene glycol 400 with a protein concentration of 7 mg/mL. *Sc*MnSOD and *Ca*MnSODc crystals were cryo-protected in mother liquor solution containing 30% glycerol and flash frozen in liquid nitrogen prior to data collection.

Crystallography: Data Collection and Refinement. All data was collected at 100K at the UCLA X-ray diffraction facility, using a Rigaku FRE+ generator and a Rigaku HTC detector. All data was processed using DENZO and SCALEPACK (19). *Sc*MnSOD was phased by molecular replacement using human MnSOD Q143N mutant (1QNM). *Ca*MnSODc was phased by molecular replacement using *Sc*MnSOD (3LSU). All the molecular replacement was done using PHASER (20). The models were built using COOT (21). All model refinement was done using REFMAC (22) and PHENIX (23).

Coordinates and structure factors have been deposited in the PDB with accession numbers 3LSU for the *Sc*MnSOD structure and 3QVN for the *Ca*MnSODc structure.

Miscellaneous Methods. The metal contents of the purified proteins were determined by ICP-MS (Agilent 7500 series). UV-Visible absorption spectra were collected on a Shimadzu UV-2501 PC spectrophotometer.

The mass weight of the protein subunit was determined by an electrospray ionization mass spectrometry (ESI-MS) via a triple quadrupole instrument (API III, Applied Biosystems). An m/z 600–2,200 range was scanned (positive mode, orifice 90 V, 0.3 Da step size, 5.61 s/scan). Data were processed and analyzed using MacSpec 3.3, Hypermass and BioMultiview 1.3.1 software (Applied Biosystems).

The mass weight of the native protein was determined by a HPLC (Agilent 1200 series) fitted with a size exclusion column (Tosoh Bioscience, TSK gel G2000SW 7.5 mm ID X 30 cm) at a flow rate of 0.5 mL/min. The column was calibrated using five standards: bovine thyroglobulin (670 kDa), bovine γ-globulin (158 kDa), ovalbumin (44 kDa), horse myoglobin (17 kDa), and vitamin B12 (1.35 kDa).

Results

Tetramer versus Dimer. *Ca*MnSODc was overexpressed and purified from *S. cerevisiae*, with 0.6 equiv of manganese per subunit as determined by ICP-MS. The subunit mass weight is 22.7 kDa as determined by ESI-MS. The purity was confirmed by SDS-PAGE gel (Figure S3.2). *Ca*MnSODc has been reported to be a homotetramer (13), but our investigation of the native protein using gel filtration chromatography indicates that its molecular weight in solution under our conditions is ~46 kDa, corresponding to a homodimer (Figure 3.1). It should be noted, however, that we found that *Ca*MnSODc crystallized as a tetramer under other conditions (see below). *Sc*MnSOD, in contrast to *Ca*MnSODc and analogous to the human MnSOD, is a homotetramer under our conditions, although the two yeast enzymes share great sequence similarity.

Kinetic Studies. Solutions containing 1 μM MnSOD at pH 7 were pulse irradiated and the disappearance of O_2^- was followed at 260 nm; see Figure 3.2. The traces we collected for both *Ca*MnSODc and *Sc*MnSOD were plotted along with previous data collected under identical conditions for MnSOD from human, *E. coli* and *D. radiodurans* (2,3). When the O_2^- concentration was seven-fold excess over the enzyme, human MnSOD already showed a depressed activity, yet the O_2^- disappearance as a function of time was similar for the other four

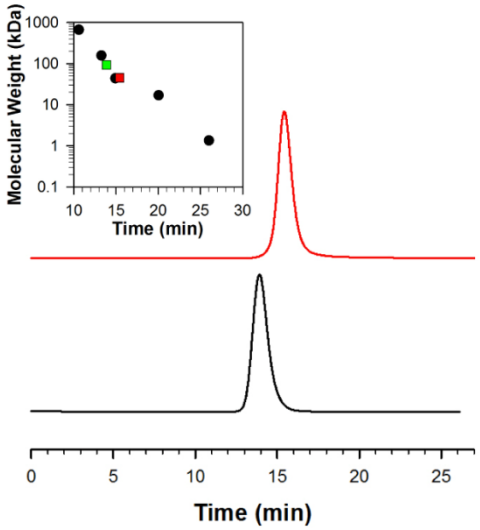

Figure 3.1. The HPLC-SEC profiles of *Ca*MnSODc (a) and *Sc*MnSOD (b). Inset: The plot of the molecular weight of the five standards (black, circles), *Sc*MnSOD (green, triangle) and *Ca*MnSODc (red, square) versus their retention time. The concentration of proteins loaded into the column is 6 mg/mL. The column was calibrated using five standards: 1) bovine thyroglobulin (670 kDa), 2) bovine γ-globulin (158 kDa), 3) ovalbumin (44 kDa), 4) horse myoglobin (17 kDa), and 5) vitamin B12 (1.35 kDa). The buffer contained 50 mM sodium phosphate (pH 6.7) and 50 mM sodium chloride.

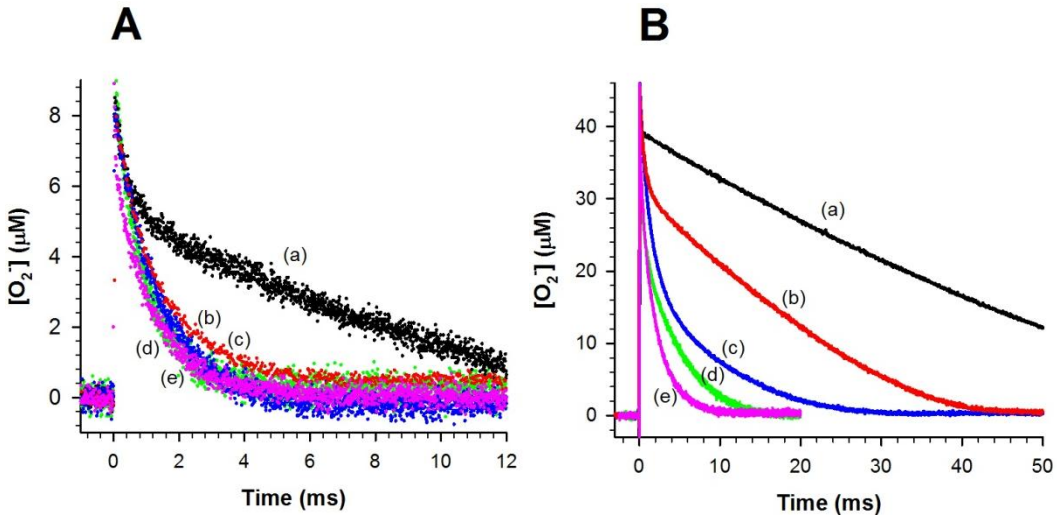

Figure 3.2. Decay of 7 μM (A) and 41 μM (B) O_2^- catalyzed by 1 μM (in Mn) human (a, black), *E. coli* (b, red), *D. radiodurans* (c, blue) MnSOD, *Sc*MnSOD (d, green) and *Ca*MnSODc (e, pink). The sample for pulse radiolysis contained 10 mM potassium phosphate (pH 7), 10 mM sodium formate and 10 μM EDTA. The O_2^- concentration in these figures is calculated from the absorbance at 260 nm.

enzymes and could be fit to a first-order process (Figure 3.2A). When the ratio of $[O_2^-]$:MnSOD increased to 41, the five MnSODs displayed dramatically different efficiencies at removing O_2^- (Figure 3.2B), which scale as *Ca*MnSODc > *Sc*MnSOD > *D. radiodurans* (*Dr*MnSOD) > *E. coli* (*Ec*MnSOD) > human MnSOD. For human and *E. coli* MnSOD, the O_2^- decay was characterized by a fast decrease, followed by a slow almost zero-order phase. It is the biphasic nature of the trace that suggests dismutation proceeded by a fast catalytic pathway and a slower, concomitant product-inhibited pathway. The gating values for these two enzymes are 1 and 5 respectively (2). The trace obtained for the *Dr*MnSOD showed a much less distinct plateau region and fitting the data yielded a gating value of 12 (3). Our earlier study of the reaction of *Sc*MnSOD with high O_2^- concentrations led to a calculated gating value k_2/k_3 to be 16-20, indicating that the fast protonation pathway dominates (4).

*Ca*MnSODc removes high concentrations of O_2^- even more efficiently than *Sc*MnSOD. Here, k_2 of *Ca*MnSODc was determined to be 1.0×10^9 $M \cdot s^{-1}$ by following the appearance of Mn^{3+}SOD (λ_{max} = 480 nm; see method, Figure S3.3) as *Ca*Mn^{2+}SODc was oxidized by substoichiometric amounts of O_2^-. However, at physiological pH (6.5–7.5), *Ca*MnSODc removed various concentrations of O_2^- ($[O_2^-]$:[MnSOD] from 2–48:1) at similar rates, showing that only minimal product inhibition occurred under these conditions. Even at $[O_2^-]$:MnSOD ratios as high as 48, the activity of *Ca*MnSODc was comparable to that of *S. cerevisiae* CuZnSOD, an enzyme that does not exhibit product inhibition (Figure S3.4). The disappearance of O_2^- catalyzed by *Ca*MnSODc could be fitted to a first-order process.

To achieve such a high efficiency, *Ca*MnSODc would either carry such a high gating ratio (k_2/k_3) that the reaction of Mn^{2+}SOD with O_2^- proceeds almost completely via the fast protonation (reaction 2), or it has such a high dissociation rate (k_4) that the product-inhibited

complex decomposes before it is detected during pulse radiolysis (reaction 4). Assuming that k_4 is 50 s^{-1}, which is close to that of bacterial dimeric MnSODs, the calculated k_2/k_3 is 65. Assuming that k_2/k_3 is 20, which is comparable to that for *Sc*MnSOD, k_4 is calculated to be 210 s^{-1}. The latter scenario is more likely, because a dissociation rate of 210 s^{-1} is not dramatically different from a k_4 of 130 s^{-1} for human MnSOD and 90-140 s^{-1} for *Sc*MnSOD. In addition, dissociation rates as large as 1000 s^{-1} have been reported in human Y34 mutants (24). A k_2/k_3 ratio of 65, however, is three times as large as the gating ratio of *Sc*MnSOD, the least inhibited MnSOD that has been characterized to date. Therefore, the high efficiency of *Ca*MnSODc is more likely due to the fast dissociation of the inhibited complex from the metal center.

Previous studies have shown that the rate of enzymatic catalysis as a function of pH is different for the human and bacterial MnSODs. Given that a major difference between the human and bacterial MnSODs is that the former is a tetramer while the latter are dimers, we compare here two yeast MnSODs, where one is a dimer and the other is a tetramer. In these studies we were initially interested only in the change in the fast catalytic cycle (k_1 and k_2), which was measured by following the disappearance of O_2^- in the presence of *Sc*MnSOD or *Ca*MnSODc under conditions where the $[O_2^-]$:MnSOD ratio was between 1 and 3. The overall activity of both *Sc*MnSOD and *Ca*MnSODc decreased considerably as pH was increased (Figure 3.3). Both yeast enzymes resemble *Ec*MnSOD, with a relatively constant activity up to pH 9, but are distinct from human MnSOD, where catalysis is relatively unchanged even up to pH 11. It is surprising that *Sc*MnSOD and *Ca*MnSODc are different in their quaternary structure, yet they exhibit such similar pH dependence. It is notable that the yeast MnSODs are even more sensitive to the change of pH than the bacterial MnSODs. The p*K* is ~8.5 in two yeast MnSODs, ~9.5 in *Ec*MnSOD and ~10.5 in human MnSOD. Adjusting the pH of yeast MnSOD sample solutions

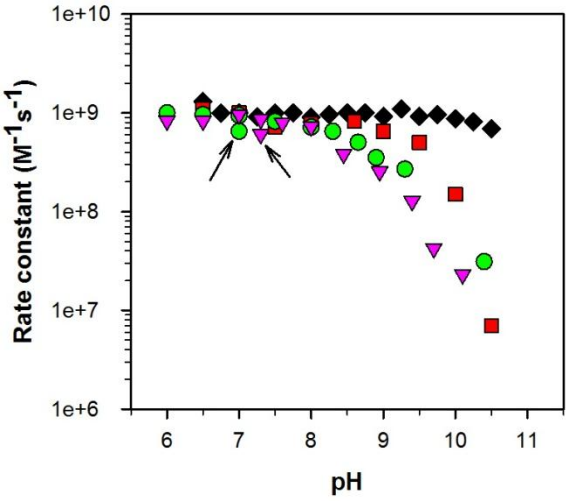

Figure 3.3. Effects of pH on the overall activity of MnSODs. The rate constant was determined by fitting the disproportionation of low doses of O_2^- ($[O_2^-]$:MnSOD from 1–3) to a first-order process. Under these $[O_2^-]$:MnSOD ratios, the reaction of Mn^{2+}SOD with O_2^- proceeds predominantly through the outer-sphere pathway. This rate constant reflects a combination of k_1 and k_2. MnSOD is from human (black, diamonds), *E. coli* (red, rectangles), *S. cerevisiae* (green, circles) and *C. albicans* (pink, triangles). The data points marked with an arrow correspond to the rate constants measured for the yeast enzymes after adjusting the pH of sample solution from 9.5 to neutral.

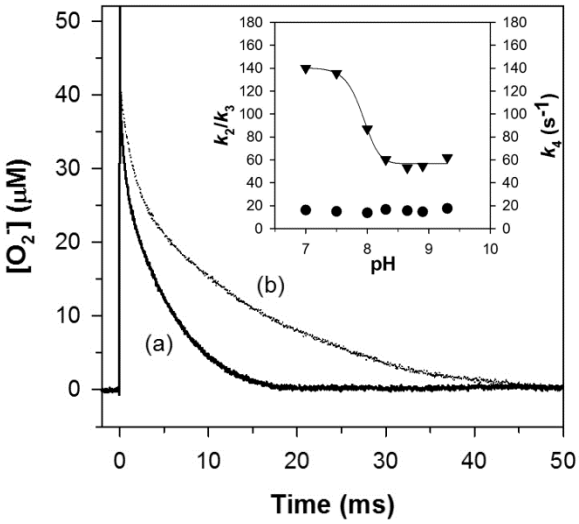

Figure 3.4. Dependence of the level of product inhibition of *Sc*MnSOD on pH. Decay of 48 μM O_2^- catalyzed by 1 μM (in Mn) *Sc*MnSOD at pH 7.5 (a) and 8.9 (b). Inset: Dependence of the values of k_2/k_3 (circles) and k_4 (triangles) of *Sc*MnSOD on pH. The sample for pulse radiolysis contained 10 mM potassium phosphate (pH 7), 10 mM sodium formate and 10 μM EDTA.

from 9.5 back to 7 resulted in the restoration of their activity to ~50% of that of the intact enzymes (Figure 3.3).

pH also has an impact on the level of product inhibition exhibited by *Sc*MnSOD. The slow almost zero-order phase, which is a sign of the saturation of MnSOD by O_2^-, was discernable from the reaction of high concentrations of O_2^- ($[O_2^-]$:MnSOD = 48:1) with *Sc*MnSOD at pH 8.9 (Figure 3.4). This feature was barely seen under the same conditions at pH 7.5. The gating ratio k_2/k_3 and the dissociation rate k_4 were calculated by fitting the O_2^- decay into the four-reaction mechanism (Scheme 3.2; Figure 3.4, inset). The calculated k_2/k_3 is a constant value over the pH range of 7–9.5. The dissociation rate k_4, however, dramatically decreases when pH is raised to 8 and reaches a plateau at pH ~8.5 with a p*K* of ~8. Due to a depressed k_4, the dissociation of H_2O_2 from the active site may become the rate-limiting step at high pH, resulting in a more inhibited *Sc*MnSOD. The values of k_2/k_3 and k_4 of *Sc*MnSOD were difficult to calculate at pH > 9.5, at which point k_1 and k_2 corresponded to the rate-limiting steps of the reaction. In the case that k_4 stays constant at the plateau while k_1, k_2 and k_3 continue decreasing at pH >9.5, the dissociation of the inhibited complex may occur faster than its formation, leading to a decay of O_2^- at pH >9.5 that appeared to be non-inhibited.

*Ca*MnSODc, in contrast, did not show a pronounced occurrence of the slow zero-order phase even at elevated pH (Figure S3.5). The decay of O_2^- over the pH range of 7–9.5 could still be fit to a first-order process (R^2 = 1.5). In this case it is difficult to calculate either the ratio of k_2/k_3 or the value of k_4 based on fitting.

Oxidation State. Our previous work showed that tetrameric *Sc*MnSOD, unlike all other wild-type MnSODs studied thus far, is isolated predominantly in the 2+ oxidation state (4). Dimeric *Ca*MnSODc, structurally similar to bacterial MnSODs, is also isolated in the Mn^{2+} state

(Figure S3.6-A). The two enzymes from yeast are also very similar with respect to the thermodynamics of oxidation and reduction. From this point on, if the results are very similar for the two yeast MnSODs, data from only one enzyme are shown.

The optical absorption spectrum of as-isolated *Sc*MnSOD has a very weak visible absorption band around 480 nm (Figure 3.5A) that suggests that a small amount of Mn^{3+}SOD is present along with a significantly larger amount of Mn^{2+}SOD. The addition of sodium hyposulfite fully reduced the enzyme and completely quenched this absorption intensity (Figure 3.5A). Based on the difference in absorption between the fully reduced and the as-isolated enzyme (Figure 3.5A, insert) and using the extinction coefficient for Mn^{3+}SOD obtained from pulse radiolysis (ε_{475} = 780 $M^{-1}cm^{-1}$), ~5% of the as-isolated enzyme is oxidized. The oxidized enzymes found in both as-isolated *Sc*MnSOD and *Ca*MnSODc have spectra that differ from those of most reported Mn^{3+}SODs in that additional absorption intensity at ~390 nm is visible (Figure 3.5A, inset; Figure S3.6-A, inset). They are, however, similar to the spectrum of *Sc*Mn^{3+}SOD that was reported previously (25).

Oxidation of as-isolated *Sc*Mn^{2+}SOD or *Ca*Mn^{2+}SODc by 0.75 equivalents of potassium permanganate rapidly gave absorption spectra characteristic of 5-coordinate Mn^{3+}SOD with a maximum at 480 nm (Figure 3.5B, S6-B) with no residual absorbance of permanganate. Both yeast MnSODs remained oxidized in solution and retained full activity as determined by pulse radiolysis. Interestingly, an absorption intensity around 390 nm increased slowly over time (Figure 3.5B, S6-B). Based on the difference between the immediately scanned and the final spectrum (Figure S3.7), a Mn^{3+}-containing species different from the 5-coordinate Mn^{3+}SOD was formed over time. Further addition of 1 equivalent of sodium ascorbate selectively bleached the absorption of *Sc*Mn^{3+}SOD or *Ca*Mn^{3+}SODc around 390 nm, yielding the characteristic 5-

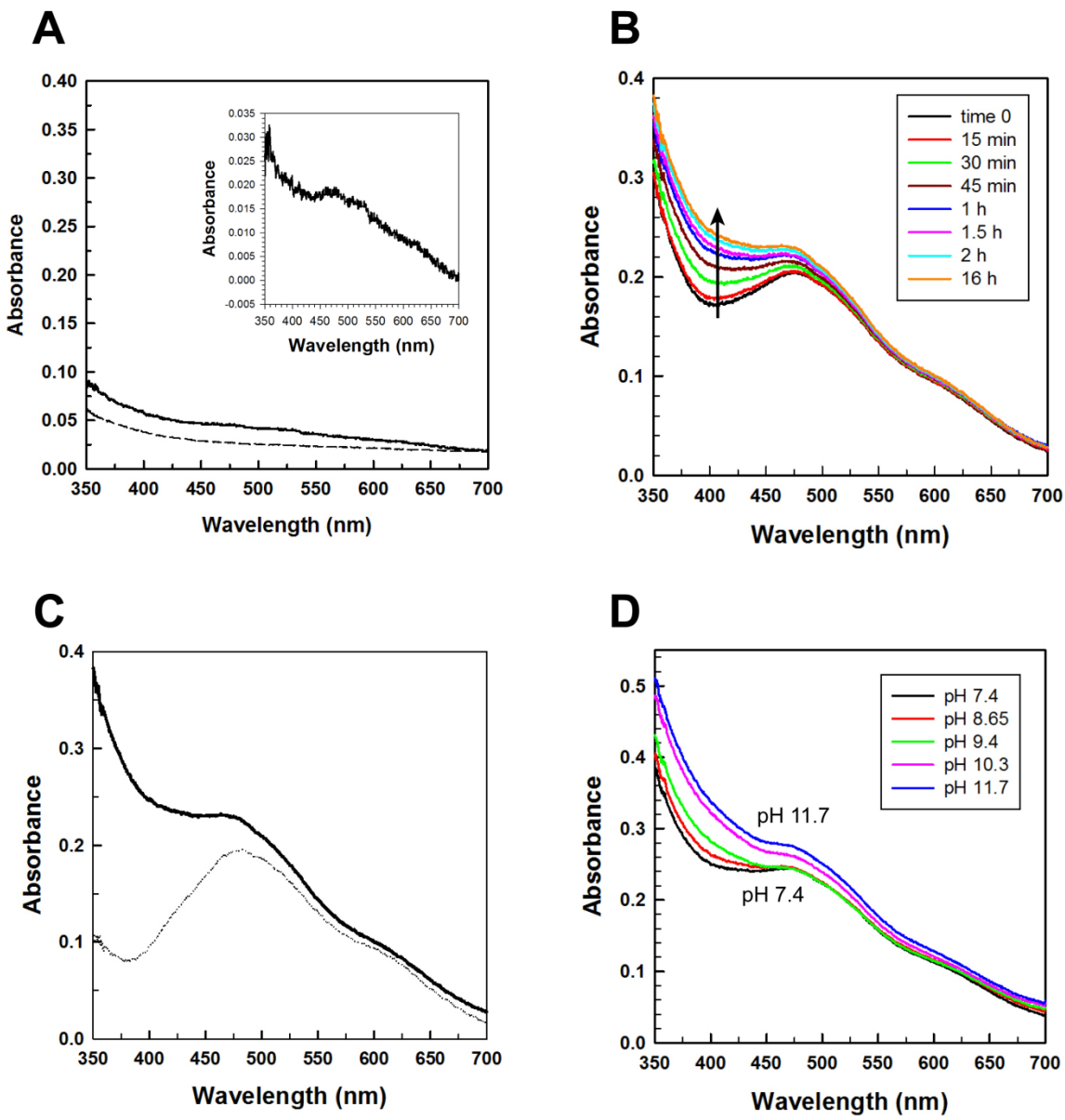

Figure 3.5. The oxidation state of *Sc*MnSOD. (A) Optical spectra of as-isolated *Sc*MnSOD (solid line) and *Sc*MnSOD reduced by sodium hydrosulfite (dashed line). Inset: The difference spectrum between as-isolated and reduced *Sc*MnSOD. (B) Optical spectra of *Sc*MnSOD oxidized by potassium permanganate ([$KMnO_4$]:MnSOD = 0.75:1) at pH 7.4 as measured over time. Time 0 refers to the start of the first scan immediately after mixing $KMnO_4$ with the enzyme. (C) Reduction of *Sc*Mn^{3+}SOD (solid line, oxidized by 0.75 equiv of $KMnO_4$ and allowed to equilibrate at room temperature for 2 hr) by one equiv of sodium ascorbate (dotted line). (D) Optical spectra of *Sc*Mn^{3+}SOD at different pH. The sample solutions contained 190 μM (in Mn) enzyme in 25 mM potassium phosphate (pH 7.4).

coordinate Mn^{3+}SOD spectrum (Figure 3.5C, S6-C), which has been reported previously (25). Treatment of the yeast enzymes with 10-fold molar excess of ascorbate yielded the completely reduced enzymes. Therefore, the unknown species is kinetically more prone to reduction by ascorbate than the well-characterized 5-coordinate species. In contrast, In contrast, 0.5 equivalent of H_2O_2 reduced the 5-coordinate Mn^{3+} and the unknown species simultaneously in one equivalent of yeast Mn^{3+}SODs, giving optical spectra of full reduced MnSOD (data not shown). The slow formation of the 6-coordinate adduct and its susceptibility to reduction by ascorbate are very puzzling, and we will continue exploring the explanation in future.

One species known to absorb around 390 nm is the low-temperature *Ec*Mn^{3+}SOD:azide adduct. At room temperature, the 5-coordinate *Ec*Mn^{3+}SOD binds azide in such a fashion that the coordination number of the Mn ion does not change. At lower temperatures (pK = 200 K) this adduct transforms into an inner-sphere 6-coordinate azide-Mn^{3+}SOD complex (26). The room-temperature spectrum of azide-treated *Sc*Mn^{3+}SOD shows a shift of the absorption band similar to that observed in other azide-Mn^{3+}SODs (26) (Figure S3.8). However, there remains additional intensity at 390 nm that is reminiscent of the features present in the spectrum of the low-temperature azide adduct of *Ec*Mn^{3+}SOD where azide is directly bound to the Mn ion. This may indicate that the unknown species in *Sc*Mn^{3+}SOD is also 6-coordinate.

The measurement of the redox potential of MnSOD is notoriously difficult. Our electrochemical studies on *Sc*MnSOD and *Ca*MnSODc failed to achieve efficient electron transfer between the electrode and the enzymes and thus only yielded an approximation of their redox potential as ~0.3 V. This value is comparable to those determined for *E. coli* (0.3 V) (27) and human (0.4 V) (28) MnSOD, which are a reflection of the redox potential of the 5-coordinate

Mn^{3+}SOD species. The redox potentials of human and *E. coli* MnSOD are close to that of ascorbate$^{\bullet-}$, H^+/ascorbateH^- ($E°$ = 282 mV) at neutral pH.

The Mn^{3+}SOD spectra obtained from pulse radiolysis, in which *Sc*Mn^{2+}SOD or *Ca*Mn^{2+}SODc was oxidized by substoi-chiometric amount of O_2^- (see method), merely showed formation of the well characterized 5-coordinate Mn^{3+}SOD (4) and were comparable to those of other Mn^{3+}SODs (3,29) (Figure 3.6). However, the time scale of each single measurement at each wavelength was shorter than 1 ms. Over 10 ms the reduction of yeast Mn^{3+}SODs by excess H_2O_2 was discernable. Therefore, the generation of the putative L-Mn^{3+}SOD species likely occurred more slowly under pulse radiolysis conditions than the reduction of the 5-coordinate Mn^{3+} center by H_2O_2. Indeed the shifting of the spectrum around 390 nm was discernable in a much longer timescale (> 10 min) from the oxidation of as-isolated *Sc*MnSOD using ^{60}Co radiation as the source of O_2^- (Figure S3.9).

MnSODs that are isolated in the Mn^{3+} state possess absorption spectra that change modestly as pH is raised. For example, at pH > 9 the 478 nm absorption feature corresponding to *Ec*Mn^{3+}SOD begins to diminish slightly in intensity and shifts to shorter wavelength. This p*K* event has been ascribed to deprotonation of Tyr34 (numbering in *Sc*MnSOD) (30). However, for *Sc*MnSOD and *Ca*MnSODc the absorption intensity around 390 nm increased as pH was increased (Figure 3.5D, S6-D). *Sc*MnSOD and *Ca*MnSODc may not have the same p*K* as other Mn^{3+}SODs, or the spectral change due to the p*K* may have been obscured by the absorption shifting around 390 nm. The Mn^{3+} spectra of *Sc*MnSOD obtained from pulse radiolysis at pH 7 and 10 were compared, and a roughly 20% decrease in intensity but no shift in peak for the Mn^{3+}SOD absorbance at 480 nm were observed (Figure S3.10). The spectral shift over pH

indicates that the sixth ligand is likely a hydroxide that with a higher concentration binds to Mn^{3+} more readily at high pH.

EPR Spectra. In agreement with the electronic absorption data shown above, results from perpendicular-mode X-band EPR experiments confirm that *Ca*MnSODc is isolated predominately in the Mn^{2+} oxidation state (Figure S3.11-A). These spectra are similar to those obtained for *Ec*Mn^{2+}SOD with five separate electronic spin transitions observed due to zero-field splitting of the manifold of spin levels of the high-spin (S = 5/2) Mn^{2+} ion. These resonances are further split by the hyperfine interaction of the electron spin with the ^{55}Mn nuclear spin (I = 5/2). The corresponding parallel-mode EPR spectrum for as-isolated *Ca*MnSODc possesses little intensity (Figure S3.11-B). In contrast, the spectra of the pH 7.65 permanganate-oxidized samples have at least eight intense transitions centered at 80 mT (g = 8.4) (Figure 3.7A) that are somewhat similar to the six parallel-mode EPR transitions separated by ≈10 mT observed previously for *Ec*Mn^{3+}SOD (31). Campbell *et. al.* (31), showed that these signals arise from transitions within the $m_S = |\pm 2\rangle$ manifolds of a high-spin (S = 2) Mn(III) system. Analysis of the temperature-dependence of the integrated signal intensity led to an evaluation of the magnitude and, importantly, sign of the zero-field splitting parameters—D = +2.10 cm^{-1} and E = 0.24 cm^{-1}. (NOTE: These values are consistent with those determined by analysis of variable-temperature, variable-field magnetic circular dichroism saturation behavior (32).) That $D > 0$ indicates that the lowest unoccupied metal-centered molecular orbital (MO) is $3d_z^2$-based (33). These conclusions are borne out by the trigonal bipyramidal coordination geometry of the Mn^{3+} site determined by X-ray crystallography as well as results of numerous electronic structure calculations (34).

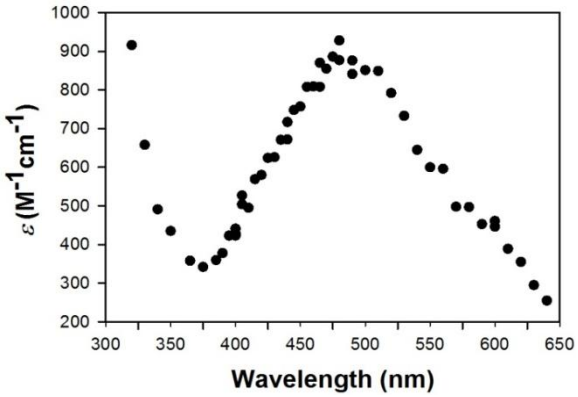

Figure 3.6. The Mn^{3+}SOD spectrum of *Ca*MnSODc obtained from pulse radiolysis. The pulse radiolysis sample contained 60 μM (in Mn) *Ca*MnSODc in 10 mM potassium phosphate (pH 7), 10 mM sodium formate and 100 μM EDTA. The enzyme was reduced prior to each pulse with 120 μM H_2O_2.

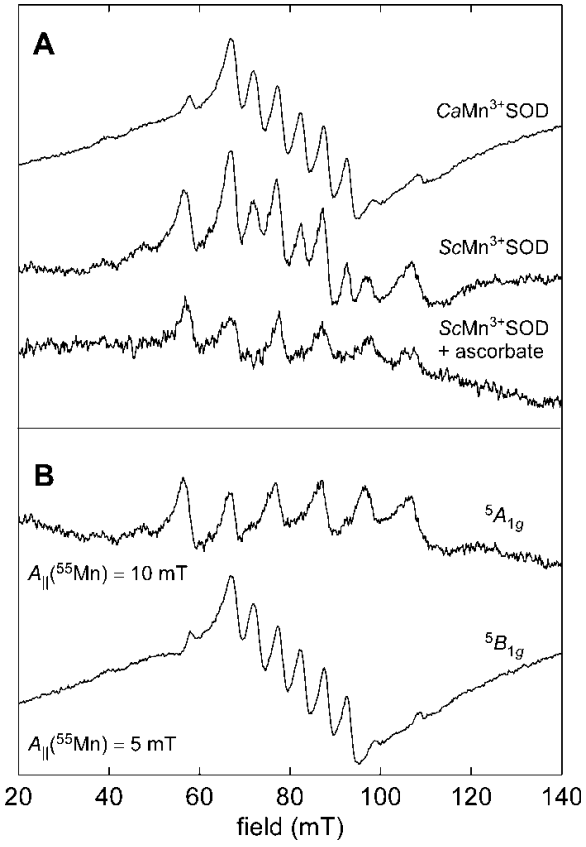

Figure 3.7. (A) Parallel-mode CW EPR spectrum of *Ca*Mn^{3+}SODc and *Sc*Mn^{3+}SOD oxidized by potassium permanganate ([*Sc*MnSOD]:$KMnO_4$ = 1:0.75) and of *Sc*Mn^{3+}SOD treated with 1 equivalent of sodium ascorbate. (B) The deconvolution of the two spectra (top two spectra in panel A) of the permanganate-oxidized species shows two components, one assigned to a Mn^{3+} center with a $5A_{1g}$ ground state and one with a $5B_{1g}$ ground state. Instrument settings: ν = 9.3959 GHz; microwave power = 32 mW; sweep rate = 1.81 mT/s; temp = 4.9 K.

In the present case of *Sc*Mn^{3+}SOD and *Ca*Mn^{3+}SODc, more than six parallel-mode resonances are observed, indicating that there are at least two Mn^{3+}-containing species present in the sample. Subtraction of the EPR spectrum of *Ec*Mn^{3+}SOD from that of *Sc*Mn^{3+}SOD reveals an underlying sextet with interpeak spacings of approximately 4.5−5.0 mT (Figure 3.7B). Such a small effective ^{55}Mn hyperfine coupling parameter ($A_{\|}$) has been observed previously for several 6-coordinate Mn(III) centers (33,35,36). There has also been a preliminary report that showed a fraction of 5-coordinate *Ec*Mn^{3+}SOD converts to a new species at pH 11.54 that is characterized by a parallel-mode EPR spectrum with $A_{\|}(^{55}\text{Mn})$ = 3.3 mT (31).

The dramatic difference in $A_{\|}$ for the two spectroscopically distinct *Sc*Mn^{3+}SOD species is likely resulted from a change in the electronic ground state for the Mn^{3+} ion—from $5A_{1g}$ to $5B_{1g}$ (33). Respectively, these states correspond to d-electron configurations wherein the $3d_z^2$-based and $3d_{x^2-y^2}$-based MOs are empty. A simple explanation for this change would be a new, strong ligand binding in the equatorial plane to the Mn^{3+} ion. This event would raise the energy of the $3d_{x^2-y^2}$-based MO allowing the fourth d-electron to occupy the $3d_z^2$ orbital instead.

The EPR transition observed for both electron configurations is between the $m_S = |\pm 2\rangle$ spin levels. For the $5B_{1g}$ state, the axial zero-field splitting interaction (D) will be negatively signed, putting the $|\pm 2\rangle$ manifold lowest in energy. Thus this manifold will be populated at all temperatures and if the energy splitting (Δ) of the $m_S = |\pm 2\rangle$ spin levels at zero field is less than the energy of the incident microwave radiation ($h\nu$ = 0.319 cm−1 for the 9.396 GHz radiation employed here) a parallel-mode EPR transition will be observed. However, for the $5A_{1g}$ state, the sign of D is positive and the $|\pm 2\rangle$ manifold will not be populated at low temperatures. For *Ca*Mn^{3+}SODc, increasing the temperature thermally populates this manifold and the EPR transition becomes apparent. By monitoring the temperature-dependent intensity of the peak at

58 mT we have determined that D = +1.90 cm^{-1} and E = 0.20 cm^{-1}, values similar to those found for the 5-coordinate form of *Ec*Mn^{3+}SOD (see Figure S3.12).

Upon treatment of *Sc*Mn^{3+}SOD with 1 equivalent of ascorbate, the $5B_{1g}$ contribution to the parallel-mode EPR spectrum completely disappears (compare second and third traces in Figure 3.7A). This spectral change coincides with bleaching of the 390 nm feature in the electronic absorption spectrum (Figure 3.5C) upon addition of ascorbate, suggesting the narrowly split EPR signal and the 390 nm absorption intensity are spectral signatures of the same species.

Crystal Structure. The active site structure of the two yeast MnSODs was investigated by crystallography (Tabls S3.1). The crystals of both yeast MnSODs are colorless. The X-ray crystallography structure of *Sc*MnSOD is always a tetramer (Figure S3.13-A). To our surprise, the quaternary structure of *Ca*MnSODc varied with crystallization conditions. It is either a dimer (data not shown) or a tetramer (Figure S3.13-B). We believe that the quaternary structure of *Ca*MnSODc depends on buffer condition (ion strength and viscosity) and protein concentration, and we will explore the factors that control its quaternary structure in a future publication.

*Sc*MnSOD and *Ca*MnSODc both maintain the 5-coordinate sphere of manganese conserved in all other MnSODs (Figure 3.8) (34,37-40). Their active sites are superimposable, giving a root mean square deviation (RMSD) of 0.20 Å (Figure S3.14). For both enzymes the observed manganese bond lengths are ~2.2 Å to each His NE2, 2.0 Å to Asp OD2, and 2.3 Å to OH2 (Tabls S3.2). These are only slightly longer than the corresponding distances in MnSODs that rest predominantly in the Mn^{3+} state. Spectroscopic and computational evidence suggests that in the reduced state Mn is bound by a water molecule and in the oxidized state it is bound by a hydroxide (41). The distance of the Mn–O bond should be farther in the bound water as it is not

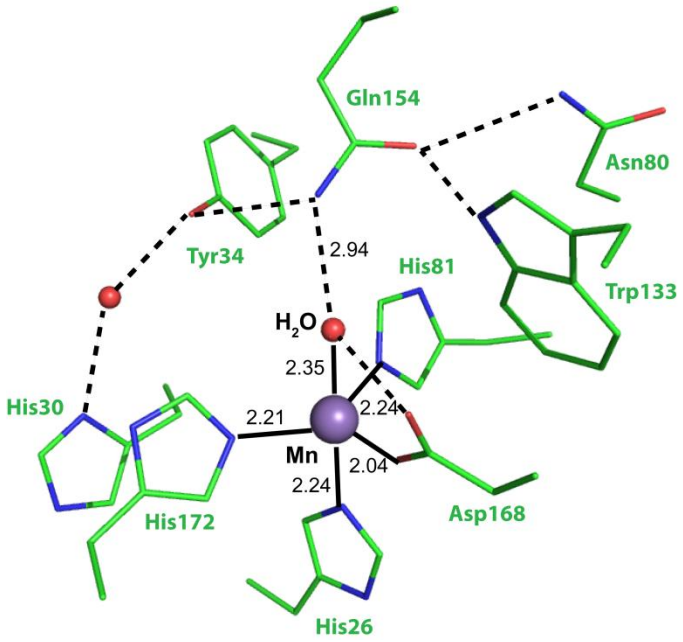

Figure 3.8. Active site structure of *Sc*MnSOD, showing the coordination sphere of manganese (chain A). Some second coordination sphere residues are also shown. Coordination and hydrogen bonds are indicated as solid and dashed lines, respectively.

as strong a bond and closer in the bound hydroxide. The long Mn–O (solvent molecule) distances in both yeast MnSODs are consistent with Mn^{2+}–OH_2 moieties. Although these shifts are small and within possible experimental error, the observed longer coordination bond distances could reflect the 2+ oxidation state of *Sc*MnSOD and *Ca*MnSODc.

During X-ray crystallography data collections, metalloenzyme crystals are likely to be reduced by photo-electrons generated from the excitation of protein and solvent atoms by the incident X-ray beam (42). As *Sc*MnSOD and *Ca*MnSODc are both isolated in the reduced form as indicated by their optical and EPR spectra (Figure 3.5, S6 and S11), the X-ray structures are certainly those of the reduced (Mn^{2+}SOD) enzymes. For other MnSODs that are isolated in the Mn^{3+} oxidation state, active site bond distances measured in their X-ray structures (Tabls S3.2) would suggest that the human and *Thermus thermophilus* crystals contained primarily Mn^{3+}SOD and the remaining MnSODs were likely primarily reduced during the data collection.

Discussion

The Relationship of Product Inhibition to Active Site Structure. Based on the structural and sequence similarity shared between *Sc*MnSOD and human MnSOD, *Sc*MnSOD was expected to exhibit a level of product inhibition similar to human MnSOD. However, we found that *Sc*MnSOD is dramatically gated toward the fast protonation pathway. *Ca*MnSODc resembles *Sc*MnSOD in its efficiency of removing O_2^- at high O_2^- doses. The yeast MnSODs are more like bacterial MnSODs in terms of function. Our studies on yeast MnSODs place human MnSOD in a unique class that predominantly undergoes the product-inhibited pathway at high levels of O_2^- among MnSODs that have been characterized to date.

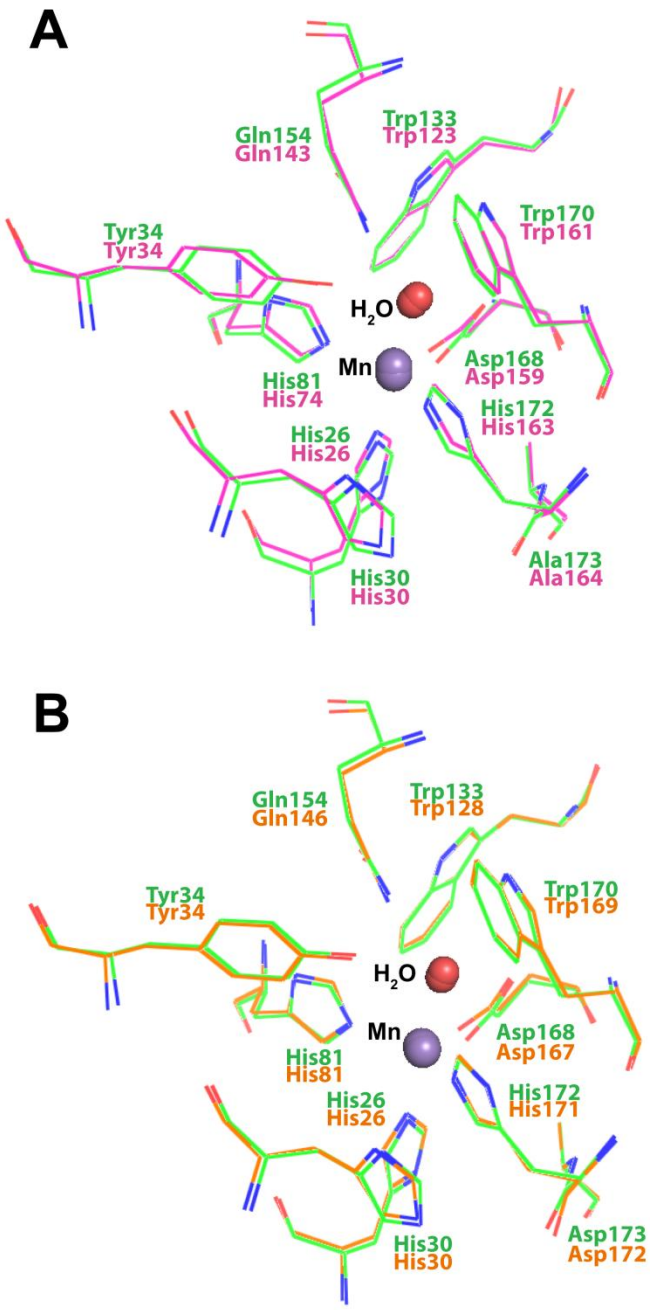

Figure 3.9. Superposition of the first and second coordination sphere of *Sc*MnSOD to that of human MnSOD (pink, A) and *Ec*MnSOD (yellow, B).

Numerous studies on the structure-function relationship of MnSOD have been focused on the structure of second coordination sphere structure (24,43-47), which is highly conserved in MnSOD from different organisms (34,37-39). Superposition of all active site residues (within 6 Å of Mn) of *Sc*MnSOD on those of human or *E. coli* MnSOD gives RMSD of 0.25 and 0.18 Å, respectively (Figure 3.9), indicating that in terms of second coordination sphere, *Sc*MnSOD resembles *Ec*MnSOD more than it does human MnSOD, in spite of the fact that *Sc*MnSOD and human MnSOD are both tetramers and share greater sequence similarity. Of particular significance are highly conserved residues Tyr34 and His30, mutations of which usually cause changes in product inhibition (24,48). Their positions in *Sc*MnSOD overlap more with those in *Ec*MnSOD than with those in human MnSOD (Figure 3.9). One would expect subtle shifts of these residues in the second coordination sphere to cause dramatic differences in the degree of product inhibition among MnSOD from different species. The factors that control the level of product inhibition will be subjects of future investigations.

The Unusual Resting State of Yeast MnSODs and the Role of Gln154. In contrast to human and bacterial MnSODs that rest predominantly as Mn^{3+}SOD, the as-isolated proteins of yeast MnSODs are both ~95% reduced. Our preliminary electrochemical results indicate that the redox potentials of yeast MnSODs are comparable to those determined for human and bacterial MnSODs. However, previous studies on *Ec*MnSOD have shown spontaneous oxidation of *Ec*Mn^{2+}SOD in air (29), which does not occur in yeast MnSODs. Therefore, the unusual resting state of the yeast enzymes may result from thermodynamically driven shifts in oxidation-reduction equilibria.

The fact that yeast MnSODs rest as Mn^{2+}SOD could be linked with the positioning of an outer-sphere residue, Gln154 (the numbering in *Sc*MnSOD; *Ca*MnSODc: Gln163; human:

Gln143; *E. coli*: Gln146). Conserved in all Mn and FeSODs, Gln154 donates an H-bond to the metal-bound solvent molecule, and is the only contact of the metal-bound solvent molecule to the protein beyond the active site. Gln154 makes three hydrogen bonds to three highly conserved residues, Tyr34, Asn80 and Trp133 (numbering in *Sc*MnSOD). Its hydrogen bonding potential is fully utilized and Gln154 seems firmly fixed in place. Gln154 together with Asp168 that is an H-bond acceptor from the metal-coordinated H_2O or OH^-, determine the position of the coordinated solvent molecule. Mutagenesis on Gln154 often causes dramatic depression of reactivity (43,44,46), indicating the key role of the NE2(Gln154)···O(solv) bond.

The active site reduction midpoint potential (E_m) contributes directly to the driving forces of the two half reactions of O_2^- dismutation. In Mn and FeSOD (structural homologs), Gln154 is critical in modulating E_m and thus contributes to the ion specificity as well as determining the resting state of Mn and FeSOD (12,49). The second coordination sphere of Mn and FeSOD is similar except that the Gln154 amide nitrogen is ~0.7 Å further from the metal in FeSOD. DFT calculations on the structure of Mn and FeSOD suggest the reason of MnSOD resting predominantly in the Mn^{3+} state as the destabilization of coordinated H_2O vs. OH^- by the closely placed glutamine side chain (12,50). In Mn-substituted *Ec*FeSOD in which Mn is placed away from Gln69, the E_m is elevated by 670 mV and the enzyme completely rests as the reduced form (51). Mutation of Gln143 to asparagine in human MnSOD also causes the enzyme to rest as Mn^{2+}SOD (43). Either *Ec*Mn(Fe)SOD or human Q143 mutants is only able to catalyze one half reaction, the oxidation of O_2^- (43,51).

Most MnSODs with solved structure conserve a NE2(Gln154)···O(solv) H-bond of 2.85–2.95 Å (Tabls S3.2), and, as indicated by previous studies, the further the Gln154 amide nitrogen is away from Mn, the more the 2+ state is favored by the enzyme. Thus, the observation that the

distance of Gln154 to Mn is slightly longer in the two yeast MnSODs (4.79 and 4.73 Å in *Sc*MnSOD and *Ca*MnSODc, respectively) than in the MnSODs that predominantly rest in the oxidized form (Human: 4.65 Å; *E. coli*: 4.64 Å; *D. radiodurans*: 4.54 Å; *Caenorhabditis elegans*: 4.54 Å) may be related to fact that the yeast MnSODs rest in the reduced state.

The Relationship of Product Inhibition of Human MnSOD to H_2O_2 Signaling in Mammals. Human MnSOD is much less efficient at turning O_2^- into H_2O_2 than *Sc*MnSOD when O_2^- levels are high, although the two enzymes share great sequence similarity and are both located in mitochondria. Mitochondria are recognized as the main source of O_2^- with the production occurring through respiratory chain. H_2O_2 is generated in mitochondrial matrix via the dismutation reaction of O_2^- catalyzed by MnSOD. The produced H_2O_2 then diffuses into cytosol. The roles of H_2O_2 are complex in higher organisms. In mammalian cells the upregulated expression of antioxidant enzymes is not a universal response to supraphysiologic levels of H_2O_2 (7). Instead, physiologic levels of H_2O_2 stimulate cell division, transformation, migration or apoptosis (7,8,10,11). This along with the fact that mammalian cells generate H_2O_2 in response to various stimuli supports that H_2O_2 is utilized as a signaling agent in numerous mammalian signaling pathways (7-11,52,53). A well established H_2O_2-induced signaling is the modulation of the tyrosine phosphorylation of proteins by causing the oxidative inhibition of tyrosine phosphatases (9). Reversible inactivation of tyrosine phosphatases has been demonstrated to play a critical role in protein tyrosine phosphatase (PTP) and insulin signaling (54,55). Several mitochondrial signaling pathways are stimulated by increased H_2O_2, including tumor necrosis factor (TNF)-α-induced apoptosis (56) and c-Jun NH_2-terminal kinase (JNK)-induced apoptosis (52,57). The participation of H_2O_2 in signaling cascades may require tight regulation of its production in mitochondria.

A recent study demonstrates the production of large bursts of O_2^-, termed "superoxide flashes", in human mitochondria (58). The flash events occur randomly in space and time, last for 20–30 seconds and are confined to tiny elliptical areas (58). Under the conditions that were tested human MnSOD in mitochondrial matrix was expected to eliminate superoxide flashes in a shorter time scale, considering that the reactivity of human MnSOD was thought to be diffusion controlled (k = 2.3 × 10^9 M^{-1} s^{-1}) and its intramitochondrial concentration is 10–40 μM (52,59). The observation of superoxide flashes indicates that human MnSOD is unable to maintain a steady-state concentration of O_2^- in tiny elliptical areas in mitochondria. The most likely explanation for this phenomenon is that human MnSOD is significantly inhibited at these high concentrations of O_2^-. Under these conditions, bursts of O_2^- are not translated into bursts of H_2O_2 that could result in aberrant oxidant-driven signaling in mitochondria.

Mitochondria are the main source of H_2O_2 and its decomposition in the mitochondrial matrix is catalyzed by glutathione peroxidase and catalase. The rate constants of mammalian glutathione peroxidase and catalase are 5 × 10^7 M^{-1} s^{-1} and 4.6 × 10^7 M^{-1} s^{-1}, respectively, and their intramitochondrial concentration is ~10% that of MnSOD (59). These antioxidants maintain a steady-state intramitochonrial H_2O_2 concentration of ~0.5 × 10^{-8} M (59). As no comparison of H_2O_2 concentration in areas with or without superoxide flashes has been reported, it is unclear whether superoxide flashes cause "H_2O_2 flashes" in tiny confined areas in mitochondria.

In contrast, neither superoxide flashes nor evidence of H_2O_2 signaling in yeast have been reported. The different levels of product inhibition found in human and *Sc*MnSOD may well be explained by the necessity for constrained generation of H_2O_2 in human mitochondria, especially under the conditions associated with "superoxide flashes".

Binding of a Sixth Ligand and the Proposed Mechanism of Yeast MnSODs. Native *Sc*Mn^{3+}SOD and *Ca*Mn^{3+}SODc display optical absorption spectra that are different from other Mn^{3+}SODs. When the yeast enzymes were chemically oxidized, the spectra changed over time from characteristic 5-coordinate Mn^{3+} spectra to spectra with additional absorption intensity around 390 nm. The growth of this absorption intensity can be ascribed to the binding of a sixth ligand, L, leading to formation of an L-Mn^{3+}SOD complex, and since its formation is favored at high pH the sixth ligand is highly likely to be a hydroxide. EPR spectra suggest the presence of at least two Mn^{3+}-containing species with distinct electronic ground states in yeast Mn^{3+}SODs. One of them is the well-characterized 5-coordinate Mn^{3+}SOD, and the other could be an L-Mn^{3+}SOD species with the sixth ligand bound in the equatorial plane.

A 6-coordinate MnSOD that binds two H_2O/OH^- has been obtained in the past at cryogenic conditions or at high pH. The structure of cyro-trapped *Ec*MnSOD crystallized at pH 8.5 shows a H_2O/OH^- bound to the equatorial plane of Mn, giving an octahedral coordination center (60). Probing the Mn^{2+} center of *Ec*MnSOD using high-field EPR indicates transfer of a water molecule to the Mn center at 240–268 K (61). *Ec*Mn^{3+}SOD at pH 11.65 forms a putative 6-coordinate species, giving a heterogeneous EPR spectrum that is comparable to those reported here for *Sc*Mn^{3+}SOD and *Ca*Mn^{3+}SODc at pH 7.65 (31). Recently Porta *et. al.* have reported a 6-coordinate structure of *Ec*MnSOD with peroxide bound as a side-on ligand to active site manganese (62). However, the existence of a 6-coordinate MnSOD binding two H_2O/OH^- that is stable in solution at room temperature and neutral pH is novel.

Examination of the second coordination sphere of *Sc*MnSOD shows two outer-sphere solvent molecules within 6 Å of the Mn center, in addition to the Mn-coordinated water. As discussed by Tabares *et. al.* (61), the sixth ligand is most likely the water that is hydrogen bonded

to Tyr34 and His30 (Figure 3.8). Tyr34 and His30 are highly conserved residues that are part of the proposed hydrogen-bonding network, which pumps protons from protein surface to active site (1,40,45,46). They are also involved in the gating between fast and slow protonation pathways as well as the dissociation of H_2O_2 from the active site (24,48). This water, however, only occupies 50% of the subunits in the structure of *Sc*MnSOD or *Ec*MnSOD and cannot be seen in the structure of human MnSOD or *Ca*MnSODc.

The binding site of O_2^- in the MnSOD active site has been investigated using small anions like fluoride and azide as O_2^- analogues. Azide binds to the sixth ligand site in proximity of Try34 in the plane of His26, His81 and Asp168 at low temperatures.(26) Fluoride also sits close to the same binding site and is likely hydrogen bonded to Tyr34 (63). Therefore, to react with the Mn ion O_2^- is highly likely bound in the sixth ligand site in the vicinity to Tyr34. O_2^- has also been proposed to form hydrogen bonds with Tyr34 and the Mn-coordinated H_2O but does not directly bind Mn (63). In both cases, the outer-sphere water, which has been proposed to become the sixth ligand, is located in the vicinity to the O_2^- binding site.

Scheme 3.3. Proposed Mechanism of the Reaction of Yeast Mn^{2+}SOD with O_2^-

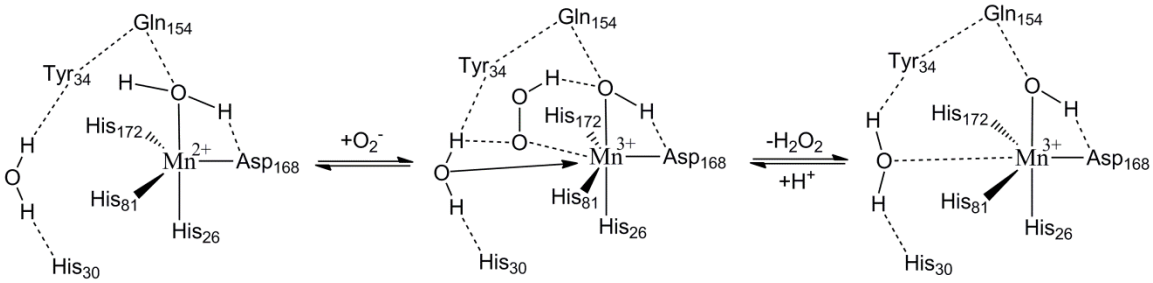

Herein we propose a mechanism based on the tendency of yeast Mn^{3+}SODs to bind two solvent molecules, which may explain their high efficiency at high O_2^- doses (Scheme 3.3).

When O_2^- binds to (or merely approaches) the sixth ligand binding site close to Tyr34, Mn^{2+} transfers an electron to O_2^- (which becomes peroxide) and is oxidized to Mn^{3+}. Since Mn^{3+}SOD tends to bind two solvent molecules, the water molecule that is hydrogen bonded to Tyr34 and His30 may travel to the Mn^{3+} center to compete with the peroxide for the sixth ligand site (Scheme 3.3). This could cause steric effects at the metal binding site, which may destabilize the inner-sphere peroxo-Mn^{3+}SOD complex. This is consistent with the fact that *Sc*MnSOD and *Ca*MnSODc are significantly gated toward the outer-sphere fast protonation pathway, in which formation of the peroxo-Mn^{3+}SOD species is disfavored. The outer-sphere water may not necessarily bind Mn^{3+} ion, which could be a slow process, but merely fluctuate between the Mn center and Tyr34/His30 to create steric effects at the active site. Deviations in the positioning of outer-sphere solvent molecules have been reported to be important in enhancing proton transfer in other metalloenzymes (64). In human carbonic anhydrase II (HACII), the positioning and structuring of water molecules in the active site cavity vary with the conformation of an outer-sphere residue, His64 (64).

The putative translocation of the outer-sphere solvent molecule in yeast MnSODs may also facilitate dissociation of the bound peroxide by enhancing proton transfer. Numerous previous studies show that MnSODs from various organisms exhibit a similar hydrogen isotope effect of ~2, suggesting that proton transfer is involved (65). Dissociation of H_2O_2 from MnSOD active site requires two protons transferred from the protein. Rapid proton transfer from the axial solvent ligand to peroxide is expected to occur in all MnSOD. In yeast MnSODs the other proton is likely donated by the outer-sphere H_2O that sits between Tyr34 and His30 upon translocation, which may highly enhance the proton transfer and facilitate the removal of the peroxide from the active site.

Indeed, the rate of peroxide release from active site (k_4) in *Sc*MnSOD is dramatically depressed at increased pH with a p*K* of ~8, which causes the level of product inhibition to increase (Figure 3.4). This is significantly different from human MnSOD, which maintain a constant k_4 over a wide range of pH (6–10) (65). The depression of k_4, which is likely caused by slower proton transfer, could either be resulted from deprotonation of the axial H_2O or the outer-sphere H_2O that is hydrogen bonded to Tyr34 and His30, or from deprotonation of Tyr34 as proposed to be responsible for the spectroscopic p*K* of *Ec*MnSOD (30). In the latter scenario, deprotonation of Tyr34 may destabilize the potential sixth ligand by eliminating its hydrogen bonding with Tyr34. Considering that the p*K* of k_4 for *Sc*MnSOD is as low as 8 (Figure 3.4) while the p*K* of Tyr34 is 11.5, deprotonation of the solvent ligands is more likely. This may support the hypothesis that the outer-sphere solvent molecule approaches the sixth ligand site of the Mn^{3+} ion and transfers a proton to the peroxide to facilitate its leaving.

However, the binding of two H_2O/OH^- in *Sc*Mn^{3+}SOD and *Ca*Mn^{3+}SODc may not be relevant to their fast catalytic kinetics and low level of product inhibition, but merely a coincidence. We will therefore continue investigating the correlation between product inhibition and the L-Mn^{3+}SOD species by investigating yeast MnSOD mutants with mutations at certain second coordination sphere residues.

In conclusion, MnSODs from *S. cerevisiae* mitochondria and *C. albicans* cytosol both exhibit higher efficiencies of O_2^- dismutation at high [O_2^-] than human and bacterial MnSODs. The unusual resting state of yeast MnSODs could be attributed to the slightly longer distance between Gln154 and Mn. Both yeast Mn^{3+}SODs form a 6-coordinate species. The potential sixth ligand could be an outer-sphere water and its translocation to Mn ion in the catalytic cycle may facilitate the reaction of Mn^{2+}SOD with O_2^- to undergo through the non-inhibited pathway.

Among MnSODs that have been characterized to date, human MnSOD is the only enzyme that significantly undergoes the product-inhibited pathway at high [O_2^-], which can be ascribed to complicated roles of H_2O_2 in mammalian cells, especially as a signaling agent.

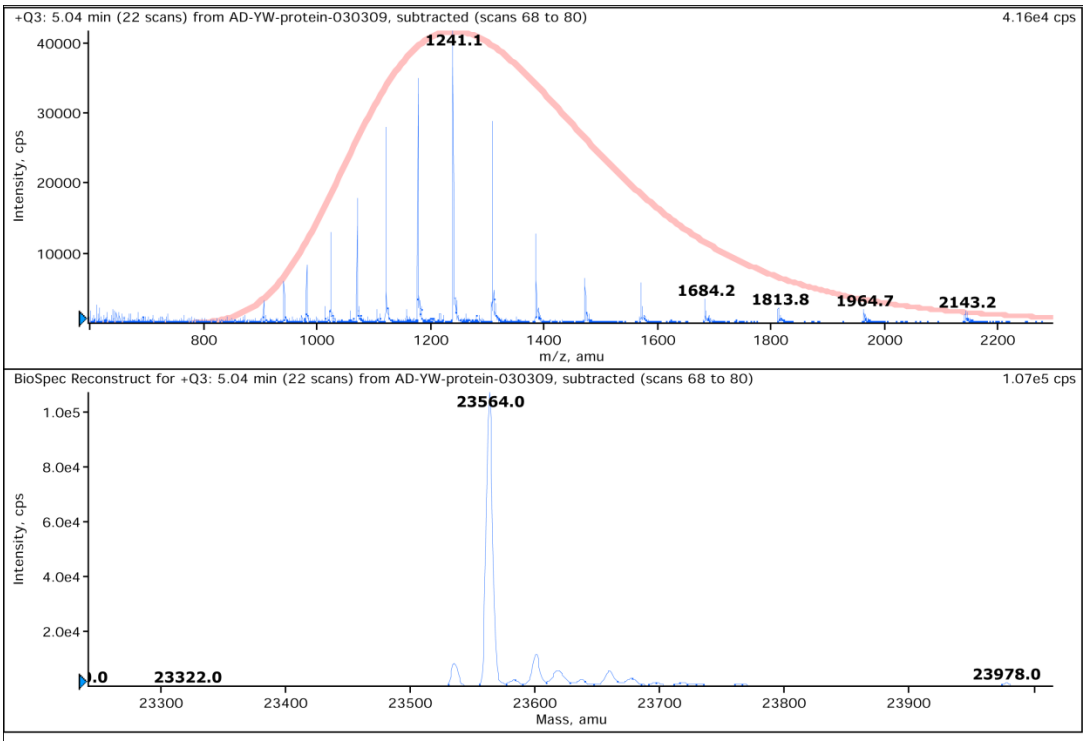

Figure S3.1. Electrospray-ionization mass spectra (top panel) of methylated *Sc*MnSOD and its reconstructed mass distribution profiles (bottom panel). Ordinate units of intensity are arbitrary and the abscissa units of average molecular mass are in Daltons. The expected mass is 23,560 Da.

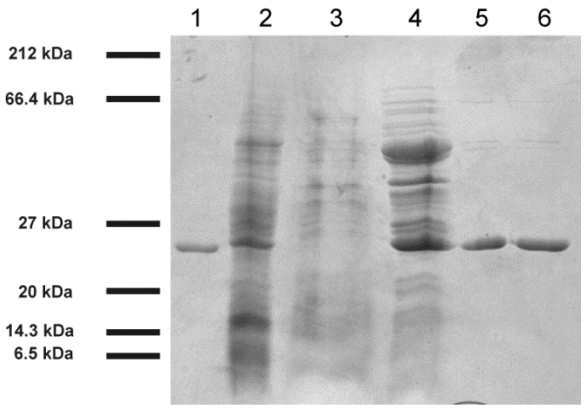

Figure S3.2. The SDS-PAGE analysis of the purification of *Ca*MnSODc: 1) purified *Sc*MnSOD; 2) cell lysate; 3) supernatant of ammonium sulfate cut; 4) active HIC fractions; 5) DE52 load and wash; 6) 5 µg of purified *Ca*MnSODc after G300 column.

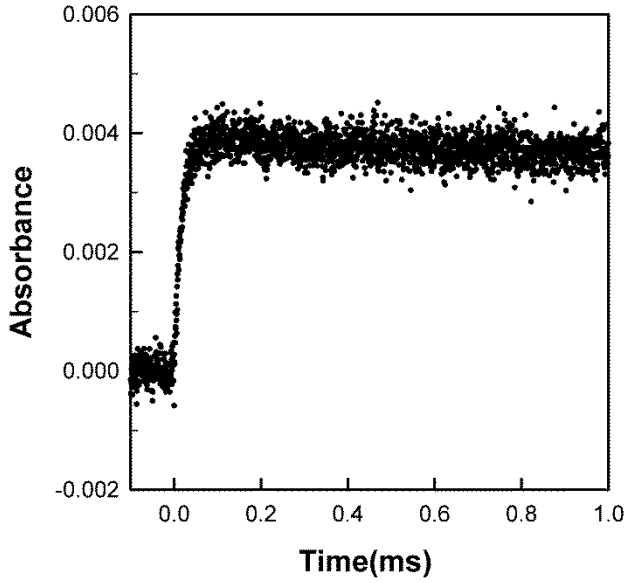

Figure S3.3. Oxidation of *Ca*Mn^{2+}SODc by O_2^- in pulse radiolysis. The formation of Mn^{3+}SOD is indicated by the change of absorbance at 480 nm over time upon generation of 2.2 μM O_2^-. The sample contained 60 μM (in Mn) *Ca*MnSODc, 10 mM potassium phosphate (pH 7), 10 mM sodium formate, and 100 μM EDTA. The enzyme was reduced prior to each pulse with 120 μM H_2O_2.

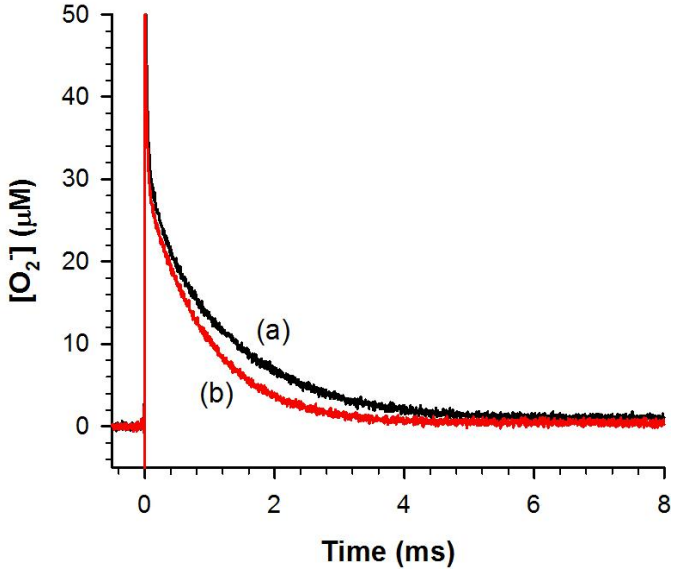

Figure S3.4. Decay of 48 μM O_2^- catalyzed by 1 μM (in Mn) *Ca*MnSODc (a, black) and *Sc*CuZnSOD (b, red). The sample of pulse radiolysis contained 10 mM potassium phosphate (pH 7), 10 mM sodium formate and 10 μM EDTA.

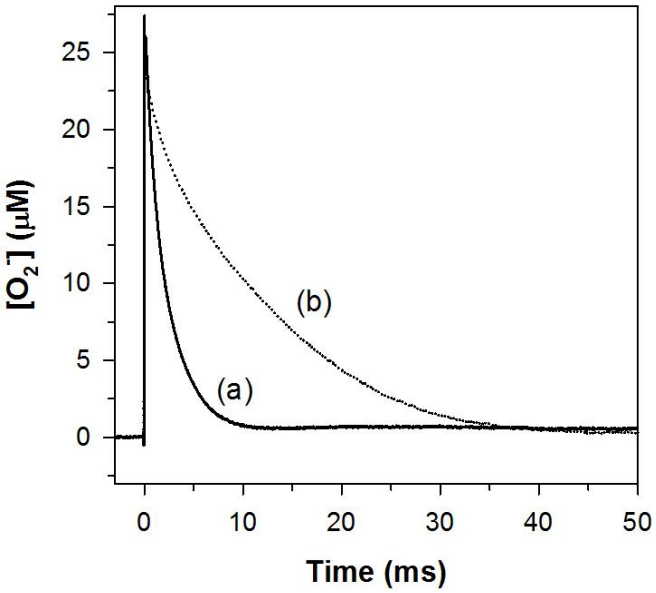

Figure S3.5. Dependence of the level of product inhibition of *Ca*MnSODc on pH. Decay of 25 μM O_2^- catalyzed by 1 μM (in Mn) *Ca*MnSODc at pH 7.5 (a) and 9.0 (b). The sample of pulse radiolysis contained 10 mM potassium phosphate (pH 7), 10 mM sodium formate and 10 μM EDTA.

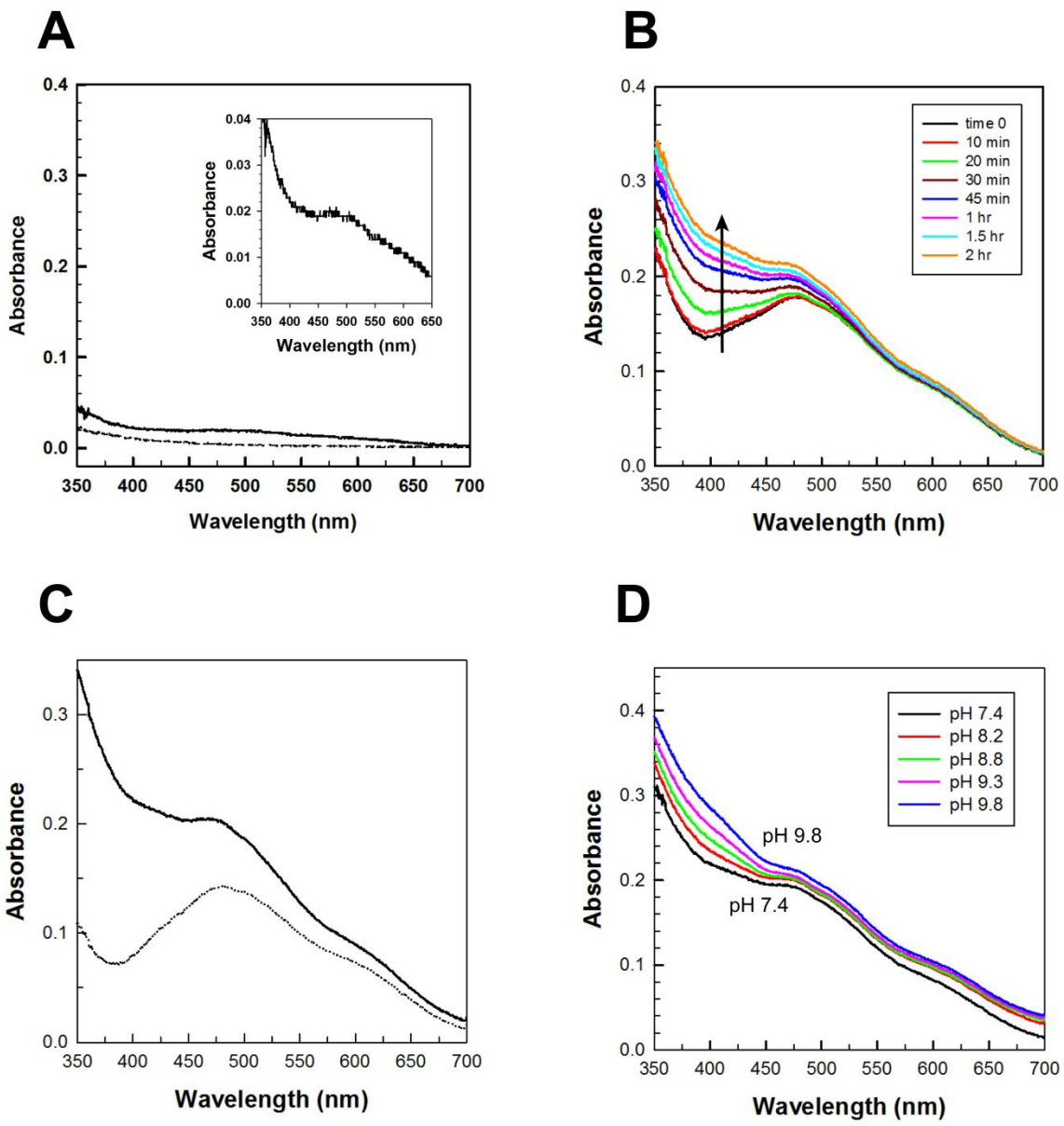

Figure S3.6. The oxidation state of *Ca*MnSODc. (**A**) Optical spectra of as-isolated *Ca*MnSODc (solid line) and *Ca*MnSODc reduced by sodium hydrosulfite (dashed line). Inset: The difference spectrum between as-isolated and reduced *Ca*MnSODc. (**B**) Optical spectra of *Ca*MnSODc oxidized by potassium permanganate ([$KMnO_4$]:MnSOD = 0.75:1) as measured over time. (**C**) Reduction of *Ca*Mn^{3+}SODc (solid line, oxidized by 0.75 equivalent of $KMnO_4$ and allowed to equilibrate at room temperature for 2 hr) by one equivalent of sodium ascorbate (dotted line). (**D**) Optical spectra of *Ca*Mn^{3+}SODc at different pH. The sample solution contained 160 μM (in Mn) enzyme in 25 mM potassium phosphate (pH 7.4).

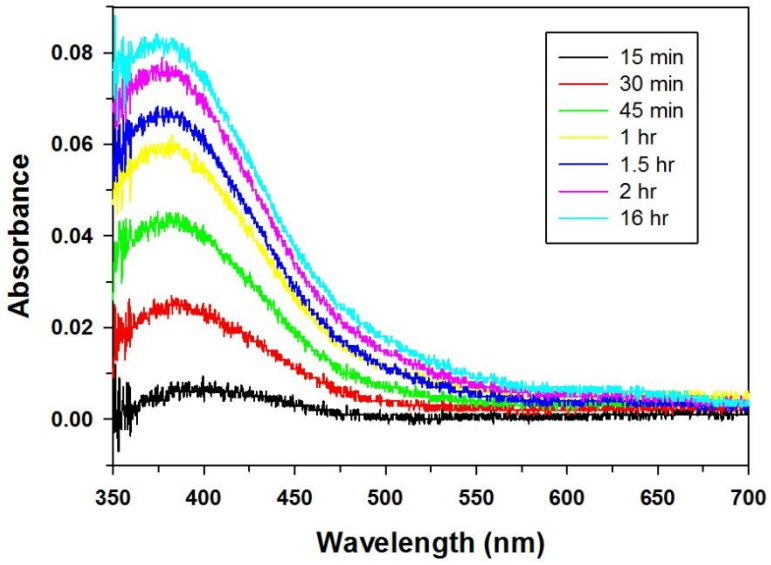

Figure S3.7. The absorption band of *Sc*Mn^{3+}SOD around 390 nm as measured over time. *Sc*MnSOD oxidized by potassium permanganate ([$KMnO_4$]:MnSOD = 0.75:1) at pH 7.4 as measured over time. Time 0 refers to the start of the first scan immediately after mixing $KMnO_4$ with the enzyme.

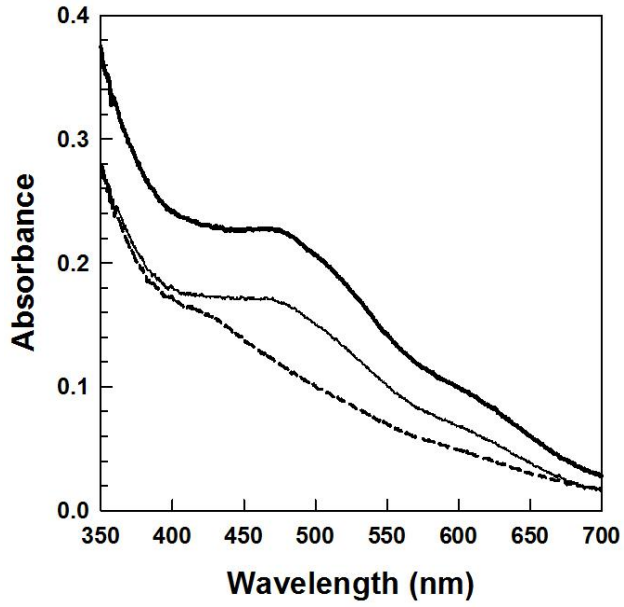

Figure S3.8. Anion binding causes spectral shifts of *Sc*Mn^{3+}SOD. Solutions contained 190 μM (in Mn) *Sc*MnSOD oxidized by 0.75 equivalent of $KMnO_4$ (thick solid, allowed to equilibrate at room temperature for 2 hr) in 25 mM potassium phosphate (pH 7.4) with 100 mM NaF (thin solid) and 100 mM NaN_3 (dashed).

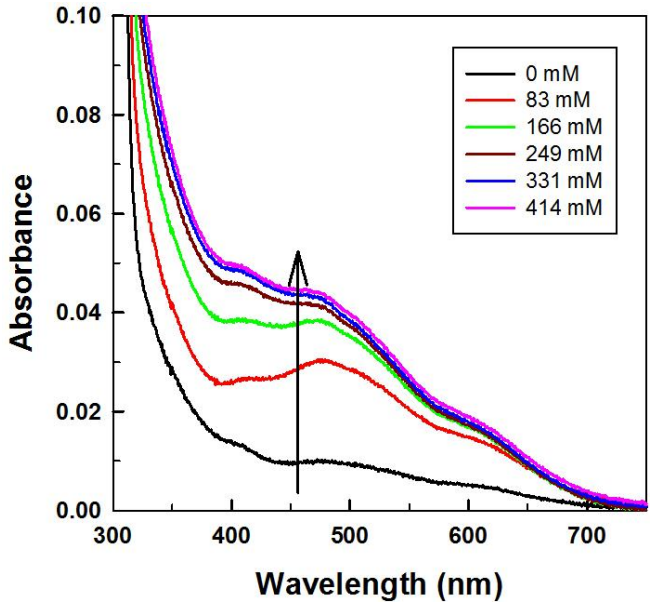

Figure S3.9. Oxidation of as-isolated *Sc*MnSOD by O_2^- at long timescales. O_2^- was generated by ^{60}Co radiation source. The legend shows the doses of O_2^- that reacted with *Sc*MnSOD before spectra were taken. The sample solution contained 130 μM (in Mn) *Sc*MnSOD in 25 mM potassium phosphate (pH 7.4) and 200 units/mL catalase.

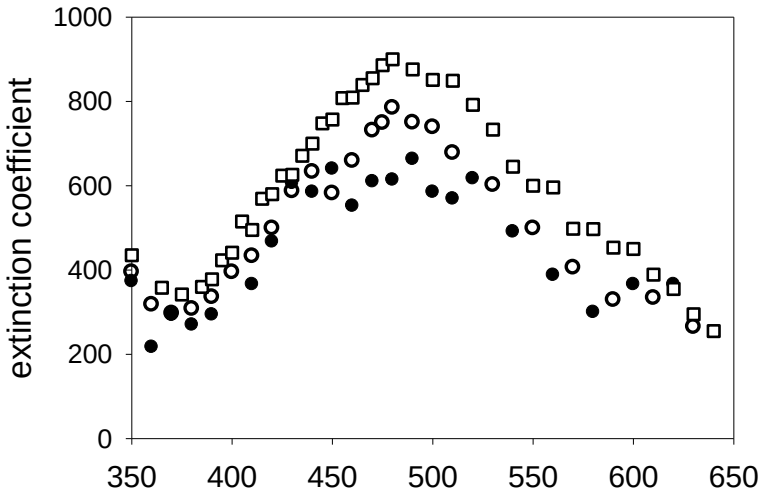

Figure S3.10. The Mn^{3+} spectra of yeast MnSODs at different pH as determined by pulse radiolysis. Protein samples are: 1) 60 μM *Ca*MnSODc at pH 7.5 (squares); 2) 40 μM *Sc*MnSOD at pH 7.0 (open circles); 3) 40 μM *Sc*MnSOD at pH 10.0 (closed circles).

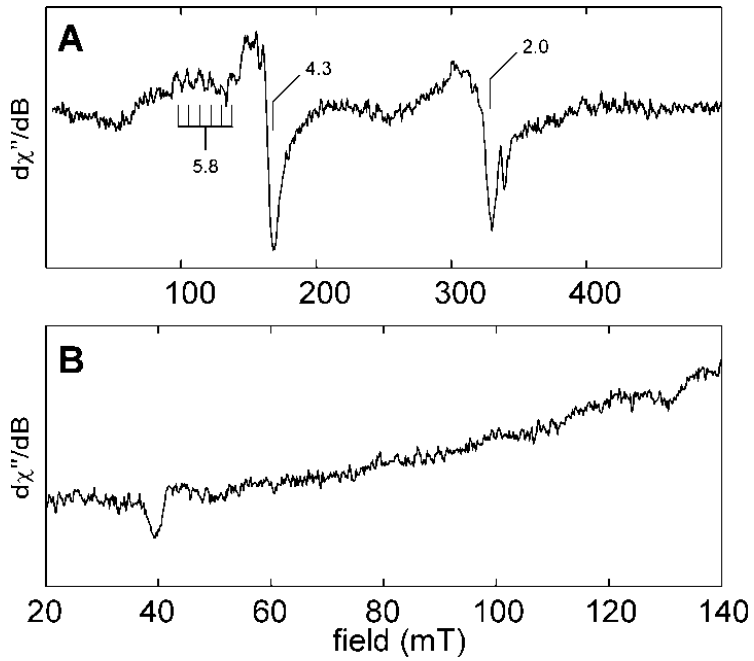

Figure S3.11. These spectra are similar to those obtained for *Ec*Mn^{2+}SOD. Five separate electron spin transitions are possible and these are shifted from $g = 2.0$ due to zero-field splitting of the manifold of spin levels of the high-spin ($S = 5/2$) Mn^{2+} ion. In some cases, these resonances are further split (e.g., the feature at $g = 5.8$) by the hyperfine interaction of the electron spin with the ^{55}Mn nuclear spin ($I = 5/2$).

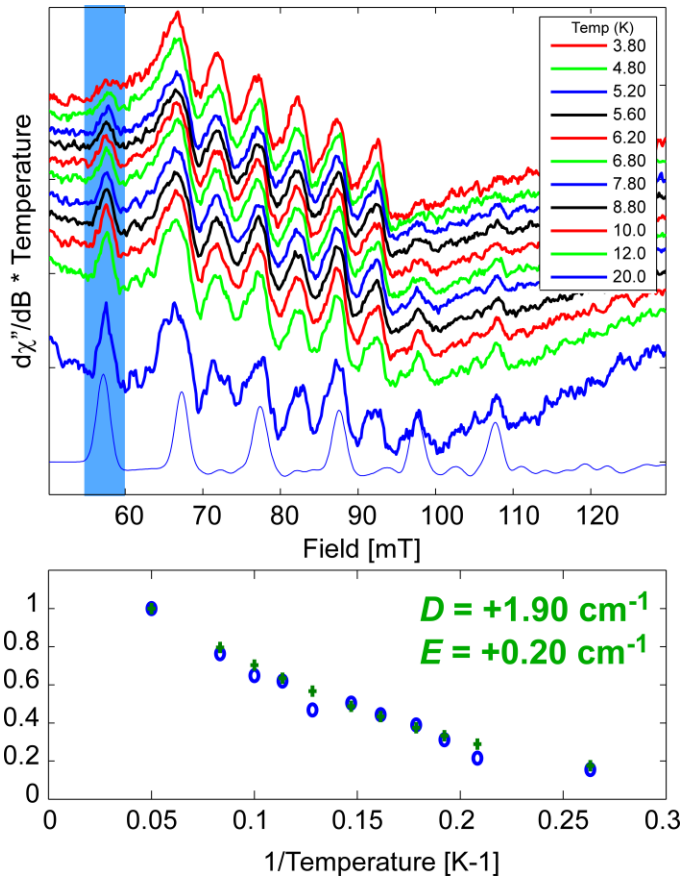

Figure S3.12. (Top panel) Temperature dependence of the parallel-mode EPR spectrum of permanganate-oxidized *Ca*MnSODc. Except for temperature (given in legend), the spectrometer settings are the same as those given in the caption of Figure 3.7. Simulation of the $^5A_{1g}$ component is shown (thin blue line). (Bottom panel) Integrated intensity of feature centered at 58 mT (blue circles) as a function of the inverse of the temperature and corresponding simulated integrated intensity (green crosses) achieved using ZFS parameters D = +1.90 cm^{-1} and E = 0.2 cm^{-1}.

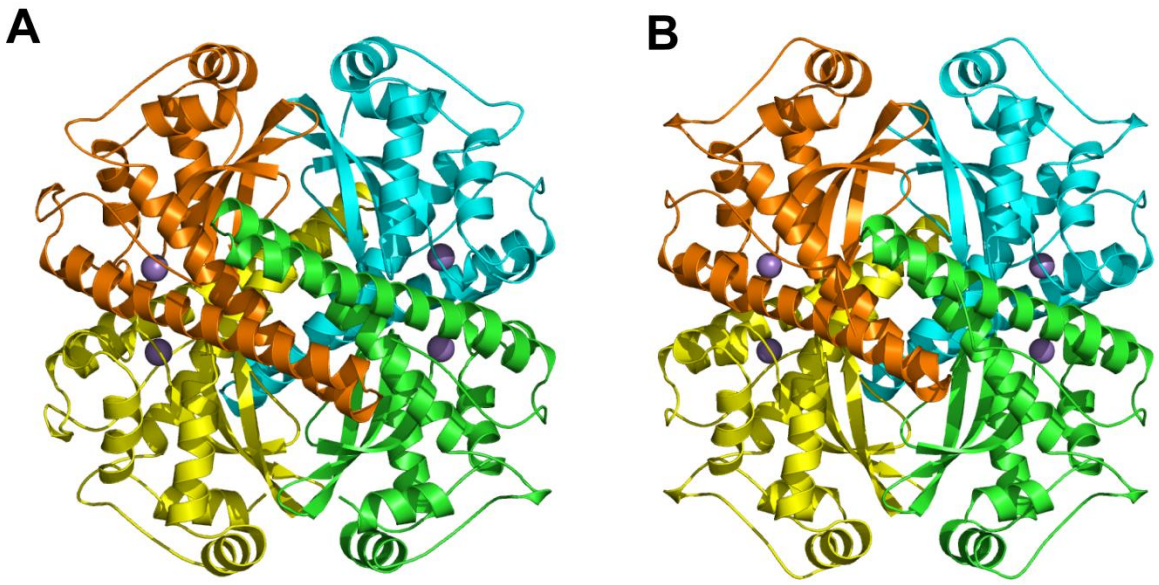

Figure S3.13. The quaternary structure of *Sc*MnSOD (**A**) and *Ca*MnSODc (**B**) in crystal lattice. Crystallization condition for *Ca*MnSODc: 0.1 M magnesium chloride, 0.1 M sodium chloride and 0.1 M tri-sodium citrate (pH 5.5) in 30% (w/v) polyethylene glycol 400 at 4 ℃ with a protein concentration of 7 mg/mL.

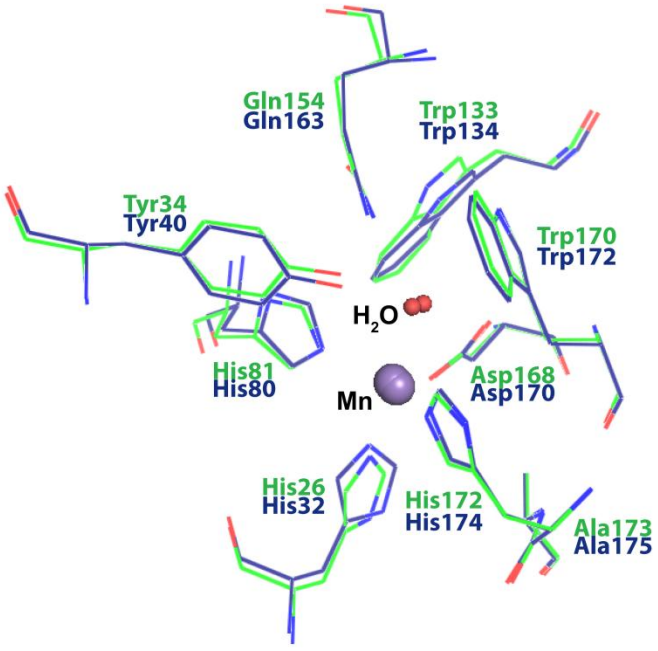

Figure S3.14. Superposition of the active site of *Sc*MnSOD (green, chain A, PDB accession: 3LSU) and *Ca*MnSODc (blue, PDB accession: 3QVN).

Table S3.1. X-ray Data Collection and Refinement Statistics [a].

	***Sc*MnSOD**	***Ca*MnSODc**
Data Collection		
X-Ray Source	Rigaku FRE+	Rigaku FRE+
Detector	Rigaku HTC	Rigaku HTC
Reflections observed	197227	252317
Unique reflections	59997	6933
Wavelength (Å)	1.5418	1.5418
Resolution (Å)	1.90	2.60
Highest Resolution Shell (Å)	1.97-1.90	2.69-2.60
Space group	P1	P $6_4$22
R_{sym} (%) [b]	8.3 (31.4)	17.9 (74.3)
I/σ	14.8 (3.7)	22.9 (8.1)
Completeness (%)	89.5 (53.1)	99.0 (100.0)
Unit cell dimensions		
a (Å)	63.657	77.134
b (Å)	64.933	77.134
c (Å)	66.550	120.080
α (°)	109.36	90.0
β (°)	106.33	90.0
γ (°)	109.68	120.0
Wilson B value ($Å^2$)	24.3	52.8
Refinement		
Resolution (Å)	32.0 – 1.9	44.6 – 2.6
Reflections Used	59979	6626
R_{work}(%)	16.30 (16.50)	20.25 (27.42)
R_{free} (%) [c]	19.50 (19.20)	26.86 (40.48)
Protein Molecules in Asymmetric Unit	4	1
Number of non-H atoms		
Protein	6661	1593
Non-protein	450	23
RMS deviations		
Bond lengths (Å)	0.007	0.002
Bond angles (°)	1.045	0.517
Average B-factor ($Å^2$)		
Protein atoms	24.52	52.85
Non-protein atoms	29.50	40.75
PDB accession code	3LSU	3QVN

a. Highest resolution shell shown in parenthesis.
b. $R_{sym} = \Sigma \mid I-\langle I\rangle \mid / \Sigma I$
c. R_{free} calculated using 5% of the data

Table S3.2. Active Site Crystallographic Distances

	*Sc*MnSOD (pdb: 3lsu)	*Ca*MnSODc (pdb: 3qvn)	Human (pdb: 1n0j)	*A. fumigatus* (pdb: 1kkc)	*C. elegans* (pdb: 3dc5)	*E. coli* (pdb: 1vew)	*T. Thermophilus* (pdb: 3mds)	*Drad* (pdb: 2ce4)
Ligands								
Mn-NE2 (His26)[a]	2.24 (0.05)	2.35	2.10 (0.01)	2.11 (0.09)	2.23 (0.01)	2.14 (0.04)	2.14 (0)	2.19 (0.05)
Mn-NE2 (His81)	2.22 (0.02)	2.27	2.10 (0.02)	2.19 (0.06)	2.19 (0.01)	2.21 (0.01)	2.10 (0.02)	2.10 (0.09)
Mn-NE2 (His172)	2.22 (0.02)	2.26	2.09 (0)	2.20 (0.08)	2.18 (0.07)	2.17 (0.01)	2.17 (0.02)	2.16 (0.08)
Mn-OD2 (Asp168)	2.05 (0.02)	2.11	1.94 (0)	1.99 (0.04)	2.06 (0.01)	2.02 (0.01)	1.79 (0.01)	1.93 (0.04)
Mn-O (coord solvent)	2.31 (0.04)	2.33	2.02 (0.01)	2.27 (0.06)	2.26 (0.01)	2.21 (0.05)	2.08 (0.01)	2.19 (0.01)
Coordinating Solvent Molecule								
O-OD2 (Asp168)	2.89 (0.03)	3.08	2.95 (0.06)	2.89 (0.11)	2.78 (0)	2.78 (0.04)	2.78 (0.06)	2.83 (0.01)
O-ND (Gln154)	2.95 (0.02)	2.92	2.95 (0.01)	2.78 (0.13)	2.86 (0.01)	2.90 (0.08)	2.99 (0.03)	2.87 (0.06)

a. Numbering in *Sc*MnSOD is use

References

1. Abreu, I. A., and Cabelli, D. E. (2010) Superoxide dismutases-a review of the metal-associated mechanistic variations. *Biochim Biophys Acta* **1804**, 263-274

2. Zheng, J., Domsic, J. F., Cabelli, D., McKenna, R., and Silverman, D. N. (2007) Structural and kinetic study of differences between human and Escherichia coli manganese superoxide dismutases. *Biochemistry* **46**, 14830-14837

3. Abreu, I. A., Hearn, A., An, H., Nick, H. S., Silverman, D. N., and Cabelli, D. E. (2008) The kinetic mechanism of manganese-containing superoxide dismutase from Deinococcus radiodurans: a specialized enzyme for the elimination of high superoxide concentrations. *Biochemistry* **47**, 2350-2356

4. Barnese, K., Sheng, Y., Stich, T. A., Gralla, E. B., Britt, R. D., Cabelli, D. E., and Valentine, J. S. (2010) Investigation of the highly active manganese superoxide dismutase from Saccharomyces cerevisiae. *J Am Chem Soc* **132**, 12525-12527

5. Valko, M., Rhodes, C. J., Moncol, J., Izakovic, M., and Mazur, M. (2006) Free radicals, metals and antioxidants in oxidative stress-induced cancer. *Chem Biol Interact* **160**, 1-40

6. Giorgio, M., Trinei, M., Migliaccio, E., and Pelicci, P. G. (2007) Hydrogen peroxide: a metabolic by-product or a common mediator of ageing signals? *Nat Rev Mol Cell Biol* **8**, 722-728

7. Veal, E. A., Day, A. M., and Morgan, B. A. (2007) Hydrogen peroxide sensing and signaling. *Mol Cell* **26**, 1-14

8. Stone, J. R., and Yang, S. (2006) Hydrogen peroxide: a signaling messenger. *Antioxid Redox Signal* **8**, 243-270

9. Rhee, S. G. (2006) Cell signaling. H2O2, a necessary evil for cell signaling. *Science* **312**, 1882-1883

10. Finkel, T., and Holbrook, N. J. (2000) Oxidants, oxidative stress and the biology of ageing. *Nature* **408**, 239-247

11. Finkel, T. (2003) Oxidant signals and oxidative stress. *Curr Opin Cell Biol* **15**, 247-254

12. Jackson, T. A., and Brunold, T. C. (2004) Combined spectroscopic/computational studies on Fe- and Mn-dependent superoxide dismutases: insights into second-sphere tuning of active site properties. *Acc Chem Res* **37**, 461-470

13. Lamarre, C., LeMay, J. D., Deslauriers, N., and Bourbonnais, Y. (2001) Candida albicans expresses an unusual cytoplasmic manganese-containing superoxide dismutase (SOD3 gene product) upon the entry and during the stationary phase. *J Biol Chem* **276**, 43784-43791

14. Schwarz, H., BNL Pulse Radiolysis Program. Brookhaven National Laboratory

15. Stoll, S., and Britt, R. D. (2009) General and efficient simulation of pulse EPR spectra. *Phys Chem Chem Phys* **11**, 6614-6625

16. Stoll, S., and Schweiger, A. (2006) EasySpin, a comprehensive software package for spectral simulation and analysis in EPR. *J Magn Reson* **178**, 42-55

17. Walter, T. S., Meier, C., Assenberg, R., Au, K. F., Ren, J. S., Verma, A., Nettleship, J. E., Owens, R. J., Stuart, D. I., and Grimes, J. M. (2006) Lysine methylation as a routine rescue strategy for protein crystallization. *Structure* **14**, 1617-1622

18. Sutherland, M. W., and Learmonth, B. A. (1997) The tetrazolium dyes MTS and XTT provide new quantitative assays for superoxide and superoxide dismutase. *Free Radic Res* **27**, 283-289

19. Otwinowski, Z., and Minor, W. (1997) Processing of X-ray diffraction data collected in oscillation mode. *Method Enzymol* **276**, 307-326

20. Mccoy, A. J., Grosse-Kunstleve, R. W., Adams, P. D., Winn, M. D., Storoni, L. C., and Read, R. J. (2007) Phaser crystallographic software. *J Appl Crystallogr* **40**, 658-674

21. Emsley, P., and Cowtan, K. (2004) Coot: model-building tools for molecular graphics. *Acta Crystallogr D* **60**, 2126-2132

22. Murshudov, G. N., Vagin, A. A., and Dodson, E. J. (1997) Refinement of macromolecular structures by the maximum-likelihood method. *Acta Crystallogr D* **53**, 240-255

23. Adams, P. D., Grosse-Kunstleve, R. W., Hung, L. W., Ioerger, T. R., McCoy, A. J., Moriarty, N. W., Read, R. J., Sacchettini, J. C., Sauter, N. K., and Terwilliger, T. C. (2002) PHENIX: building new software for automated crystallographic structure determination. *Acta Crystallogr D Biol Crystallogr* **58**, 1948-1954

24. Perry, J. J., Hearn, A. S., Cabelli, D. E., Nick, H. S., Tainer, J. A., and Silverman, D. N. (2009) Contribution of human manganese superoxide dismutase tyrosine 34 to structure and catalysis. *Biochemistry* **48**, 3417-3424

25. Ravindranath, S. D., and Fridovich, I. (1975) Isolation and characterization of a manganese-containing superoxide dismutase from yeast. *J Biol Chem* **250**, 6107-6112

26. Whittaker, M. M., and Whittaker, J. W. (1996) Low-temperature thermochromism marks a change in coordination for the metal ion in manganese superoxide dismutase. *Biochemistry* **35**, 6762-6770

27. Vance, C. K., and Miller, A. F. (2001) Novel insights into the basis for Escherichia coli superoxide dismutase's metal ion specificity from Mn-substituted FeSOD and its very high E(m). *Biochemistry* **40**, 13079-13087

28. Leveque, V. J., Vance, C. K., Nick, H. S., and Silverman, D. N. (2001) Redox properties of human manganese superoxide dismutase and active-site mutants. *Biochemistry* **40**, 10586-10591

29. Whittaker, J. W., and Whittaker, M. M. (1991) Active-Site Spectral Studies on Manganese Superoxide-Dismutase. *J Am Chem Soc* **113**, 5528-5540

30. Maliekal, J., Karapetian, A., Vance, C., Yikilmaz, E., Wu, Q., Jackson, T., Brunold, T. C., Spiro, T. G., and Miller, A. F. (2002) Comparison and contrasts between the active site PKs of Mn-superoxide dismutase and those of Fe-superoxide dismutase. *J Am Chem Soc* **124**, 15064-15075

31. Campbell, K. A. (1999) CW and Pulsed EPR Studies of Photosystem II and Mn-Containing Complexes. University of California, Davis. Ph.D

32. Jackson, T. A., Karapetian, A., Miller, A. F., and Brunold, T. C. (2005) Probing the geometric and electronic structures of the low-temperature azide adduct and the product-inhibited form of oxidized manganese superoxide dismutase. *Biochemistry* **44**, 1504-1520

33. Campbell, K. A., Force, D. A., Nixon, P. J., Dole, F., Diner, B. A., and Britt, R. D. (2000) Dual-mode EPR detects the initial intermediate in photoassembly of the photosystem II mn cluster: The influence of amino acid residue 170 of the D1 polypeptide on Mn coordination. *J Am Chem Soc* **122**, 3754-3761

34. Edwards, R. A., Baker, H. M., Whittaker, M. M., Whittaker, J. W., Jameson, G. B., and Baker, E. N. (1998) Crystal structure of Escherichia coli manganese superoxide dismutase at 2.1-angstrom resolution. *J Biol Inorg Chem* **3**, 161-171

35. Krivokapic, I., Noble, C., Klitgaard, S., Tregenna-Piggott, P., Weihe, H., and Barra, A. L. (2005) Anisotropic hyperfine interaction in the manganese(III) hexaaqua ion. *Angew Chem Int Ed Engl* **44**, 3613-3616

36. Campbell, K. A., Lashley, M. R., Wyatt, J. K., Nantz, M. H., and Britt, R. D. (2001) Dual-mode EPR study of Mn(III) salen and the Mn(III) salen-catalyzed epoxidation of cis-beta-methylstyrene. *J Am Chem Soc* **123**, 5710-5719

37. Borgstahl, G. E., Parge, H. E., Hickey, M. J., Beyer, W. F., Jr., Hallewell, R. A., and Tainer, J. A. (1992) The structure of human mitochondrial manganese superoxide dismutase reveals a novel tetrameric interface of two 4-helix bundles. *Cell* **71**, 107-118

38. Fluckiger, S., Mittl, P. R., Scapozza, L., Fijten, H., Folkers, G., Grutter, M. G., Blaser, K., and Crameri, R. (2002) Comparison of the crystal structures of the human manganese superoxide dismutase and the homologous Aspergillus fumigatus allergen at 2-A resolution. *J Immunol* **168**, 1267-1272

39. Trinh, C. H., Hunter, T., Stewart, E. E., Phillips, S. E., and Hunter, G. J. (2008) Purification, crystallization and X-ray structures of the two manganese superoxide dismutases from Caenorhabditis elegans. *Acta Crystallogr Sect F Struct Biol Cryst Commun* **64**, 1110-1114

40. Perry, J. J., Shin, D. S., Getzoff, E. D., and Tainer, J. A. (2010) The structural biochemistry of the superoxide dismutases. *Biochim Biophys Acta* **1804**, 245-262

41. Jackson, T. A., Xie, J., Yikilmaz, E., Miller, A. F., and Brunold, T. C. (2002) Spectroscopic and computational studies on iron and manganese superoxide dismutases: nature of the chemical events associated with active-site pKs. *J Am Chem Soc* **124**, 10833-10845

42. Carugo, O., and Djinovic Carugo, K. (2005) When X-rays modify the protein structure: radiation damage at work. *Trends Biochem Sci* **30**, 213-219

43. Hsieh, Y. S., Guan, Y., Tu, C. K., Bratt, P. J., Angerhofer, A., Lepock, J. R., Hickey, M. J., Tainer, J. A., Nick, H. S., and Silverman, D. N. (1998) Probing the active site of human manganese superoxide dismutase: The role of glutamine 143. *Biochemistry* **37**, 4731-4739

44. Leveque, V. J., Stroupe, M. E., Lepock, J. R., Cabelli, D. E., Tainer, J. A., Nick, H. S., and Silverman, D. N. (2000) Multiple replacements of glutamine 143 in human manganese superoxide dismutase: effects on structure, stability, and catalysis. *Biochemistry* **39**, 7131-7137

45. Whittaker, M. M., and Whittaker, J. W. (1997) Mutagenesis of a proton linkage pathway in Escherichia coli manganese superoxide dismutase. *Biochemistry* **36**, 8923-8931

46. Edwards, R. A., Whittaker, M. M., Whittaker, J. W., Baker, E. N., and Jameson, G. B. (2001) Outer sphere mutations perturb metal reactivity in manganese superoxide dismutase. *Biochemistry* **40**, 15-27

47. Guan, Y., Hickey, M. J., Borgstahl, G. E., Hallewell, R. A., Lepock, J. R., O'Connor, D., Hsieh, Y., Nick, H. S., Silverman, D. N., and Tainer, J. A. (1998) Crystal structure of Y34F mutant human mitochondrial manganese superoxide dismutase and the functional role of tyrosine 34. *Biochemistry* **37**, 4722-4730

48. Davis, C. A., Hearn, A. S., Fletcher, B., Bickford, J., Garcia, J. E., Leveque, V., Melendez, J. A., Silverman, D. N., Zucali, J., Agarwal, A., and Nick, H. S. (2004) Potent anti-tumor effects of an active site mutant of human manganese-superoxide dismutase. Evolutionary conservation of product inhibition. *J Biol Chem* **279**, 12769-12776

49. Yikilmaz, E., Porta, J., Grove, L. E., Vahedi-Faridi, A., Bronshteyn, Y., Brunold, T. C., Borgstahl, G. E. O., and Miller, A. F. (2007) How can a single second sphere amino acid substitution cause reduction midpoint potential changes of hundreds of millivolts? *J Am Chem Soc* **129**, 9927-9940

50. Yikilmaz, E., Xie, J., Brunold, T. C., and Miller, A. F. (2002) Hydrogen-bond-mediated tuning of the redox potential of the non-heme Fe site of superoxide dismutase. *J Am Chem Soc* **124**, 3482-3483

51. Miller, A. F., and Vance, C. K. (2001) Novel insights into the basis for Escherichia coli superoxide dismutase's metal ion specificity from Mn-substituted FeSOD and its very high E(m). *Biochemistry* **40**, 13079-13087

52. Cadenas, E. (2004) Mitochondrial free radical production and cell signaling. *Mol Aspects Med* **25**, 17-26

53. Droge, W. (2002) Free radicals in the physiological control of cell function. *Physiol Rev* **82**, 47-95

54. Mahadev, K., Wu, X., Zilbering, A., Zhu, L., Lawrence, J. T., and Goldstein, B. J. (2001) Hydrogen peroxide generated during cellular insulin stimulation is integral to activation of the distal insulin signaling cascade in 3T3-L1 adipocytes. *J Biol Chem* **276**, 48662-48669

55. Tonks, N. K. (2005) Redox redux: revisiting PTPs and the control of cell signaling. *Cell* **121**, 667-670

56. Melendez, J. A., Dasgupta, J., Subbaram, S., Connor, K. M., Rodriguez, A. M., Tirosh, O., Beckman, J. S., and JourD'Heuil, D. (2006) Manganese superoxide dismutase protects from TNF-alpha-induced apoptosis by increasing the steady-state production of H2O2. *Antioxid Redox Sign* **8**, 1295-1305

57. Chen, K., Thomas, S. R., Albano, A., Murphy, M. P., and Keaney, J. F., Jr. (2004) Mitochondrial function is required for hydrogen peroxide-induced growth factor receptor transactivation and downstream signaling. *J Biol Chem* **279**, 35079-35086

58. Wang, W., Fang, H., Groom, L., Cheng, A., Zhang, W., Liu, J., Wang, X., Li, K., Han, P., Zheng, M., Yin, J., Mattson, M. P., Kao, J. P., Lakatta, E. G., Sheu, S. S., Ouyang, K., Chen, J., Dirksen, R. T., and Cheng, H. (2008) Superoxide flashes in single mitochondria. *Cell* **134**, 279-290

59. Cadenas, E., and Davies, K. J. (2000) Mitochondrial free radical generation, oxidative stress, and aging. *Free Radic Biol Med* **29**, 222-230

60. Borgstahl, G. E. O., Pokross, M., Chehab, R., Sekher, A., and Snell, E. H. (2000) Cryo-trapping the six-coordinate, distorted-octahedral active site of manganese superoxide dismutase. *Journal of Molecular Biology* **296**, 951-959

61. Tabares, L. C., Cortez, N., Agalidis, I., and Un, S. (2005) Temperature-dependent coordination in E-coli manganese superoxide dismutase. *J Am Chem Soc* **127**, 6039-6047

62. Porta, J., Vahedi-Faridi, A., and Borgstahl, G. E. (2010) Structural analysis of peroxide-soaked MnSOD crystals reveals side-on binding of peroxide to active-site manganese. *J Mol Biol* **399**, 377-384

63. Tabares, L. C., Cortez, N., Hiraoka, B. Y., Yamakura, F., and Un, S. (2006) Effects of substrate analogues and pH on manganese superoxide dismutases. *Biochemistry* **45**, 1919-1929

64. Merz, K. M., Toba, S., and Colombo, G. (1999) Solvent dynamics and mechanism of proton transfer in human carbonic anhydrase II. *J Am Chem Soc* **121**, 2290-2302

65. Hearn, A. S., Stroupe, M. E., Cabelli, D. E., Lepock, J. R., Tainer, J. A., Nick, H. S., and Silverman, D. N. (2001) Kinetic analysis of product inhibition in human manganese superoxide dismutase. *Biochemistry* **40**, 12051-12058

Chapter 4

Six-coordinate Manganese(3+)

in Catalysis by Yeast Manganese Superoxide Dismutase

(This chapter was submitted to *Proceedings of the National Academy of Sciences*)

Introduction

Superoxide dismutase (SOD) with manganese at its active site (MnSOD) is remarkable in that it becomes less efficient when levels of its substrate O_2^- are high, while other subclasses of SOD catalyze the disproportionation of O_2^- at virtually diffusion-controlled rates independent of O_2^- level (1). The degree of depression of MnSOD activity at high [O_2^-] is most prominent in human MnSOD, while the MnSODs from bacteria (*Escherichia coli* (2) and *Deinococcus radiodurans* (3)) and yeast (*Saccharomyces cerevisiae* (4,5) and *Candida albicans* (5)) are relatively more efficient under the same conditions. This unique property of human MnSOD could result from the need for stringent regulation of H_2O_2 production, due to the complicated roles of H_2O_2 in mammalian cells, especially as a signaling agent (5).

Scheme 4.1. Catalytic mechanism of MnSOD

$$Mn^{3+}SOD + O_2^- \xrightarrow{k_1} Mn^{2+}SOD + O_2 \qquad (1)$$

$$Mn^{2+}SOD + O_2^- \xrightarrow{k_2, 2H^+} Mn^{3+}SOD + H_2O_2 \qquad (2)$$

$$Mn^{2+}SOD + O_2^- \xrightarrow{k_3} Mn^{3+}(OO^{2-})SOD \qquad (3)$$

$$Mn^{3+}(OO^{2-})SOD \xrightarrow{k_4, 2H^+} Mn^{3+}SOD + H_2O_2 \qquad (4)$$

The mechanism by which MnSOD removes O_2^- involves product inhibition.(1) Specifically, reduction of O_2^- by Mn^{2+}SOD (Scheme 4.1) occurs either through a pathway (called "prompt protonation" pathway here) (reaction 2), where protonation and dissociation of the peroxo moiety is instantaneous, or through an "inner-sphere" pathway (reaction 3), where a detectable intermediate is formed, which has been suggested to be a side-on Mn(III)-peroxo species (6). (We here refer to this intermediate as a Mn-peroxo complex instead of as a "product-

inhibited" complex, the latter term having been used frequently in previous reports.) When protonation of the Mn-peroxo complex (reaction 4) is rate limiting, the "inner-sphere" pathway has the effect of slowing down MnSOD catalysis.

Recently we have been investigating MnSODs from single-cellular eukaryotes in order to understand the mechanism of product inhibition. Our recent study showed that the two yeast MnSODs, one from *S. cerevisiae* mitochondria (*Sc*MnSOD) and the other from *C. albicans* cytosol (*Ca*MnSODc), are both very efficient at high levels of O_2^-, relative to other MnSODs that have been characterized to date (4,5). Spectroscopic analysis of the oxidized yeast enzymes suggests the presence of a six-coordinate Mn^{3+} species, in addition to the well-characterized five-coordinate Mn^{3+} (5). The sixth ligand is likely a hydroxide. Based on these findings, we earlier proposed, for the fast catalysis by yeast MnSODs, a mechanism that involves putative translocation of an outer-sphere solvent molecule (5). More recently we have been pursuing this mechanistic investigation by focusing on mutant yeast MnSOD with substitutions in the second coordination sphere.

Tyr34 is highly conserved and structurally similar in all known MnSODs, where it participates in a hydrogen-bonding network at the active site. Computational studies suggest that Tyr34 provides one of the two protons needed to form H_2O_2 in the catalytic cycle (7). Deprotonation of Tyr34 is responsible for the spectroscopic changes, including the blue shift and decrease in intensity of the optical absorption maximum, that occurs for Mn^{3+}SOD with increasing pH (8). Wild-type human MnSOD and its Y34F mutant protein have similar k_{cat}/K_m, but k_{cat} is decreased by ~10 fold in the mutant protein (9). SOD activity, measured by the xanthine oxidase/cytochrome c assay, is only slightly reduced in *E. coli* Y34 mutant proteins

(10,11). Tyr34 also plays an interesting role in the "prompt protonation" pathway, as elucidated by the changes in the kinetics of Tyr34 mutant human MnSOD (12).

To test our previously proposed mechanism and to address questions regarding the role of Tyr34 in yeast MnSOD, we purified and characterized Y34F mutant *Sc*MnSOD. To our surprise, we have found that catalysis by Y34F *Sc*MnSOD is completely "inner-sphere". More interestingly, our results reveal that Y34F *Sc*MnSOD has a novel mechanism involving an active six-coordinate Mn^{3+} species and gating between multiple proton transfer pathways, different from any previously characterized wild-type or mutant enzyme.

Materials and Methods

DNA Manipulation of Y34F ScMnSOD and Transformation into S. cerevisiae. Site-directed mutagenesis was carried out on an overexpression vector (YEp352-*Sc*MnSOD) containing the *URA*3 selectable marker and a 2-kb genomic *BamH*I fragment containing the gene for *Sc*MnSOD. The primers 5'-GCACCATCAAACTT**T**TGTGAACGGATTCAACAC-3' and 5'-TGAATCCGTTC-ACA**A**AAGTTTGATGGTGCTTGG-3' were used to create the wild-type cDNA. The PCR products were transformed into *E. coli* DH5α strain and screened by ampicillin selection. The purified vector was transformed into *S. cerevisiae sod*2Δ strain (EG110; *Mat-alpha, ura3, leu2, trp1, his3, sod2::TRP1*).

Expression and Purification of Y34F ScMnSOD. Y34F *Sc*MnSOD was expressed and purified as described (5).

Pulse Radiolysis. The experiments were carried out using the 2 MeV Van de Graaff accelerator at Brookhaven National Laboratory. O_2^- is generated in air-saturated aqueous solution

containing sodium formate through the following reactions: $^{\bullet}OH + HCO_2^- \rightarrow H_2O + CO_2^{\bullet-}$, $O_2 + CO_2^{\bullet-} \rightarrow O_2^{\bullet-} + CO_2$, $e_{aq}^- + O_2 \rightarrow O_2^{\bullet-}$, $H^{\bullet} + O_2 \rightarrow HO_2^{\bullet}$.

The experiments to measure catalytic rates were carried out using two methodologies. One set of studies involved either oxidizing the resting enzyme or reducing the oxidized enzyme with substoichiometric quantities of O_2^- and following the appearance or disappearance of Mn^{3+}SOD, respectively, via following absorbance change in the visible range (370-550 nm). The other method involved following the decay of various [O_2^-] at 260 nm using a 1:1 to 1:50 ratio of [MnSOD]:[O_2^-]. Here, rate constants were calculated by fitting the data obtained to a mechanism described in Scheme 4.1 using the Chemical Kinetics program in PRWIN (13).

All MnSOD concentrations were taken as the ICP-measured concentration of manganese in the sample. The pH of the buffer was adjusted using ultrapure (Baker Ultrex) sodium hydroxide and sulphuric acid.

Crystallization of Y34F ScMnSOD. Fully metallated Y34F *Sc*MnSOD was obtained as described before (5). The reductive methylation of lysine residues of Y34F *Sc*MnSOD was carried out as described, in order to improve the diffraction of protein crystals (14). The activity of native and methylated Y34F *Sc*MnSOD is similar in SOD activity assay (15). All free amino groups of the lysine residues and the N-terminal were methylated as confirmed by mass spectrometry (Figure S1).

Methylated Y34F *Sc*MnSOD was crystallized by hanging-drop vapor diffusion at 4 ℃ against a well solution of 0.2 M sodium malonate (pH 7) in 20% (w/v) polyethylene glycol 3,350 with a protein concentration of 7 mg/mL. Y34F *Sc*MnSOD crystals were cryo-protected in mother liquor solution containing 30% glycerol and flash frozen in liquid nitrogen prior to data collection.

Crystallography: Data Collection and Refinement. All data was collected at 100K at the Synchrotron facility, using a APS BEAMLINE 24-ID-C generator and a ADSC QUANTUM 315 detector. All data was processed using DENZO and SCALEPACK (16). Y34F *Sc*MnSOD was phased by molecular replacement using wild-type *Sc*MnSOD (PDB code: 3LSU). All the molecular replacement was done using PHASER (17). The models were built using COOT (18). All model refinement was done using REFMAC (19) and PHENIX (20). Coordinates and structure factors have been deposited in the PDB with accession number 4E4E for the Y34F *Sc*MnSOD structure.

Results

An Additional Water Sits in the Active Site of Y34F ScMnSOD. To aid in our investigation of the role of Tyr34, we determined the X-ray structure of Y34F *Sc*MnSOD (Table 4.1). The subunit structure and the tetrameric assembly of wild-type and the mutant *Sc*MnSOD closely resemble each other (Fig. S4.2). Superimposition of all backbone atoms of the mutant tetramer onto those of the wild-type protein gives a root-mean-square deviation (RMSD) of 0.22 Å. Y34F *Sc*MnSOD maintains the strictly-conserved five-coordinate Mn at active site, and the substitution of Tyr34 causes only minimal changes to positioning and conformation of active-site residues (Fig. 4.1A). The Chi(1) and Chi(2) angles of Phe34 in Y34F *Sc*MnSOD shift by 0.7 °and 2.7 °, respectively, compared to those of Tyr34 in the wild-type enzyme.

An additional water molecule occupies the cavity created by the replacement of Tyr34 with phenylalanine in all four subunits in the unit cell of Y34F *Sc*MnSOD. This water has substituted for the –OH of Tyr34 in the wild-type enzyme by forming hydrogen bonds to Gln154 and the water molecule hydrogen bonded to His30 (Fig. 4.1A). Its presence at that location

Table 4.1. X-ray data collection and refinement statistics [a].

	Y34F *Sc*MnSOD
Data Collection	
X-Ray Source	APS BEAMLINE 24-ID-C
Detector	ADSC QUANTUM 315
Reflections observed	169216
Unique reflections	59948
Wavelength (Å)	0.9641
Resolution (Å)	1.88
Highest Resolution Shell (Å)	1.91–1.88
Space group	P1
R_{sym} (%) [b]	12.2 (54.7)
I/σ	12.1 (1.9)
Completeness (%)	94.6 (54.0)
Unit cell dimensions	
a (Å)	61.139
b (Å)	63.022
c (Å)	63.943
α (°)	112.19
β (°)	106.78
γ (°)	103.88
Wilson B value ($Å^2$)	22.5
Refinement	
Resolution (Å)	32.2 – 1.88
Reflections Used	59832
R_{work}(%)	18.98
R_{free} (%) [c]	23.13
Protein Molecules in Asymmetric Unit	4
Number of non-H atoms	
Protein	6658
Non-protein	231
RMS deviations	
Bond lengths (Å)	0.009
Bond angles (°)	1.149
Average B-factor ($Å^2$)	
Protein atoms	28.39
Non-protein atoms	29.51
PDB accession code	4E4E

a. Highest resolution shell shown in parenthesis.
b. $R_{sym} = \Sigma \mid I - \langle I \rangle \mid / \Sigma I$
c. R_{free} calculated using 5% of the data

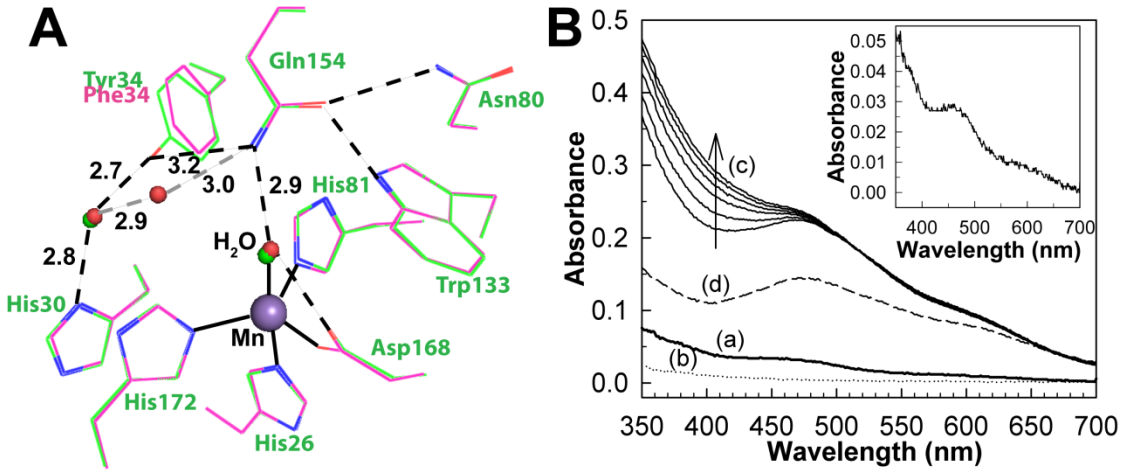

Figure 4.1. Active site structure and oxidation state of Y34F *Sc*MnSOD. (A) Superimposition of the active site of Y34F *Sc*MnSOD (chain A, red) onto that of wild-type *Sc*MnSOD (chain A, green). Coordination bonds are indicated as solid lines, and hydrogen bonds are shown as dashed lines in wild-type (black) and Y34F (gray) *Sc*MnSOD, respectively. The graphic was generated using the PyMOL Molecular Graphics System. (B) (a)&(b) Optical spectra of as-isolated (solid line) and reduced (dotted line, by sodium hydrosulfite) Y34F *Sc*MnSOD. Inset: The difference spectrum between as-isolated and reduced Y34F *Sc*MnSOD. (c) Optical spectra of Y34F *Sc*MnSOD oxidized by potassium permanganate ([$KMnO_4$]:[MnSOD] = 0.75:1) at pH 7.4 as measured over time. The spectra were recorded after mixing $KMnO_4$ with the enzyme for 0, 10, 20, 30, 45 and 60 min. (d) Reduction (dashed line) of Y34F *Sc*Mn^{3+}SOD (gave the last spectrum in c) by one equivalent of sodium ascorbate. The sample solutions contained 200 μM (in Mn) enzyme in 25 mM potassium phosphate (pH 7.4).

supports the importance of the hydrogen-bonding chain involving Tyr34 (Gln154···Tyr34···H_2O···His30) in the wild-type enzyme (21). This additional water molecule is also present in Y34 mutant (Y34A, Y34N, Y34H, and Y34V) human MnSOD (12). However, it was not observed in the crystal structure of human Y34F MnSOD, which had been carried out at a resolution similar to that of our study (1.9 Å) (9).

Like the Wild-type Enzyme, Y34F ScMn^{3+}SOD Contains both Five- and Six-coordinate Mn^{3+} Centers. Wild-type MnSODs are usually isolated in the oxidized state, Mn^{3+}SOD (3,22,23). Yeast MnSODs appear to be an exception, since we showed previously that wild-type yeast MnSODs from *S. cerevisiae* and *C. albicans* rest predominantly in the reduced state, Mn^{2+}SOD (4,5). This preference to be reduced is unchanged in Y34F *Sc*MnSOD (Fig. 4.1B-a). Also similar to wild-type *Sc*MnSOD is the observation of a small amount of Mn^{3+}SOD in the as-isolated Y34F *Sc*MnSOD, which absorbs below 400 nm in addition to the 480 nm band (Fig. 4.1B, inset).

As in the wild-type enzyme, the spectrum of Y34F *Sc*MnSOD immediately after oxidation is characteristic of five-coordinate Mn^{3+}SOD (Fig. 4.1B-c). Additional absorption intensity appeared at lower wavelengths (<400 nm) over time (Fig. 4.1B-c), which was proposed to result from formation of a six-coordinate Mn^{3+}SOD, with hydroxide as the sixth ligand (5). The intensity is blueshifted from ~390 nm in wild-type *Sc*Mn^{3+}SOD (5) to ~370 nm in Y34F *Sc*Mn^{3+}SOD (Fig. S4.3). The time to reach the final spectrum was shorter in the Y34F mutant protein (~45 min) (Fig. 4.1B-c) than in wild-type *Sc*MnSOD (~2 h) (5), indicating faster formation of the putative six-coordinate adduct in Y34F *Sc*Mn^{3+}SOD.

Y34F *Sc*Mn^{3+}SOD also resembles wild-type *Sc*Mn^{3+}SOD in that the six-coordinate adduct is more prone to reduction by ascorbate than the five-coordinate species (5), as revealed

by the fact that 1.0 equivalent of ascorbate selectively bleached the absorption of Y34F *Sc*Mn^{3+}SOD around 370 nm (Fig. 4.1B-d). This result suggests that the six-coordinate Mn^{3+} has a higher reduction potential than the five-coordinate Mn^{3+}. Six-coordinate Mn^{3+}SOD, with a high-spin d^4 center, displays strong Jahn-Teller distortion, which favors the Mn^{2+} over Mn^{3+} state. The slow formation of the six-coordinate adduct and its high reduction potential in both wild-type and the mutant yeast MnSOD are still not understood in detail, and we will continue exploring their origins in future.

Y34F ScMnSOD is Gated Exclusively toward "Inner-sphere" Pathway, yet still Displays Fast Catalysis. To examine the impact of the Tyr34 on catalysis by *Sc*MnSOD, we carried out pulse radiolysis studies on Y34F *Sc*MnSOD. The disappearance of various concentrations (2-50 μM) of O_2^- in solutions containing 1–5 μM Y34F *Sc*MnSOD was followed at 260 nm, and the observed traces were compared to previous data collected under identical conditions for wild-type MnSOD from *S. cerevisiae*, *C. albicans*, human, *E. coli*, and *D. radiodurans* (Fig. 4.2). When [O_2^-] was in seven-fold excess over [MnSOD], a relatively uninhibiting condition, human MnSOD, the most product-inhibited wild-type MnSOD known, already showed a depressed activity, while the O_2^- disappearance as a function of time was similar for each of the other four wild-type enzymes (Fig. 4.2A). Notably, substitution of Tyr34 caused *Sc*MnSOD to remove O_2^- more slowly under this condition than all of the wild-type enzymes, including wild-type human MnSOD (Fig. 4.2A).

We then increased the [O_2^-]:[MnSOD] ratio to 41, a condition where MnSOD from different organisms displays dramatically different efficiencies, due to different degrees of product inhibition (3). The fast decay of O_2^- within a few milliseconds after its generation is the

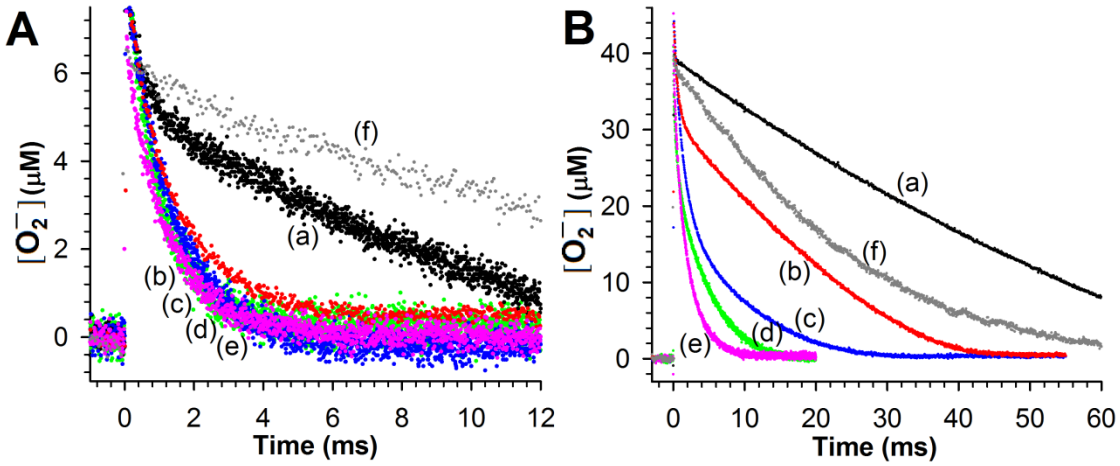

Figure 4.2. Decay of 7 μM (A), and 41 μM (B) O_2^- catalyzed by 1 μM (in Mn) human (a, black), *E. coli* (b, red), *D. radiodurans* (c, blue) MnSOD, *Sc*MnSOD (d, green), *Ca*MnSODc (e, pink) and Y34F *Sc*MnSOD (f,gray). The samples contained 10 mM potassium phosphate (pH 7), 10 mM sodium formate and 10 μM EDTA. The O_2^- concentrations in these figures are calculated from the absorbance at 260 nm.

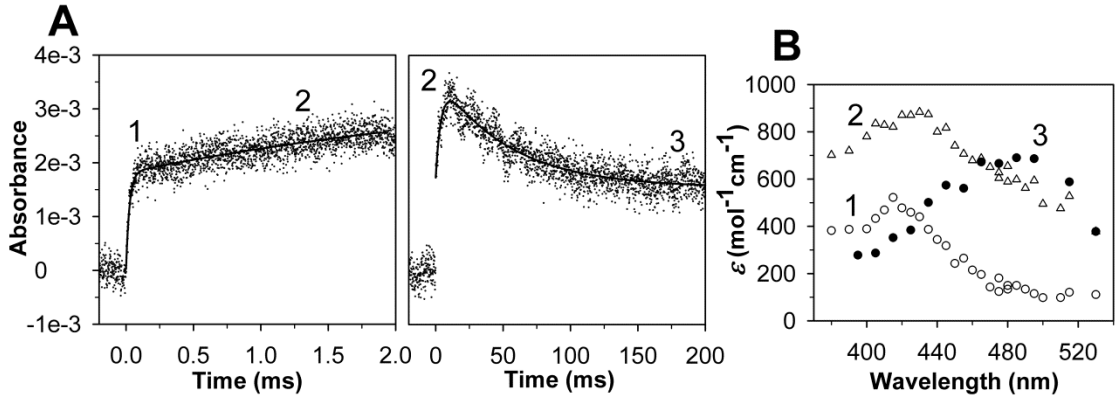

Figure 4.3. Mn^{3+} species observed from oxidation of Y34F *Sc*Mn^{2+}SODc by O_2^- in pulse radiolysis. (A) The absorbance change at 420 nm within 2 (left) and 200 (right) ms after pulse radiolysis generated initial O_2^- burst of 2.2 μM. Experimental data are shown in dots and fitted curves are shown in solid lines. (B) The spectra of the Mn^{3+} species (Int_1: hollow circles; Int_2: open triangles; Int_3: solid circles). The sample solutions contained 60 μM (in Mn) Y34F *Sc*MnSOD in 10 mM potassium phosphate (pH 7.4), 10 mM sodium formate, 120 μM H_2O_2, and 100 μM EDTA.

indicator of the "prompt protonation" pathway. Therefore, the absence of this fast decay in Y34F *Sc*MnSOD (Fig. 4.2B) indicates that the mutant protein is gated predominantly toward the "inner-sphere" pathway. Nevertheless, to our surprise, Y34F *Sc*MnSOD catalyzed the disappearance of O_2^- more efficiently than human MnSOD (Fig. 4.2B), even though the former is gated exclusively toward the "inner-sphere" pathway (k_2/k_3 <0.01, see below). The zero-order phase, characteristic of the presence of the Mn-peroxo complex, is controlled by the gating ratio k_2/k_3 and the dissociation rate of the bound peroxide (k_4). The fact that the zero-order phase was not as pronounced in Y34F *Sc*MnSOD as in wild-type *E. coli* or human MnSOD (Fig. 4.2B) suggests faster peroxide dissociation steps in Y34F *Sc*MnSOD (see below).

Scheme 4.2. Reduction of O_2^- by Y34F *Sc*Mn^{2+}SOD

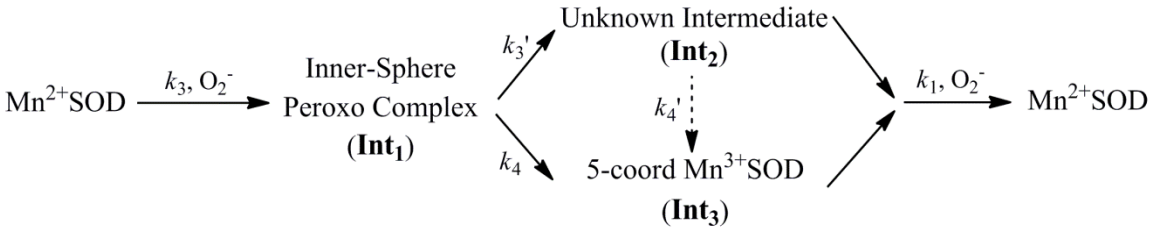

To measure individual rate constants, 60 μM of Y34F *Sc*Mn^{2+}SOD was pulse irradiated to react with substoichiometric amounts (2-3 μM) of O_2^-, and the appearance of Mn^{3+}SOD was followed (Materials and Methods). The absorbance measured at 420 nm within 2 ms after generation of O_2^- could be divided into two phases, a rapid emergence of absorption within 0.1 ms followed by a relatively slow increase that lasted for ~15 ms (Fig. 4.3A, left). Similar biphasic increases at 420 nm absorption have also been observed for several Y34 mutant human MnSOD (12). The 420 nm absorption of Y34F *Sc*MnSOD slowly decreased at a longer time scale (Fig. 4.3A, right), leading to formation of a Mn^{3+} species (Int_3) with an absorption

Table 4.2. Rate contants for wild-type MnSODs from *S. cerevisiae* and human and their Y34 mutant proteins

Enzyme	k_1 ($nM^{-1}s^{-1}$)	k_2 ($nM^{-1}s^{-1}$)	k_3 ($nM^{-1}s^{-1}$)	k_3' (s^{-1})	k_4' (s^{-1})	k_4 (s^{-1})
wild-type *Sc*MnSOD (4)	1.1-1.5	0.8	0.04–0.05	–	–	90-140
Y34F *Sc*MnSOD (this work)	– *	<0.01	0.70	310	20	~40
wild-type human MnSOD (3)	1.5	0.6	0.5	–	–	120
Y34F human MnSOD (12)	0.55	<0.02	0.46	–	–	52
Y34A human MnSOD (12)	0.25	<0.02	0.38	1600	330	–
Y34N human MnSOD (12)	0.14	<0.02	0.15	850	200	–
Y34H human MnSOD (12)	0.07	<0.02	0.04	250	61	–
Y34V human MnSOD (12)	0.15	<0.02	0.15	–	–	1000

* k_1 was not determined, because the reduction of *Sc*Mn^{3+}SOD by O_2^- is not stoichiometric in a long timescale.

maximum at ~480 nm (Fig. 4.3B), consistent with the well-characterized five-coordinate Mn^{3+}SOD (2,3).

We attribute the rapid and slow absorption increase in Fig. 4.3A (left) to emergence of Intermediate 1 (Int_1) and 2 (Int_2), respectively (Scheme 4.2). The data were fitted into a two-exponential model, and the rate constants and the molar extinction coefficients were calculated. The resulting spectrum of Int_1, which has an absorption maximum at ~415 nm (Fig. 4.3B), is identical to those reported for the Mn-peroxo complexes in numerous wild-type and mutant MnSODs (2,3,12). Int_2 is an intermediate with broad absorption in the visible range and a maximum at ~425 nm. (Fig. 4.3B) The structure of this intermediate is unknown, but species with similar spectral features have been observed in similar studies of Y34A, Y34H, and Y34N human MnSOD (12).

The substitution of Tyr34 caused dramatic changes to the kinetics of *Sc*MnSOD. The rate constant for the "prompt protonation" pathway, k_2 (Scheme 4.1), was too low to measure accurately. The rate constant for formation of the Mn-peroxo complex, k_3 (Scheme 4.1, 4.2), was dramatically elevated from 0.04–0.05 $nM^{-1}s^{-1}$ for wild-type *Sc*MnSOD to 0.70 $nM^{-1}s^{-1}$ for the mutant protein (Table 4.2), such that the overall rate constant for reduction of O_2^- by Mn^{2+}SOD, defined as a sum of k_2 and k_3, is similar in the wild type and the mutant protein. We define k_3' the rate constant for formation of Int_2 from the Mn-peroxo complex (Scheme 4.2). It was determined to be 310 s^{-1} for Y34F *Sc*MnSOD, comparable to that of Y34H human MnSOD, but lower than those of Y34A and Y34N human MnSOD (Table 4.2). The rate constant for formation of the five-coordinate Mn^{3+}SOD from Int_2, k_4' (Scheme 4.2), was determined to be 20 s^{-1} for Y34F *Sc*MnSOD, which is 3–16 fold lower than those determined for Y34 mutant human enzymes (Table 4.2).

Int_2 is the Active Mn^{3+} species in Y34F ScMnSOD. As we have shown that the mutant yeast enzyme reacts completely through the Mn-peroxo complex, the question arises: what is the Mn^{3+} species that oxidizes O_2^{-}? Is it Int_2 or the five-coordinate Mn^{3+}? Int_2 is a product from partial or full protonation of the Mn-peroxo complex. Formation of the five-coordinate Mn^{3+} from Int_2 is so slow (k_4' = 20 s^{-1}) that if the former were the oxidant, Y34F *Sc*MnSOD would be much slower than wild-type human MnSOD (k_4 = 120 s^{-1}) under inhibiting conditions. This contradicts our observation (Fig. 4.2B). Indeed, we were unable to fit our data to a mechanism in which formation of the five-coordinate Mn^{3+} is the rate limiting step (data not shown). By contrast, the experimental data (Fig. 4.2, 4A) with various enzyme and O_2^{-} concentrations fit well to a mechanism in which Int_2 is the active Mn^{3+} species (Fig. S4.4).

Fast and Slow Proton Transfer Pathways in Y34F ScMnSOD. Increased pH lowers the overall rate of protonation of the Mn-peroxo complex, which is a combination of k_3', k_4, and k_4' (see below), in Y34F *Sc*MnSOD. At pH 7.0, the overall protonation rate equals to k_3' (310 s^{-1}); at pH 8.5, it dropped by a factor of three to ~100 s^{-1} (Fig. 4.4A). Also noticeably, the rapid absorption increase at 420 nm, resulting from formation of Int_2, gradually disappears at increased pH (Fig. 4.4B). These facts were not caused by depression of k_3', which, calculated via fitting the data in Fig. 4.4B, stayed almost the same from pH 7.0–8.5 (Fig. 4.4A, inset). The most likely explanation is that Int_2 was no longer formed at increased pH. The same experiments recorded at 480 nm clearly indicated generation of the five-coordinate Mn^{3+} directly from the peroxo complex at pH ≥ 8 (Fig. S4.5). Protonation of the peroxo complex in Y34F *Sc*MnSOD appears to partition into two pathways, a fast one at low pH leading to Int_2 and a slow one at high pH leading directly to the five-coordinate Mn^{3+}. The gating between the two pathways has a p*K* of

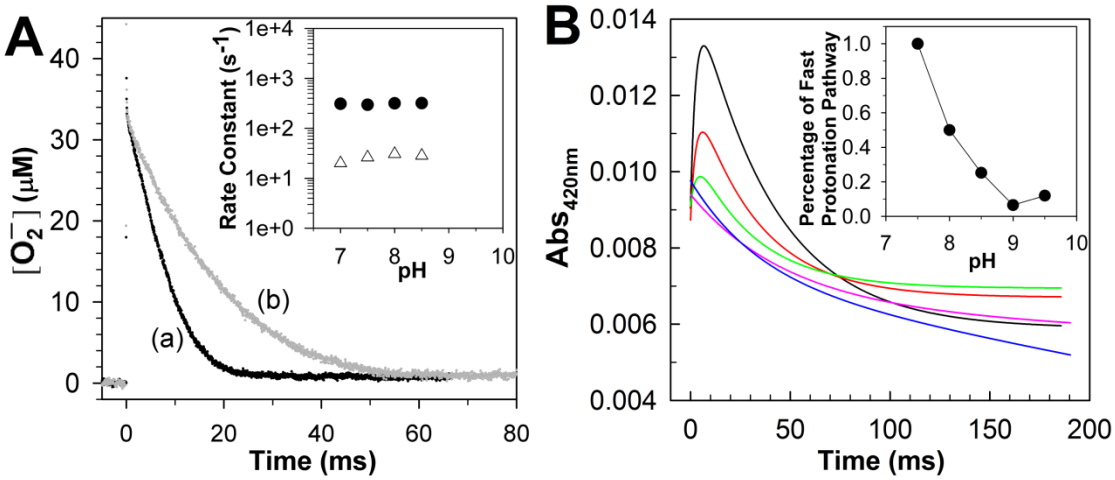

Figure 4.4. Protonation of the inner-sphere peroxo complex as a function of pH in Y34F *Sc*MnSOD. (A) Decay of 41 μM O_2^- catalyzed by 5 μM (in Mn) Y34F *Sc*MnSOD at pH 7.0 (a) and 8.5 (b). The solutions contained 10 mM potassium phosphate, 10 mM sodium formate, 1 mM Tris-Cl and 10 μM EDTA. Inset: rate constant k_3'(solid circles) and k_4' (hollow triangles) as functions of pH. (B) The absorbance change at 420 nm upon generation of 8.9 μM O_2^- at pH 7.5 (black), 8.0 (red), 8.5 (green), 9.0 (purple), and 9.5 (blue). Fitted curves generated from PRWIN (13) are shown. The solutions contained 80 μM (in Mn) Y34F *Sc*MnSOD in 15 mM potassium phosphate, 10 mM sodium formate, 1 mM Tris-Cl, 160 μM H_2O_2, and 100 μM EDTA. Inset: percentage of the fast protonation pathway as a function of pH, calculated by dividing the highest 420 nm absorbance at each pH to that at pH 7.5, assuming that at pH 7.5 the enzyme reacts solely through the fast proton transfer pathway.

~8, and the enzyme reacts completely through the slow pathway at pH ≥ 9 (Fig. 4.4B, inset). The rate constant for the slow pathway (k_4) was calculated to be ~40 s^{-1}, by fitting the absorbance change at 480 nm to a first-order reaction (Fig. S4.5-A).

Discussion

Tyr34 is critical for "Prompt Protonation" Pathway. To examine the role of Tyr34 in catalysis by *Sc*MnSOD, we replaced Tyr34 with phenylalanine. Wild-type *Sc*MnSOD reacts predominantly through the "prompt protonation" pathway, with a gating ratio of 16–20 (Table 4.2) (4,5). As in Y34 mutant human enzymes (12), the "prompt protonation" pathway is completely disrupted in Y34F *Sc*MnSOD. In Y34F *Sc*MnSOD, k_3 is close in value (0.70 $nM^{-1}s^{-1}$) to k_2 of wild-type *Sc*MnSOD (0.80 $nM^{-1}s^{-1}$) (Table 4.2), indicating that the "prompt protonation" pathway is substituted by the "inner-sphere" pathway in the mutant yeast enzyme.

Putative Six-coordinate Int_2 is Associated with the Additional Second-sphere Water. Spectroscopic analysis revealed that the resting state of wild-type yeast Mn^{3+}SODs consists of both five- and six-coordinate Mn^{3+} centers (5). In wild-type yeast enzymes, the absorption intensities around 480 nm and <400 nm correlate with two effective ^{55}Mn hyperfine couplings in the EPR spectra, consistent with five- and six-coordinate Mn^{3+} centers, respectively (5). Like the wild-type enzyme, Y34F *Sc*Mn^{3+}SOD also absorbs at <400 nm in addition to the 480 nm band (Fig. 4.1B), suggesting that the oxidized mutant protein also contains both five- and six-coordinate Mn^{3+}.

Similar to several Y34 mutant human MnSOD (12), an intermediate (Int_2, Scheme 4.2) with an absorption maximum at 425 nm was observed when Y34F *Sc*Mn^{2+}SOD was oxidized by

O_2^- (Fig. 4.3). Because k_3', the rate constant for formation of Int_2, is independent of ionic strength in Y34 mutant human MnSOD, generation of Int_2 is thought to involve an isomerization (12). Int_2 was proposed to be six-coodinate where the metal ion binds an additional water molecule (12).

The blue shifting of the Mn^{3+}SOD spectra could be ascribed to binding of a new, strong ligand in the equatorial plane of the Mn^{3+} ion, causing the coordination geometry to switch from trigonal bipyramidal to distorted-octahedral and thus elevating the energies of the d-d transitions. Assuming that Int_2 observed in catalysis is alsosix-coordinate, it must differ from the six-coordinate species in the resting Mn^{3+}SOD, because the two have distinct absorption maxima (Fig. 4.1B, 3B). A simple explanation for the different extent of blue shifting is that the coordination geometry is slightly different in the six-coordinate species present under catalytic conditions from the non-catalytic form. The sixth ligand was proposed to be hydroxide in the resting wild-type *Sc*Mn^{3+}SOD (5). Because its binding to the Mn^{3+} center is facile at neutral pH, the sixth ligand could also be a water molecule. Nevertheless, this conclusion does not necessarily hold for Int_2 in which H_2O, OH^-, or OOH^- are all potential candidates for the sixth ligand (see below).

All Y34 mutant proteins shown to react via Int_2 contain an additional second sphere water molecule occupying the cavity created by the replacement of Tyr34 (Fig. 4.1A) (12), suggesting that the observation of Int_2 and the presence of the additional water may be correlated. However, neither the additional water nor Int_2 are found in any Y34F mutant protein that has been studied previously (3,9), suggesting a particularly important role of Tyr34 in wild-type *Sc*MnSOD. Previously we proposed that fast catalysis by yeast MnSOD could be related to fast proton transfer from an outer-sphere solvent molecule (5). Particularly in Y34 mutant proteins,

protonation of the peroxo complex is always fast so long as the additional water molecule is present. One would therefore expect that the additional second-sphere water in these Y34 mutant proteins donates one of the two protons to the bound peroxyl group.

In order to explore the catalytic properties of the six-coordinate species in wild-type yeast MnSODs, we reduced *Sc*Mn^{3+}SOD or *Ca*Mn^{3+}SOD (40–80 μM) with substoichiometric amounts of O_2^- and followed the absorbance change at 475 nm (Fig. S4.6). The resting form of oxidized yeast MnSODs is a mixture of five- and six-coordinate Mn^{3+}SOD. In the case of the six-coordinate Mn^{3+}SOD being a "dead-end" complex, k_1 would be significantly reduced due to inhibition by the sixth ligand. However, k_1 was determined to be ~1.0–1.3 $\times 10^9$ $M^{-1}s^{-1}$ for yeast wild-type MnSODs and is comparable to that of other wild-type MnSODs (Table 4.2), whose catalysis apparently only involves five-coordinate Mn^{3+} species. Therefore, the six-coordinate Mn^{3+} center with two solvent molecules bound is equally as catalytically competent as the well-characterized five-coordinate Mn^{3+}. This, along with the correlation between the additional second-sphere water molecule and fast proton transfer, suggests that the sixth ligand in Int_2 is most likely a solvent molecule. Unfortunately, it is difficult to confirm the structure of Int_2 using spectroscopic tools, due to short lifetime (~200 ms) of this intermediate.

Proposed Mechanisms for Y34F ScMnSOD in which Six-coordinate Int_2 is the Active Species. Y34F *Sc*MnSOD is even more gated through the inner-sphere Mn-peroxo complex, Int_1, than is wild-type human MnSOD, as indicated by their gating ratios (k_2/k_3) of <0.01 and 1, respectively (Table 4.2). Nevertheless, to our surprise, the mutant *Sc*MnSOD is faster than human MnSOD when O_2^- levels are high (Fig. 4.2B). In the case of human MnSOD, high [O_2^-] causes the overall reaction to slow because of the relatively low rate of peroxide loss (120 s^{-1} at

pH 7) upon protonation of Int_1. In the case of Y34F *Sc*MnSOD, by contrast, protonation and loss of peroxide is much faster (310 s^{-1} at pH 7). We conclude from curve fitting (Fig. S4.4) that Int_2 is the active Mn^{3+} species that oxidizes O_2^- in Y34F *Sc*MnSOD. Although Int_2 has been observed during reaction of several Y34 mutant human enzymes, the active species that oxidizes O_2^- in those systems remains the five-coordinate Mn^{3+} (12). Since Int_2 is putatively six-coordinate, Y34F *Sc*MnSOD represents the first MnSOD, whose catalysis may involve a six-coordinate Mn^{3+}.

Scheme 4.3. Proposed mechanisms for Y34F *Sc*MnSOD

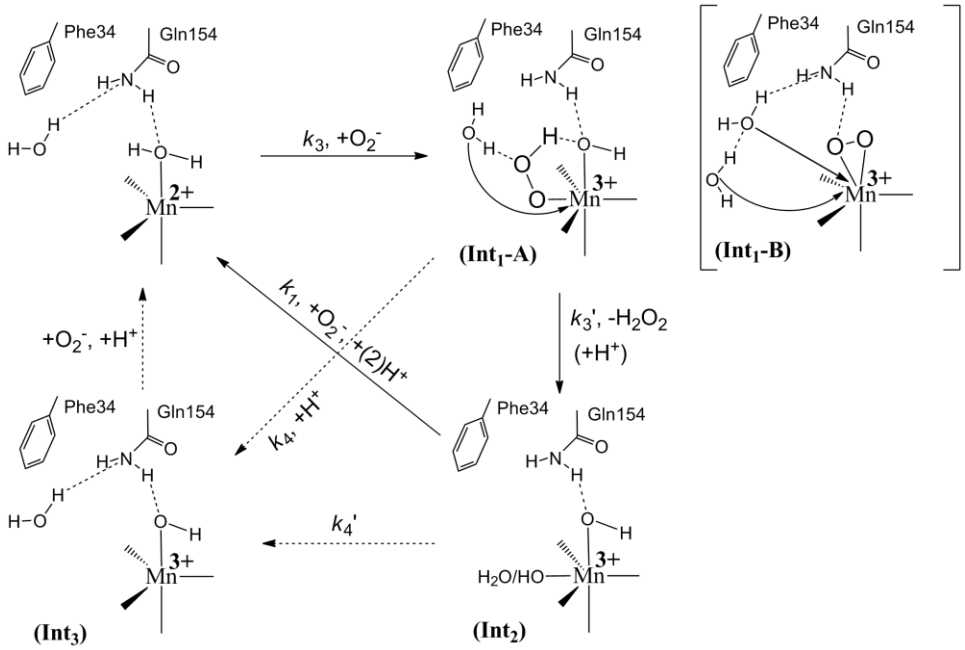

Here we propose a mechanism to describe the catalytic cycle of Y34F *Sc*MnSOD (Mechanism A, Scheme 4.3, involving Int_1-A). It involves binding of O_2^- to Mn^{2+} in the sixth coordination position close to Tyr34 prior to inner-sphere electron transfer, as proposed in the "5–6–5" mechanism (24), referring to increase of coordination number from five to six upon binding of

O_2^-, and decrease of coordination number from six to five upon dissociation of H_2O_2. The solvent ligand instantaneously transfers the first proton to the distal oxygen of the newly formed O_2^{2-} (25), leading to a six-coordinate end-on Mn^{3+}-hydroperoxo species, which in this mechanism corresponds to the inner-sphere Mn-peroxo complex. The additional outer-sphere water molecule then transfers a second proton to the proximal oxygen of HOO^-, leading to dissociation of the peroxide ligand. The vacant sixth ligand site is then occupied by a second-sphere solvent molecule. We formulate Int_2 as a six- coordinate Mn^{3+} center binding two solvent molecules. In the other half reaction, O_2^- first replaces the solvent molecule in the sixth ligand site (26), before it is oxidized by the Mn^{3+} ion.

Mechanism A is strongly supported by numerous experimental and computational studies. The "5–6–5" mechanism is supported by the fact that azide, an analog of O_2^-, binds to the metal in the sixth coordination site in Fe and MnSOD (24). Cryotrapped *Ec*MnSOD crystallized at pH 8.5 binds an additional water in the same sixth ligand site (27). These facts strongly corroborate binding of O_2^- in the sixth ligand site close to Tyr34. Several theoretical calculations suggest that the most stable conformation of a bound peroxyl is end-on (26,28). A density functional study by Carrasco *et. al.* indicates that the most probable candidate for the Mn-peroxo complex is an end-on Mn^{3+}-hydroperoxo complex with HOO^- pointing toward the solvent ligand (28).

The structure of the Mn-peroxo complex is one of the most controversial topics in MnSOD research. To test the feasibility of Mechanism A, we modeled an end-on Mn^{3+}-hydroperoxo species in the active site of Y34F *Sc*MnSOD. The O1 of HOO^- in the model was placed at the same (x, y, z) coordinates as the N1 of azide in the six-coordinate azide-MnSOD (PDB code: 1MNG) (Fig. 4.5). HOO^-, sitting in the sixth coordination site, does not have unfavorable steric interactions with the active-site residues. The only adjustment needed for a

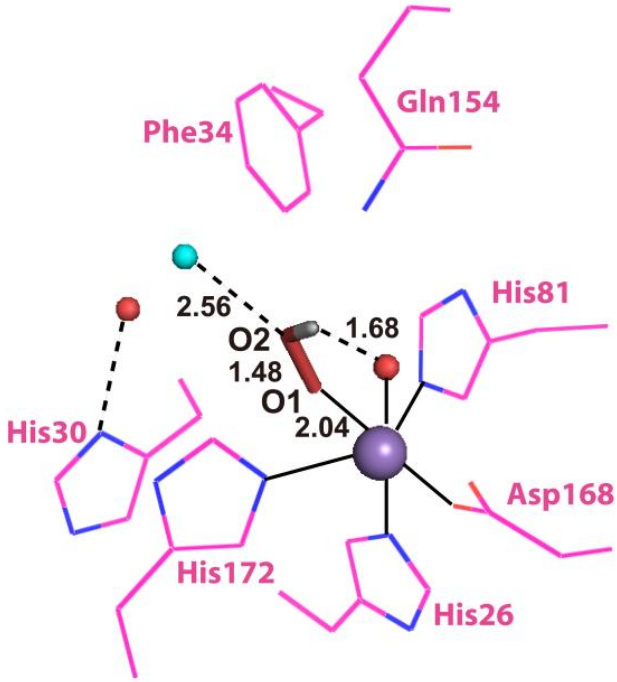

Figure 4.5. A suggestive end-on model of the inner-sphere Mn-peroxo complex built from the crystal structure of Y34F *Sc*MnSOD (chain A). The graphic was generated using the PyMOL Molecular Graphics System. Manganese ions are shown as purple spheres. Peroxyl groups are shown as red sticks with hydrogen atoms in gray. Existing and hypothetical solvent molecules are shown as red and cyan spheres, respectively.

good fit was a small displacement of the water molecule that has substituted for the –OH of Tyr34 to a position further away (~0.85 Å) from the Mn. The proposed new position for this shifted solvent is indicated in cyan in Fig. 4.5, which should be compared with Fig. 4.1A.When the Mn–O1(HOO$^-$)–O2(HOO$^-$) angle was modulated between 90 ° and 180 °, the distance between O2(HOO$^-$) and the additional water molecule in Fig. 4.1A is always <2.0 Å, suggesting that this water molecule would be in close contact with the bound HOO$^-$, and thus proton transfer from the former to the latter could be quite facile. This is consistent with the fast protonation rates observed for Y34F *Sc*MnSOD (Fig. 4.2B, 4A) and several Y34 mutant human MnSOD (Table 4.2).

There is another mechanism (Mechanism B, Scheme 4.3, involving Int$_1$-B) that has been supported by many researchers. The major distinction between Mechanism A and B lies in the structure of the inner-sphere Mn-peroxo complex. In Mechanism B the reaction of O_2^- with Mn^{2+}SOD initiates from displacement of the solvent ligand by O_2^- without occurrence of any proton transfer, and the peroxo complex is a six-coordinate Mn^{3+} binding a side-on O_2^{2-} (1,7). The displaced solvent molecule would become part of the water chain extending from active site to dimer interface (Fig. S4.7). The side-on peroxo then would need to accept two protons, either through the hydrogen bond chain extending from Gln154 or through direct hydrogen-bonding interactions with second-sphere water molecules. The structure of Int$_2$ and the process of oxidation of O_2^- are the same as in Mechanism A.

Formulation of the Mn-peroxo complex as a side-on Mn^{3+}-peroxo species has been proposed based on computational and spectroscopic studies (6,7), and on the crystal structure of peroxide-soaked *Ec*MnSOD showing side-on binding of peroxide to active-site Mn (Fig. S4.8-A) (29). The active site structure in Fig. S4.8-A, although determined under cryo conditions,

provides a potential pathway for protonation of the side-on peroxo complex through coordination of a water molecule in the sixth ligand site. An end-on Mn-hydroperoxo species is observed in two out of four chains in the same structure (Fig. S4.8-B), and it could be a product of the protonation implied in Fig. S4.8-A.

Here we favor Mechanism A over B, because, in the former, the reaction from the Mn-peroxo complex to Int_2 has a much simpler mechanism. This reaction in Mechanism A requires transfer of one proton and translocation of one solvent molecule, whereas in Mechanism B it requires transfer of two protons and translocation of two solvent molecules. Moreover, one would expect to observe additional intermediates between Int_1 and Int_2, if Mechanism B were in fact occurring.

The Y34 mutant MnSODs provide ideal systems for studying the reaction mechanism of product inhibition. Compared to wild-type MnSODs, in the Y34 mutant proteins, three instead of two Mn^{3+} species are observed from the "inner-sphere" pathway, thus making it easier to break down the pathway into individual steps, including formation of the peroxo complex and transfer of each of the two protons. We will continue our exploration of the mechanism of product inhibition through theoretical calculations in the future.

In Y34F ScMnSOD the Gating between Two Proton Transfer Pathways is Controlled by pH. MnSOD is well known for the gating between the "prompt protonation" and "inner-sphere" pathways (Scheme 4.1), based on the likelihood of reduction of O_2^- going through the Mn-peroxo complex. We report here that protonation of the peroxo complex in Y34F *Sc*MnSOD is also gated between a fast and a slow pathway (Fig. 4.4), with the rate constant differing by ~7

fold. The fast pathway goes through the putative six-coordinate Int_2, while the slow pathway leads directly to the five-coordinate Mn^{3+}SOD and occurs in all MnSODs (Scheme 4.2).

Previous studies on bacterial reaction centers (RCs) elucidated mechanisms for electron transfer coupled with multiple proton transfer pathways, and the gating is controlled by conformational change of the protein (30). In Y34F *Sc*MnSOD, by contrast, the gating is pH dependent. The fast pathway dominates at neutral pH, while the slow pathway dominates at increasing pH with a p*K* ~8 (Fig. 4.4B, inset). Examples of "fast" and "slow" proton transfer being pH dependent and independent, respectively, have been reported for metalloenzymes (31). The pH effects could result from deprotonation of the active-site water molecules, especially the one that has substituted the –OH of Tyr34, at high pH. If the additional solvent molecule stays as a H_2O, it could donate a proton quickly to the Mn-peroxo complex. When it is deprotonated at increasing pH and forms a OH^-, the fast proton transfer is shut down, and the bound peroxyl needs to get a proton through the slow pathway that occurs in all MnSODs.

Formation of the six-coordinate Int_2, which is coupled with the fast proton transfer pathway, no longer occurs at high pH. Therefore, at high pH, the five-coordinate Mn^{3+} generated through the slow proton transfer pathway becomes the active species (Scheme 4.2, 4.3). Because we were unable to observe the six-coordinate species at high pH, either the sixth ligand is not a hydroxide, or binding of a hydroxide is a relatively slow process if not preceded by the proposed fast proton transfer. It is the first time for gating between multiple proton transfer pathways to be reported in any wild-type or mutant MnSOD.

A Six-coordinate Mn^{3+} could be An Active Species in Wild-type Yeast MnSOD. Two unique biophysical properties distinguish yeast MnSODs from any previously characterized

MnSOD. First, yeast MnSODs rest predominantly in the reduced 2+ form (4,5), while all other MnSODs rest ≥ 50% in the oxidized 3+ form (3,22,23). Second, yeast Mn^{3+}SODs contain both five- and six-coordinate Mn^{3+} centers (5), while only the five-coordinate Mn^{3+} is present in oxidized MnSODs from other organisms (32). Y34F *Sc*MnSOD resembles the wild-type enzyme in that it rests as Mn^{2+}SOD and is oxidized to a mixture of five- and six-coordinate Mn^{3+} centers (Fig. 4.1B).

The positioning of Gln154 has been proposed to control the resting oxidation state of MnSOD (6,33,34). Several theoretical studies suggest that the solvent ligand is a H_2O when the enzyme is reduced, and a OH^- when it is oxidized (35). Previously we revealed that the increased separation of the Gln154 side chain from the metal ion in *Sc*MnSOD leads to a smaller stabilization of OH^- vs. H_2O and thus a relative stabilization of the 2+ state vs. 3+ state (5). On this basis, we would predict that the solvent ligands in wild-type and the mutant yeast Mn^{3+}SODs are less acidic than those in other Mn^{3+}SODs, due to stabilization of H_2O relative to OH^- in the yeast enzymes.

Electron-withdrawing/donating effects of ligands impact the coordination number of numerous metal complexes. The presence of electron-withdrawing substituents increases the propensity of a five-coordinate Mn^{3+} complex to bind a sixth ligand, via increasing the electrophilicity of the Mn (36). The presence of electron-donating methyl groups favors formation of an end-on over a side-on Mn^{3+}-peroxo (37). Because H_2O is a poorer electron donor than OH^-, the Mn^{3+} centers of the yeast enzymes are predicted to have higher electrophilicity than those of other Mn^{3+}SODs, which could explain the tendency of yeast Mn^{3+}SODs to bind another solvent molecule.

Nevertheless, Fe^{3+}-substituted *Ec*MnSOD, compared to wild-type *Ec*Fe^{3+}SOD, has a much higher affinity for OH^-, even though the Gln residue in *Ec*MnSOD is much closely placed to the metal ion (38). In addition, there is no experimental evidence for OH^- binding to Mn^{3+}-substituted *Ec*FeSOD at neutral pH, even though the Gln residue in *Ec*FeSOD is very far away from the metal ion (33). We will thus continue exploring the origin of the six-coordinate Mn^{3+} centers in yeast MnSODs in the future.

Although Y34F *Sc*MnSOD and several Y34 mutant human enzymes share similar active sites and formation of the six-coordinate Int_2, only in the mutant yeast MnSOD does Int_2 react with O_2^-. This may result from the fact that Y34F *Sc*Mn^{3+}SOD is inclined to form a six-coordinate Mn^{3+} adduct. Because wild-type and the mutant yeast Mn^{3+}SODs are both composed of five- and six-coordinate species (5), the active Mn^{3+} species in wild-type yeast MnSODs could also be six-coordinate. Indeed, as discussed above, in wild-type yeast enzymes, the six-coordinate Mn^{3+} with two solvent molecules bound is equally as catalytically active as the five-coordinate Mn^{3+}. Moreover, our recent work revealed that catalysis by wild-type yeast MnSODs may involve fast proton transfer (5). Compared to that of human MnSOD, the catalytic reactivity of wild-type yeast enzymes is significantly more decreased at high pH with indications of depression of the protonation rate (5). Therefore, the mechanism proposed for Y34F *Sc*MnSOD could well apply to wild-type yeast enzymes. Decay of the Mn-peroxo complex and the six-coordinate Int_2 may be too fast to be detectible in catalysis by wild-type yeast enzymes under the conditions of our experiments.

In conclusion, the replacement of Tyr34 with phenylalanine (Y34F) causes *Sc*MnSOD to react completely through the "inner-sphere" pathway. Y34F *Sc*MnSOD has fast catalysis due to a novel mechanism in which a putative six-coordinate Mn^{3+} species actively reacts with O_2^- at

neutral pH. Formation of this six-coordinate species and occurrence of fast proton transfer could relate to the presence of an additional active-site solvent molecule. Protonation of the inner-sphere Mn-peroxo complex has two distinct pathways with the gating controlled by pH. Our studies on Y34F *Sc*MnSOD provide novel perspectives on the mechanism of MnSOD involving active six-coordinate Mn^{3+} species and gating between multiple proton transfer pathways. Because both wild-type and the Y34F mutant yeast Mn^{3+}SOD have the tendency to become six-coordinate, the active Mn^{3+} species in the catalysis by wild-type yeast MnSODs could also contain a six-coordinate center.

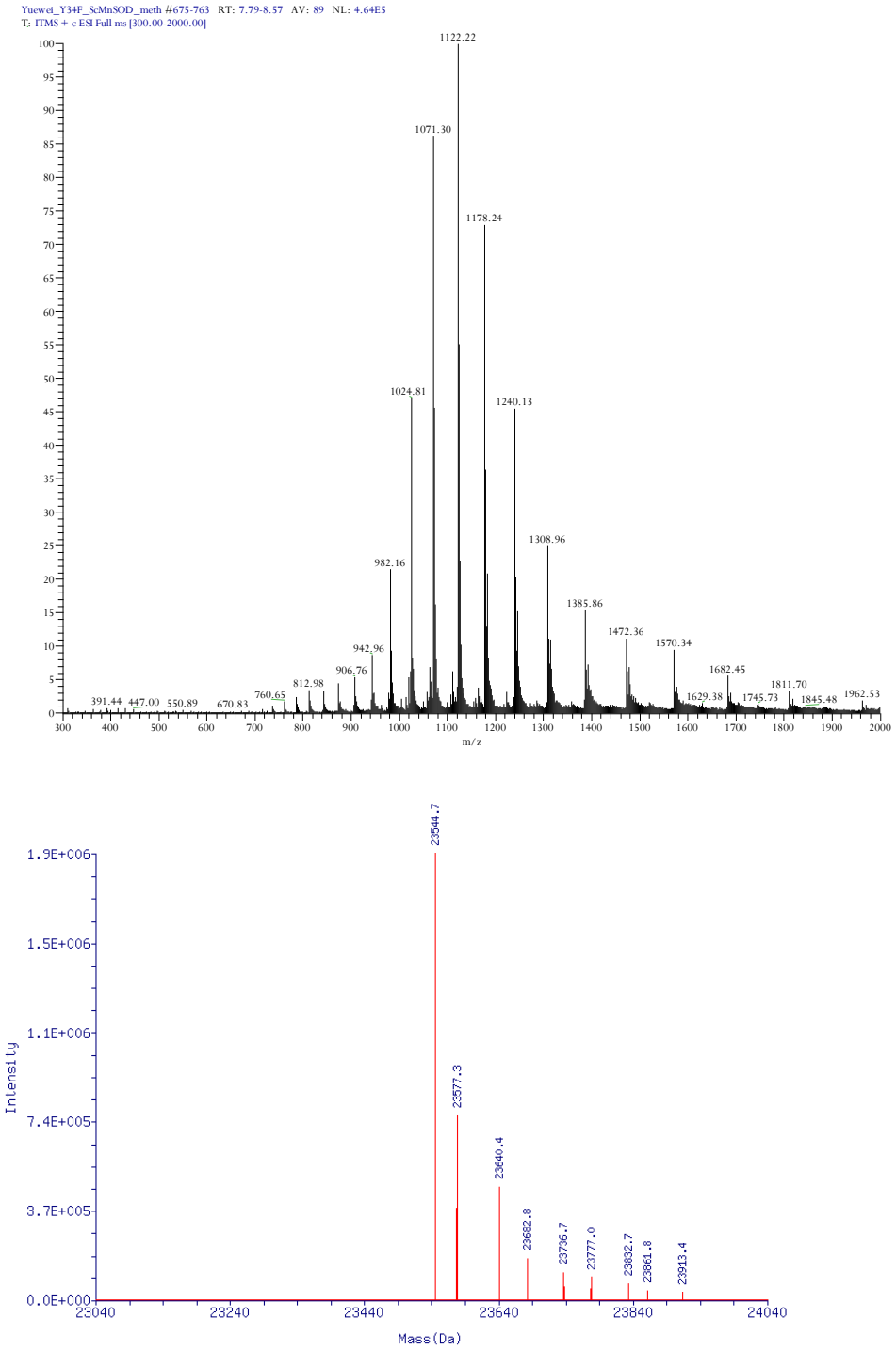

Figure S4.1. Electrospray-ionization mass spectra (top panel) of methylated Y34F *Sc*MnSOD and its reconstructed mass distribution profiles (bottom panel). Ordinate units of intensity are arbitrary and the abscissa units of average molecular mass are in Daltons. The calculated mass is 23,545 Da, and the expected mass is 23,546 Da.

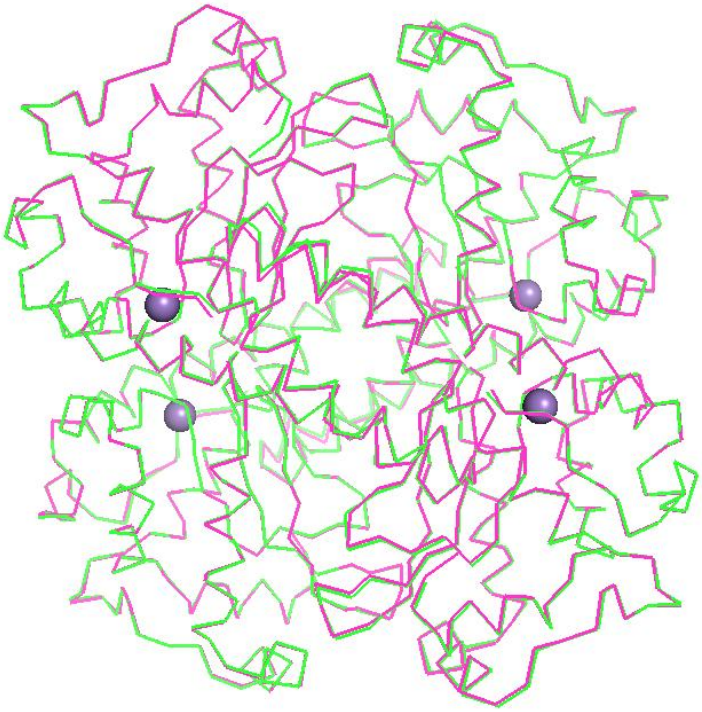

Figure S4.2. Superimposition of Y34F *Sc*MnSOD tetramer (red) onto wild-type *Sc*MnSOD tetramer (green). The graphic was generated using the PyMOL Molecular Graphics System. Mn atoms are shown in purple spheres.

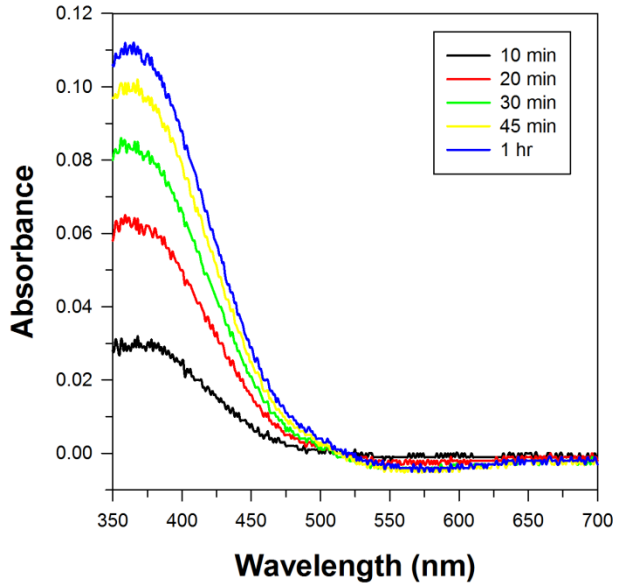

Figure S4.3. The difference absorption band of Y34F *Sc*Mn^{3+}SOD as measured over time. Y34F *Sc*MnSOD was oxidized by potassium permanganate ([$KMnO_4$]:[MnSOD] = 0.75:1) at pH 7.4. Time 0 refers to the start of the first scan immediately after mixing $KMnO_4$ with the enzyme. The sample solution contained 200 μM (in Mn) enzyme in 25 mM potassium phosphate (pH 7.4).

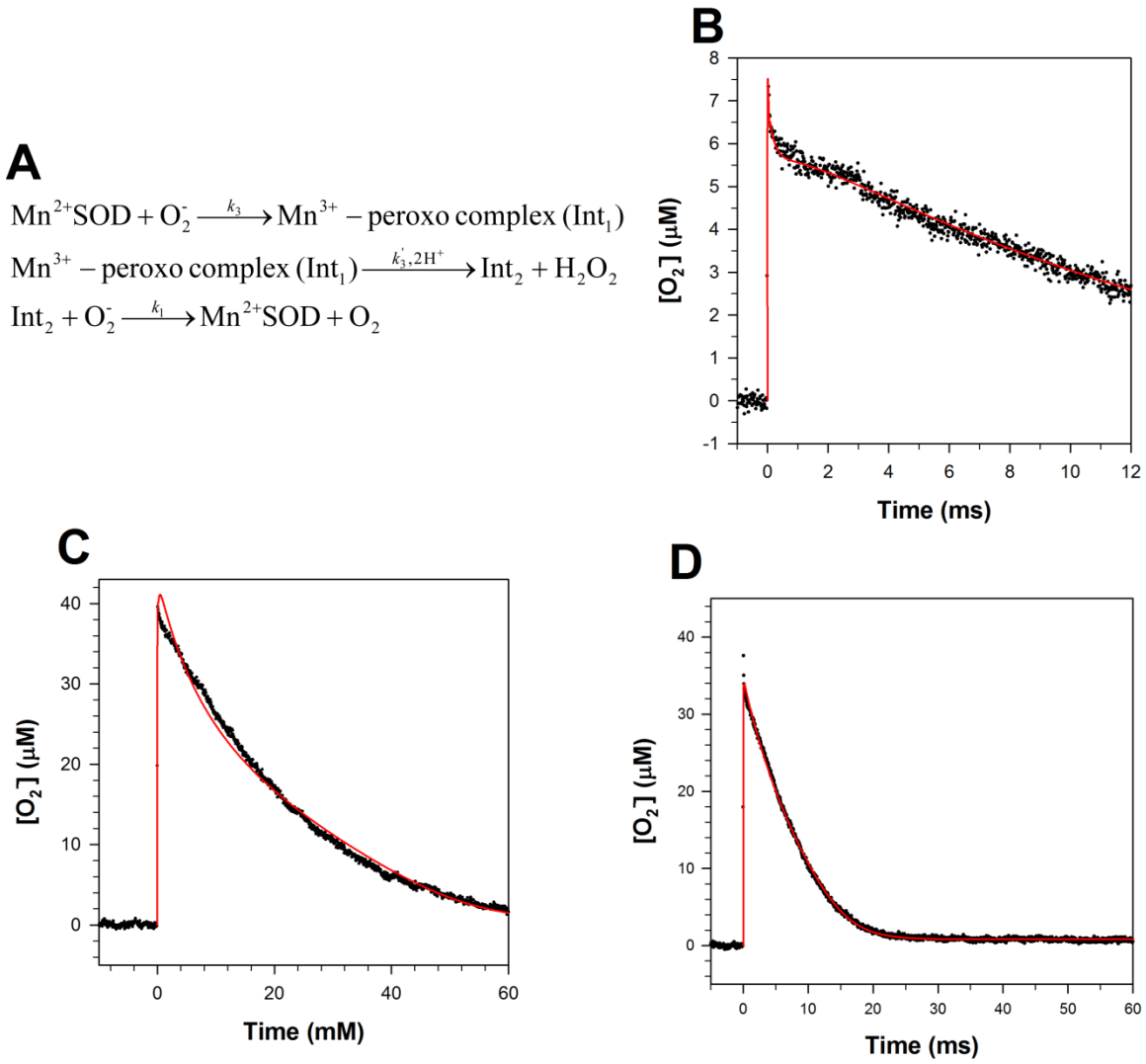

Figure S4.4. Fitting the disappearance of O_2^- catalyzed by Y34F *Sc*MnSOD at pH 7 into a mechanism in which Int_2 is the active species (A). The O_2^- and enzyme concentrations are: (B) 1 μM MnSOD and 7 μM O_2^-; (C) 1 μM MnSOD and 41 μM O_2^-; (D) 5 μM MnSOD and 41 μM O_2^-. k_3 (7×10^8 M^{-1} s^{-1}) and k_3' (310 s^{-1}) determined individually from the oxidation of Mn^{2+}SOD by O_2^- are used for the fitting. We assume that k_2 is negligible and k_1 is comparable to k_3. Experimental data are shown in black dots, and the fitted curves are shown in red lines. The sample contained 10 mM potassium phosphate (pH 7), 10 mM sodium formate and 10 μM EDTA. The O_2^- concentrations are calculated from the absorbance at 260 nm.

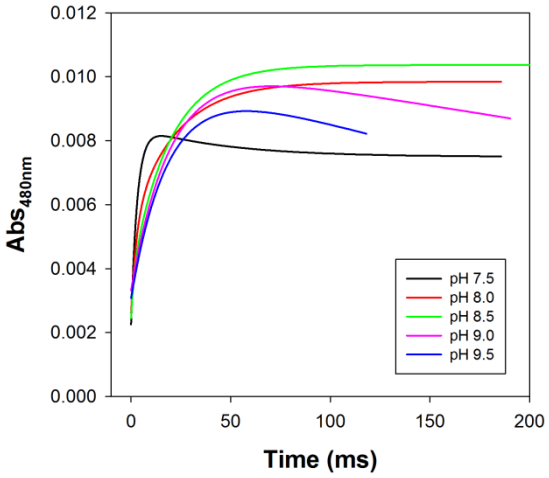

Figure S4.5. Dependence of decomposition of the product-inhibited complex on pH in Y34F *Sc*MnSOD. The absorbance change at 480 nm upon generation of 8.9 μM O_2^- as a function of pH is shown. Fitted curves generated from PRWIN (13) are shown. The solutions contained 80 μM MnSOD (in Mn) in 15 mM potassium phosphate, 10 mM sodium formate, 1 mM Tris-Cl, 160 μM H_2O_2, and 100 μM EDTA.

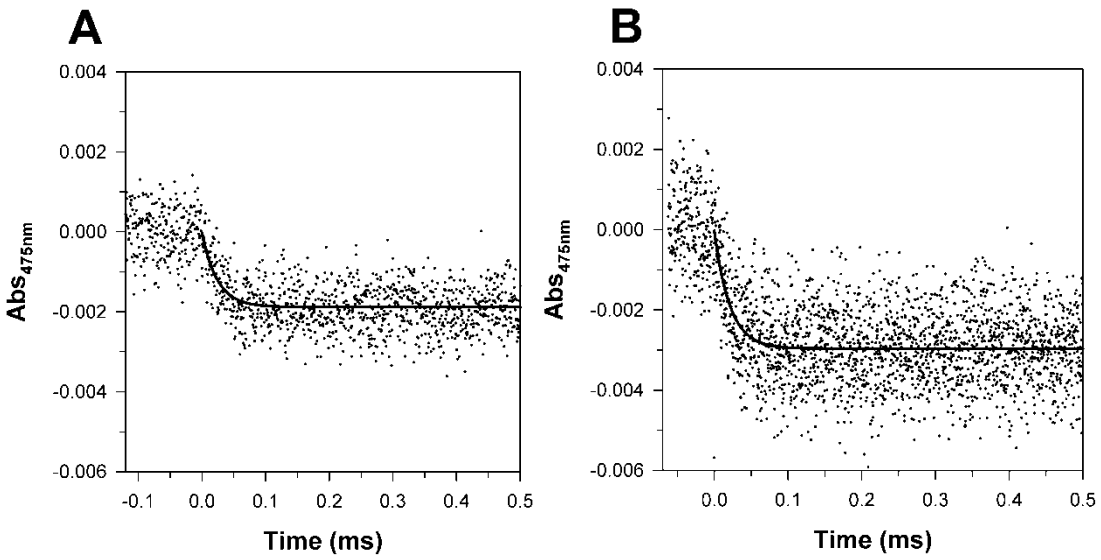

Figure S4.6. Reduction of wild-type *Sc*Mn^{3+}SODc (A) and *Ca*Mn^{3+}SODc (B) by O_2^- in pulse radiolysis. The formation of Mn^{2+}SOD is indicated by decrease of absorbance at 475 nm over time upon generation of 2.2 μM O_2^-. The sample solutions contained 40 μM (in Mn) enzyme, 10 mM potassium phosphate (pH 7), 10 mM sodium formate, and 100 μM EDTA. The oxidized enzymes were prepared by treating the as-isolated yeast enzymes with 0.75 equiv of $KMnO_4$, letting them sit at room temperature for 2 hr, and then buffer-exchanged to remove free metal ions.

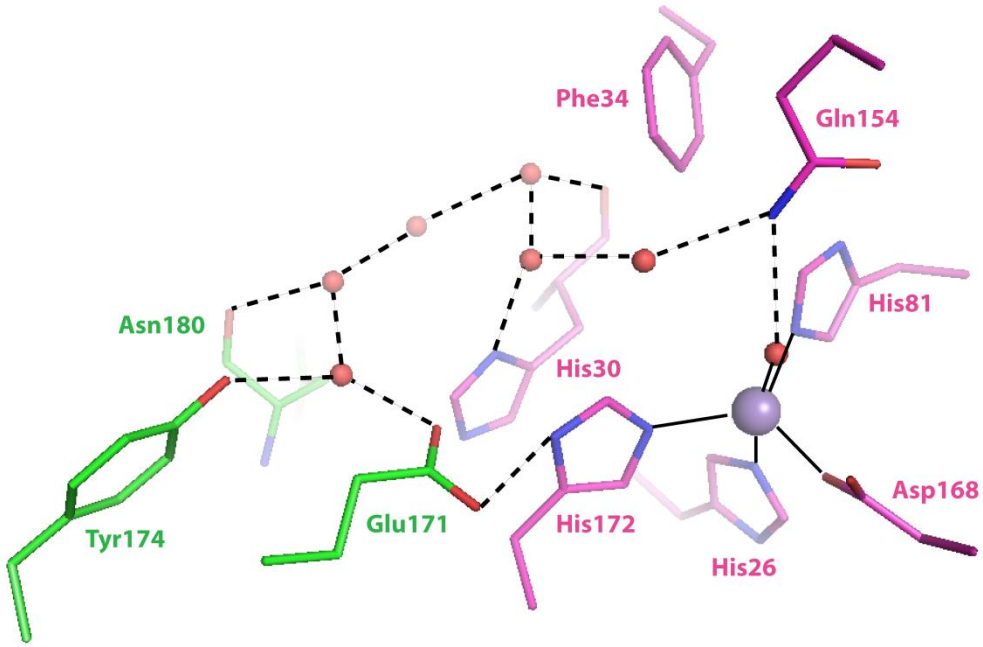

Figure S4.7. The water chain extending from active site to dimer interface in Y34F *Sc*MnSOD. Chain A and B are colored in red and green, respectively. The graphic was generated using the PyMOL Molecular Graphics System. Manganese ions are shown as purple spheres. Coordination and hydrogen bonds are indicated as solid and dashed lines, respectively.

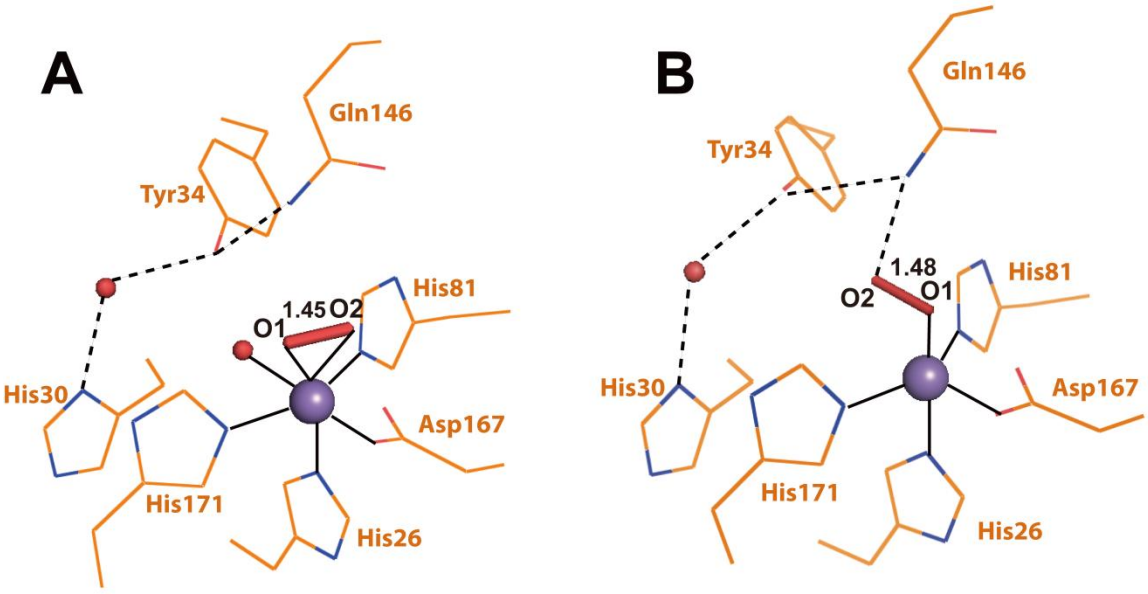

Figure S4.8. Mn-peroxo complexes in the crystal structure of cyrotrapped peroxide-soaked *Ec*MnSOD (PDB code: 3K9S). (A) A side-on Mn-peroxo complex (chain C); (B) An end-on Mn-peroxo complex (chain B). The graphic was generated using the PyMOL Molecular Graphics System. Manganese ions are shown as purple spheres. The peroxyl group and solvent molecules are shown as red sticks and red spheres, respectively. Coordination and hydrogen bonds are indicated as solid and dashed lines, respectively.

References

1. Abreu, I. A., and Cabelli, D. E. (2010) Superoxide dismutases-a review of the metal-associated mechanistic variations. *Biochim Biophys Acta* **1804**, 263-274

2. Zheng, J., Domsic, J. F., Cabelli, D., McKenna, R., and Silverman, D. N. (2007) Structural and kinetic study of differences between human and Escherichia coli manganese superoxide dismutases. *Biochemistry* **46**, 14830-14837

3. Abreu, I. A., Hearn, A., An, H., Nick, H. S., Silverman, D. N., and Cabelli, D. E. (2008) The kinetic mechanism of manganese-containing superoxide dismutase from Deinococcus radiodurans: a specialized enzyme for the elimination of high superoxide concentrations. *Biochemistry* **47**, 2350-2356

4. Barnese, K., Sheng, Y., Stich, T. A., Gralla, E. B., Britt, R. D., Cabelli, D. E., and Valentine, J. S. (2010) Investigation of the highly active manganese superoxide dismutase from Saccharomyces cerevisiae. *J Am Chem Soc* **132**, 12525-12527

5. Sheng, Y., Stich, T. A., Barnese, K., Gralla, E. B., Cascio, D., Britt, R. D., Cabelli, D. E., and Valentine, J. S. (2011) Comparison of two yeast MnSODs: mitochondrial Saccharomyces cerevisiae versus cytosolic Candida albicans. *J Am Chem Soc* **133**, 20878-20889

6. Jackson, T. A., and Brunold, T. C. (2004) Combined spectroscopic/computational studies on Fe- and Mn-dependent superoxide dismutases: insights into second-sphere tuning of active site properties. *Acc Chem Res* **37**, 461-470

7. Jackson, T. A., Karapetian, A., Miller, A. F., and Brunold, T. C. (2005) Probing the geometric and electronic structures of the low-temperature azide adduct and the product-inhibited form of oxidized manganese superoxide dismutase. *Biochemistry* **44**, 1504-1520

8. Maliekal, J., Karapetian, A., Vance, C., Yikilmaz, E., Wu, Q., Jackson, T., Brunold, T. C., Spiro, T. G., and Miller, A. F. (2002) Comparison and contrasts between the active site PKs of Mn-superoxide dismutase and those of Fe-superoxide dismutase. *J Am Chem Soc* **124**, 15064-15075

9. Guan, Y., Hickey, M. J., Borgstahl, G. E., Hallewell, R. A., Lepock, J. R., O'Connor, D., Hsieh, Y., Nick, H. S., Silverman, D. N., and Tainer, J. A. (1998) Crystal structure of Y34F mutant human mitochondrial manganese superoxide dismutase and the functional role of tyrosine 34. *Biochemistry* **37**, 4722-4730

10. Whittaker, M. M., and Whittaker, J. W. (1997) Mutagenesis of a proton linkage pathway in Escherichia coli manganese superoxide dismutase. *Biochemistry* **36**, 8923-8931

11. Edwards, R. A., Whittaker, M. M., Whittaker, J. W., Baker, E. N., and Jameson, G. B. (2001) Outer sphere mutations perturb metal reactivity in manganese superoxide dismutase. *Biochemistry* **40**, 15-27

12. Perry, J. J., Hearn, A. S., Cabelli, D. E., Nick, H. S., Tainer, J. A., and Silverman, D. N. (2009) Contribution of human manganese superoxide dismutase tyrosine 34 to structure and catalysis. *Biochemistry* **48**, 3417-3424

13. Schwarz, H., BNL Pulse Radiolysis Program. Brookhaven National Laboratory

14. Walter, T. S., Meier, C., Assenberg, R., Au, K. F., Ren, J. S., Verma, A., Nettleship, J. E., Owens, R. J., Stuart, D. I., and Grimes, J. M. (2006) Lysine methylation as a routine rescue strategy for protein crystallization. *Structure* **14**, 1617-1622

15. Sutherland, M. W., and Learmonth, B. A. (1997) The tetrazolium dyes MTS and XTT provide new quantitative assays for superoxide and superoxide dismutase. *Free Radic Res* **27**, 283-289

16. Otwinowski, Z., and Minor, W. (1997) Processing of X-ray diffraction data collected in oscillation mode. *Method Enzymol* **276**, 307-326

17. Mccoy, A. J., Grosse-Kunstleve, R. W., Adams, P. D., Winn, M. D., Storoni, L. C., and Read, R. J. (2007) Phaser crystallographic software. *J Appl Crystallogr* **40**, 658-674

18. Emsley, P., and Cowtan, K. (2004) Coot: model-building tools for molecular graphics. *Acta Crystallogr D* **60**, 2126-2132

19. Murshudov, G. N., Vagin, A. A., and Dodson, E. J. (1997) Refinement of macromolecular structures by the maximum-likelihood method. *Acta Crystallogr D* **53**, 240-255

20. Adams, P. D., Grosse-Kunstleve, R. W., Hung, L. W., Ioerger, T. R., McCoy, A. J., Moriarty, N. W., Read, R. J., Sacchettini, J. C., Sauter, N. K., and Terwilliger, T. C. (2002) PHENIX: building new software for automated crystallographic structure determination. *Acta Crystallogr D Biol Crystallogr* **58**, 1948-1954

21. Perry, J. J., Shin, D. S., Getzoff, E. D., and Tainer, J. A. (2010) The structural biochemistry of the superoxide dismutases. *Biochim Biophys Acta* **1804**, 245-262

22. Whittaker, J. W., and Whittaker, M. M. (1991) Active-Site Spectral Studies on Manganese Superoxide-Dismutase. *J Am Chem Soc* **113**, 5528-5540

23. Hsu, J. L., Hsieh, Y., Tu, C., O'Connor, D., Nick, H. S., and Silverman, D. N. (1996) Catalytic properties of human manganese superoxide dismutase. *J Biol Chem* **271**, 17687-17691

24. Lah, M. S., Dixon, M. M., Pattridge, K. A., Stallings, W. C., Fee, J. A., and Ludwig, M. L. (1995) Structure-function in Escherichia coli iron superoxide dismutase: comparisons with the manganese enzyme from Thermus thermophilus. *Biochemistry* **34**, 1646-1660

25. Rulisek, L., Jensen, K. P., Lundgren, K., and Ryde, U. (2006) The reaction mechanism of iron and manganese superoxide dismutases studied by theoretical calculations. *J Comput Chem* **27**, 1398-1414

26. Abreu, I. A., Rodriguez, J. A., and Cabelli, D. E. (2005) Theoretical studies of manganese and iron superoxide dismutases: superoxide binding and superoxide oxidation. *J Phys Chem B* **109**, 24502-24509

27. Borgstahl, G. E. O., Pokross, M., Chehab, R., Sekher, A., and Snell, E. H. (2000) Cryo-trapping the six-coordinate, distorted-octahedral active site of manganese superoxide dismutase. *Journal of Molecular Biology* **296**, 951-959

28. Carrasco, R., Morgenstern-Badarau, I., and Cano, J. (2007) Two proton-one electron coupled transfer in iron and manganese superoxide dismutases: A density functional study. *Inorg Chim Acta* **360**, 91-101

29. Porta, J., Vahedi-Faridi, A., and Borgstahl, G. E. (2010) Structural analysis of peroxide-soaked MnSOD crystals reveals side-on binding of peroxide to active-site manganese. *J Mol Biol* **399**, 377-384

30. Okamura, M. Y., Paddock, M. L., Graige, M. S., and Feher, G. (2000) Proton and electron transfer in bacterial reaction centers. *Biochim Biophys Acta* **1458**, 148-163

31. Chen, K., Hirst, J., Camba, R., Bonagura, C. A., Stout, C. D., Burgess, B. K., and Armstrong, F. A. (2000) Atomically defined mechanism for proton transfer to a buried redox centre in a protein. *Nature* **405**, 814-817

32. Campbell, K. A., Yikilmaz, E., Grant, C. V., Gregor, W., Miller, A. F., and Britt, R. D. (1999) Parallel polarization EPR characterization of the Mn(III) center of oxidized manganese superoxide dismutase. *J Am Chem Soc* **121**, 4714-4715

33. Miller, A. F., and Vance, C. K. (2001) Novel insights into the basis for Escherichia coli superoxide dismutase's metal ion specificity from Mn-substituted FeSOD and its very high E(m). *Biochemistry* **40**, 13079-13087

34. Yikilmaz, E., Porta, J., Grove, L. E., Vahedi-Faridi, A., Bronshteyn, Y., Brunold, T. C., Borgstahl, G. E. O., and Miller, A. F. (2007) How can a single second sphere amino acid substitution cause reduction midpoint potential changes of hundreds of millivolts? *J Am Chem Soc* **129**, 9927-9940

35. Jackson, T. A., Xie, J., Yikilmaz, E., Miller, A. F., and Brunold, T. C. (2002) Spectroscopic and computational studies on iron and manganese superoxide dismutases: nature of the chemical events associated with active-site pKs. *J Am Chem Soc* **124**, 10833-10845

36. Darensbourg, D. J., and Frantz, E. B. (2008) Studies of the carbon dioxide and epoxide coupling reaction in the presence of fluorinated manganese(III) acacen complexes: kinetics of epoxide ring-opening. *Inorg Chem* **47**, 4977-4987

37. Geiger, R. A., Chattopadhyay, S., Day, V. W., and Jackson, T. A. (2010) A series of peroxomanganese(III) complexes supported by tetradentate aminopyridyl ligands: detailed spectroscopic and computational studies. *J Am Chem Soc* **132**, 2821-2831

38. Vance, C. K., and Miller, A. F. (1998) Simple proposal that can explain the inactivity of metal-substituted superoxide dismutases. *J Am Chem Soc* **120**, 461-467

Chapter 5

Tetramerization in Yeast MnSOD and its Functional Significance

(This chapter is in preparation for submission to *the Journal of Biological Chemistry*)

Introduction

Manganese-containing superoxide dismutase (SOD) is an important intracellular antioxidant enzyme. It defends biological systems by catalyzing the disproportionation of superoxide (O_2^-) into dioxygen and hydrogen peroxide (H_2O_2). It is either a homodimer or a homotetramer with a monomer size of ~23,000 Da. The enzymes located in eukaryote mitochondria (human (1), *Saccharomyces cerevisiae* (2), *Caenorhabditis elegans* (3), *Aspergillus fumigates* (4)) were found to be homotetramers, while MnSODs isolated from bacteria (*Thermus thermophilus* (5), *Escherichia coli* (6), *Deinococcus radiodurans* (7)) are homodimers. In all MnSODs, each MnSOD subunit is composed of two domains, a predominantly α-helical N-terminal domain and a mixed α/β C-terminal domain. The Mn ion is coordinated by four strictly conserved residues, two from the N-terminal domain and two from the C-terminal domain, and one solvent molecule.

Assembly into oligomers has been proposed to confer several potential various advantages on proteins, including greater folding efficiency, high stability, specific morphological functions, amenability to allosteric regulation, and greater error control in synthesis (8-10). Tetrameric MnSODs are dimers of dimers, which display dihedral symmetry (D_2). However, being a tetramer does not grant MnSOD higher catalytic efficiencies. Dimeric bacterial MnSODs and tetrameric human MnSOD have similar efficiencies when O_2^- levels are low, and bacterial MnSODs are faster than human MnSOD when O_2^- levels are high (11,12).

In the budding yeast *S. cerevisiae*, there is only one MnSOD, and it is located to the mitochondria (13,14). The closely related yeast *Candida albicans* has two MnSODs, one in the mitochondria and the other in the cytosol (MnSODc) (15). *Sc*MnSOD and *Ca*MnSODc share 70% sequence similarity and are similar in enzyme kinetics, spectroscopy and redox chemistry (16).

However, *Ca*MnSODc was found to exist as a dimer in solution but as a tetramer when it was crystallized, while *Sc*MnSOD was found to be a tetramer under all conditions (16). Because *Sc*MnSOD and *Ca*MnSODc have most biochemical and biophysical properties in common and their dimer interface shares >90% similarity, they together provide an ideal system for elucidating the significance of the differences in MnSOD quaternary structures.

Scheme 5.1. Alignment of MnSOD C-terminal Sequence. Conserved residues and unconserved residues at the dimer interface are highlighted in bold and shadowed in gray, respectively. The RP-mutations in *Sc*MnSOD and *Ca*MnSODc are highlighted in black.

E. coli	GL**DVWEH**AY**YL**KFQ**N**RRPDYIKEFWN**V**VNWDEAAARFAAKK----	206
D. radiodurans	GV**DVWEH**AY**YL**NYQ**N**RRPDYLAAFWN**V**VNWDEVSKRYAAAK----	211
D. melanogaster	GI**DVWEH**AY**YL**QYK**N**VRPSYVEAIWD**I**ANWDDISCRFQEAKKLGC	206
C. elegans	GI**DVWEH**AY**YL**QYK**N**VRPDYVHAIWK**I**ANWKNISERFANARQ---	200
mouse	GI**DVWEH**AY**YL**QYK**N**VRPDYLKAIWN**V**INWENVTERYTACKK---	205
human	GI**DVWEH**AY**YL**QYK**N**VRPDYLKAIWN**V**INWENVTERYMACKK---	205
*Sc*MnSOD	AI**DAWEH**AY**YL**QYQ**N**KKADYFKAIWN**V**VNWKEASRRFDAGKI---	207
*Ca*MnSODc	AI**DAWEH**AY**YL**QYQ**N**VKLDYFKAIWN**V**INWAEAESRYSA------	206
RP-*Sc*MnSOD	AI**DAWEH**AY**YL**QYQ**N**KRPDYFKAIWN**V**VNWKEASRRFDAGKI---	207
RP-*Ca*MnSODc	AI**DAWEH**AY**YL**QYQ**N**VRPDYFKAIWN**V**INWAEAESRYSA------	206

The dimer interface plays a crucial role in maintaining MnSOD activity. Most MnSODs have a conserved arginine close to the strictly conserved DXWEHXXYL motif, while in yeast MnSODs it is a lysine (Scheme 5.1, Lys182 in *Sc*MnSOD and Lys184 in *Ca*MnSODc). This lysine in yeast MnSOD and arginine in all other MnSODs, has been proposed to be critical for the catalytic activity of MnSODs (17). A more recent study suggested that the substitution of this lysine causes loss of stability in *Sc*MnSOD (18).

The side chain of the lysine in yeast MnSODs has a different conformation compared to that of the arginine in MnSODs from other organisms. This difference derives from the residue

next to the lysine, which is an alanine or leucine in *Sc*MnSOD and *Ca*MnSODc, respectively, and a proline in all other MnSODs. To investigate whether modification of the dimer interface has the same effects on tetrameric and dimeric MnSOD, we engineered the two yeast MnSODs by mutating the lysine to arginine and changing the residue next to the lysine to proline (K182R, A183P *Sc*MnSOD and K184R, L185P *Ca*MnSODc) (Scheme 5.1), so that the conformation of the arginine is identical to that in other MnSODs. Here, we report the crystal structures of wild-type and RP-mutant (here we call the mutant proteins RP-mutant MnSOD or RP-MnSOD) yeast MnSODs and their biochemical and biophysical properties. We also discuss how the tetramer structure reinforces the dimer interface of MnSOD.

---

*We call the mutant proteins RP-mutant MnSOD or RP-MnSOD.

Materials and Methods

Samples. *Ec*MnSOD was purchased from a commercial source (Sigma-Aldrich). The protein was resuspended in 25 mM potassium phosphate (pH 7.4), washed with 1 mM EDTA in the same phosphate buffer for several times, and then purified through a G200 size exclusion column.

Construction of Plasimid for Expression of RP-mutant ScMnSOD and CaMnSODc. Site-directed mutagenesis (19) was carried out on an overexpression vector (YEp352-*Sc*MnSOD) containing the *URA*3 selectable marker and a 2-kb genomic *Bam*HI fragment containing the gene for *Sc*MnSOD. The primers 5'-CAGTACCAAAACAAG**AGACCC**GACTACTTCAAAGC-3' and 5'-GCTTTGAAGTAGTC**GGGTCT**CTTGTTTTGGTACTG-3' were used to create the cDNA for K182R, A183P *Sc*MnSOD.

The pVT102U-*Ca*MnSODc (with *URA3* and *AMP* marker) vector containing the complete coding sequence of *Ca*MnSODc was generously given by Prof. Bourbonnais (15). The primers 5'-CAAAATGTC**AGGCCT**GATTATTTCAAAGCAATTTGGAA-CGTG-3' and 5'-GAAATAATC**AGGCCT**GACATTTTGATATTGCAAGTAGTAC-GC-3' were used to create the cDNA for K184R, L185P *Ca*MnSODc.

The PCR products were transformed into *E. coli DH5α* strain and screened by ampicillin selection. The purified vectors were transformed into *S. cerevisiae sod2Δ* strain (EG110).

Expression and Purification of Wild-type and RP-mutant ScMnSOD and CaMnSODc. Yeast cells carrying Yep352-*Sc*MnSOD (wild type or mutant) were grown in YPEG media (1% yeast extract, 2% peptone, 3% glycerol, 2% ethanol, pH 4) supplemented with 0.5 mM Mn(II) sulfate at 30 ℃ to O.D. > 20. Yeast cells carrying pVT102U-*Ca*MnSODc (wild type or mutant) were grown in YPD (1% yeast extract, 2% peptone, 2% dextrose, pH 4) media supplemented with 0.5 mM Mn(II) sulfate at 30 ℃ to O.D. > 10. Cells were harvested by centrifugation at 12,000 × g for 10 min. Isolation of wild-type and RP-mutant *Sc*MnSOD and *Ca*MnSODc was performed as previously described (16).

Size Exclusion Chromatography. The mass weight of native proteins was determined by a HPLC (Agilent 1200 series) fitted with a size exclusion column (Tosoh Bioscience, TSK gel G2000SW) at a flow rate of 0.25–0.5 mL/min. The column was calibrated using five standards: bovine thyroglobulin (670 kDa), bovine γ-globulin (158 kDa), ovalbumin (44 kDa), horse myoglobin (17 kDa), and vitamin B12 (1.35 kDa).

HPLC-SEC measurements were used to determine the oligomer state of proteins. The equilibrium between dimers and monomers is shown as $D \Leftrightarrow 2M$ where D represents dimer and M represents monomer. The dimer dissociation constant (K_d) is calculated as

$$K_d = \frac{[M]^2}{[D]}$$

where [M] and [D] were calculated from area integrals of elution peaks (UV signal at 210 nm). The peak fitting was carried out in OriginPro 8.1 (OriginLab Corp.). The column buffer contained 10 mM potassium phosphate (pH 6.7). The protein concentration was varied from 10 μM to 200 nM.

Crystallization of Wild type and RP-mutant ScMnSOD and CaMnSODc. The crystallization of wild-type *Sc*MnSOD and *Ca*MnSODc was described before (16). Two conditions yielded protein crystals showing *Ca*MnSODc dimers in the structure. First, Native *Ca*MnSODc was crystallized by hanging-drop vapor diffusion at 4 ℃ against a solution of 0.2 M lithium sulfate and 0.1 M phosphate-citrate (pH 4.2) in 20% (w/v) polyethylene glycol 1,000 with a protein concentration of 7 mg/mL. Second**,** methylated *Ca*MnSODc was crystallized by hanging-drop vapor diffusion at 4 ℃ against a solution of 0.2 M sodium nitrate and 0.1 M bis-tris propane (pH 7.5) in 20% (w/v) polyethylene glycol 3,350 with a protein concentration of 7 mg/mL. The reductive methylation of lysine residues of *Ca*MnSODc was carried out using procedures described before.(20) All the free amino groups of lysine residues and N-terminal were methylated as confirmed by mass spectrometry (Figure S1-B). These two structures were not deposited to PDB bank, because they have clear breaks in the electron density in the N-terminal regions.

Reduction methylation of K182R, A183P *Sc*MnSOD was carried out as described previously (20), in order to improve the diffraction of protein crystals. All free amino groups of the lysine residues and the N-terminus were methylated as confirmed by mass spectrometry (Figure S5.1-A), and the activity of the native and methylated forms of RP-mutant *Sc*MnSOD was similar in SOD activity assay (21).

Methylated K182R, A183P *Sc*MnSOD was crystallized by hanging-drop vapor diffusion at 4 ℃ against a well solution of 0.1 M tri-ammonium citrate (pH 7) in 20% (w/v) polyethylene glycol 3,350 with a protein concentration of 7 mg/mL. Native K184R, L185P *Ca*MnSODc was crystallized by hanging-drop vapor diffusion at 4 ℃ against a solution of 2 M ammonium sulfate with a protein concentration of 7 mg/mL. The protein crystals were cryo-protected in mother liquor solution containing 30% glycerol and flash frozen in liquid nitrogen prior to data collection.

Crystallography: Data Collection and Refinement. All data were collected at 100K at the UCLA X-ray diffraction facility, using a Rigaku FRE+ generator and a Rigaku HTC detector. All data was processed using DENZO and SCALEPACK (22). The crystallography information for wild-type *Sc*MnSOD and *Ca*MnSODc was reported previously (16). RP-mutant *Sc*MnSOD and *Ca*MnSODc were phased by molecular replacement using wild-type *Sc*MnSOD (PDB code: 3LSU) and *Ca*MnSODc (PDB code: 3QVN), respectively. All the molecular replacement was done using PHASER (23). The models were built using COOT (24). All model refinements were performed using REFMAC (25) and PHENIX (26).

Analysis of interface contacts and estimation of changes in salvation energy were performed using the PISA server (PDBePISA Protein Interfaces, Surfaces and Assemblies (27)).

*Other crystallization conditions for wild-type CaMnSODc***.** Two conditions yielded wild-type *Ca*MnSODc protein crystals showing *Ca*MnSODc dimers in the structure. First, Native wild-type *Ca*MnSODc was crystallized by hanging-drop vapor diffusion at 4 ℃ against a solution of 0.2 M lithium sulfate and 0.1 M phosphate-citrate (pH 4.2) in 20% (w/v) polyethylene glycol 1,000 with a protein concentration of 7 mg/mL. Second**,** methylated wild-type *Ca*MnSODc was crystallized by hanging-drop vapor diffusion at 4 ℃ against a solution of 0.2 M sodium nitrate and 0.1 M bis-tris propane (pH 7.5) in 20% (w/v) polyethylene glycol 3,350 with a protein concentration of 7 mg/mL. The reductive methylation of lysine residues of *Ca*MnSODc was carried out using procedures described before (20). All the free amino groups of lysine residues and N-terminus were methylated as confirmed by mass spectrometry (Figure S5.1-B).

These two structures were not adopted, because their resolutions were lower than those that give *Ca*MnSODc tetramers.

Pulse radiolysis. Pulse radiolysis experiments were carried out using the 2 MeV Van de Graaff accelerator at Brookhaven National Laboratory. Upon irradiation of water with a pulse of energetic electrons, hydrated electrons (e_{aq}^-), hydroxyl radicals ($^{\bullet}OH$) and, in lesser yield, hydrogen atoms ($H^{\bullet}$) are the primary radicals produced. Superoxide radical is then generated in air-saturated aqueous solution containing sodium formate through the following reactions: $^{\bullet}OH + HCO_2^- \rightarrow H_2O + CO_2^{\bullet-}$, $O_2 + CO_2^{\bullet-} \rightarrow O_2^{\bullet-} + CO_2$, $e_{aq}^- + O_2 \rightarrow O_2^{\bullet-}$, $H + O_2 \rightarrow HO_2^{\bullet}$.

The experiments to measure catalytic rates involved following the decay of various concentrations of O_2^- at 260 nm using 1:1 to 1:50 ratios of [MnSOD]:[O_2^-]. First-order rate

constants were calculated by fitting the data using the Chemical Kinetics program in PRWIN (28).

The temperature deactivation measurements were performed by heating the pulse radiolysis cell holder to the desired temperature. The sample cell containing a protein solution was then inserted into the holder and allowed to equilibrate for 4 minutes prior to radiation of the sample solution.

All pulse radiolysis samples were prepared in 10 mM potassium phosphate, 10 mM sodium formate and 10 μM EDTA at 25 °C. All MnSOD concentrations were taken as the ICP-measured concentration of manganese in the sample. The pH of the buffer was adjusted using ultrapure (Baker Ultrex) sodium hydroxide and sulphuric acid as needed.

Differential Scanning Calorimetry (DSC). DSC scans were performed using a Nano II differential scanning calorimeter (Calorimetry Sciences Corp.). All buffers were degassed under vacuum and highly concentrated protein samples (~24 mg/mL) were diluted with degassed buffers to a concentration of 2 mg/mL (600 μL) right before the DSC run. All samples were run at a rate of 1 ℃/min under 4 atm of pressure. A buffer (25 mM potassium phosphate, pH 7.4) base line was run prior to the analysis of protein samples with the same heating/cooling rates. Baseline subtraction was performed, and some of the peaks were fitted to non-two-state reversible transitions using Origin 8.0 (Microcal).

The other peaks were fitted to two-state irreversible transitions, obeying pseudo-first-order kinetics (29). The temperature dependence of the kinetic constant *k* obeys the Arrhenius equation,

$$k = A\exp\left(\frac{-E}{RT}\right)$$

where A is the preexponential factor and E is the activation energy of transition. The apparent excess heat capacity $C_p(T)$ at a temperature T is given by Sánchez-Ruiz's methods as

$$C_p(T) = \left(\frac{\Delta HE}{RT^2}\right)\exp(u(T))\exp\left[-\exp(u(T))\right]$$

where $u(T) = \frac{E}{R}\left(\frac{1}{T_m} - \frac{1}{T}\right)$, T_m is the temperature at which C_p reaches its maximum value. DSC data were fitted to equation (6) using SigmaPlot 11.0 (Systat Software).

Miscellaneous Methods. Metal contents of the purified proteins were determined by ICP-MS (Agilent 7500 series). UV-visible absorption spectra were collected on a Shimadzu UV-2501 PC spectrophotometer.

Circular dichroism (CD) measurements were performed on a JASCO J-715 spectropolarimeter at room temperature. The GdHCl concentration was varied from 0 to 5 M while the protein concentration was held constant at 0.2 mg/mL. Protein samples were mixed with GdHCl stock solutions and incubated at room temperature for 15 min prior to the scan.

Mass weight of the protein subunit was determined by an electrospray ionization mass spectrometry (ESI-MS) either via a triple quadrupole instrument (API III, Applied Biosystems) or via a hybrid linear ion-trap mass spectrometer (LTQ, Thermo Electron). Mass spectra were processed and analyzed using MacSpec 3.3, Hypermass and BioMultiview 1.3.1 software for data obtained from API III, and ProMass for Xcalibur 2.8 for data obtained from LTQ.

Results

The N-terminal Helixes are Highly Disordered in Dimeric CaMnSODc. Wild-type *Sc*MnSOD and *Ca*MnSODc and their RP-mutant proteins were overexpressed and purified from *S. cerevisiae*, and their purities were confirmed by SDS-PAGE gel (Figure S5.2). To solve the mystery of why *Sc*MnSOD and *Ca*MnSODc share high sequence similarity while one is a tetramer and the other is a dimer in solution, we determined their crystal structures (16). The crystal structure further confirmed that *Sc*MnSOD is a homotetramer (Figure 5.1A). By contrast, the quaternary structure of *Ca*MnSODc varies with crystallization conditions; it is either a homotetramer (Figure 5.1B) or a homodimer (Figure 5.1D).

As in other tetrameric MnSODs, the N-terminus of both yeast MnSODs folds into a hairpin structure holding two long α-helixes (Figure 5.1C), which are much shorter in dimeric MnSODs from bacteria (Figure S5.3-B). The N-terminal helical hairpins are considerably longer in *Sc*MnSOD than in any previously characterized tetrameric MnSOD (Figure 5.1C, S5.3-A). This feature renders *Sc*MnSOD a much larger tetramer interface of >1400 $Å^2$, as compared to 800–1000 $Å^2$ in other MnSOD tetramers (human, *A. fumigates*, and *C. elegans*) (Table S5.1).

A surprising observation for *Ca*MnSODc is that the crystal structures showing *Ca*MnSODc as tetramers have well-defined electron density throughout the entire sequence, while those showing *Ca*MnSODc as dimers have clear electron density breaks in the region encompassing residues 45, 51–69, 89–97, and 156–163. While residues 89–97 and 156–163 belong to loop regions, which are expected to possess high structural disorder, residues 51–69 belong to the N-terminal helical region (Figure 5.1D), which holds two highly ordered α-helixes in the well-ordered structure of *Ca*MnSODc (Figure 5.1C). 20 residues (45, 51–69) from the N-

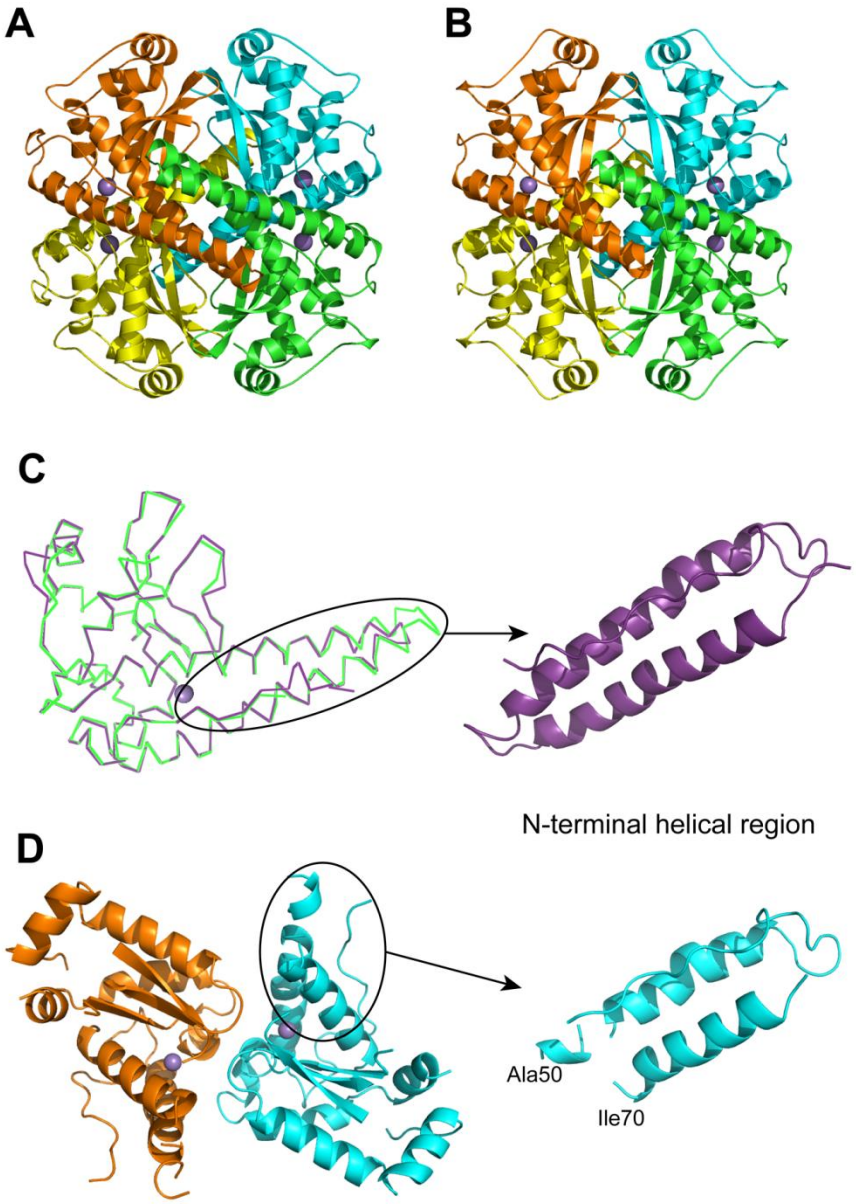

Figure 5.1. The N-terminal helixes are highly disordered, when *Ca*MnSODc is in the dimeric form. (A and B) Ribbon diagram of *Sc*MnSOD (A) and *Ca*MnSODc (B) tetramer. The four subunits are colored in: A, yellow; B, orange; C, green; D, cyan. Manganese ions are indicated as purple spheres. (C) Superimposition of the subunit of *Ca*MnSODc (purple) in the tetrameric form over that of *Sc*MnSOD (green). The N-terminal helical region (residues 1–91) of *Ca*MnSODc is enlarged on the right. (D) Ribbon diagram of *Ca*MnSODc in the dimeric form in the crystal lattice. The two subunits in the asymmetric unit are colored in: A, blue; B, yellow. Manganese ions are indicated as purple spheres. The N-terminal helical region (residues 1–88) is enlarged on the right.

terminal region are missing electron densities; therefore, the structure coordinates for a large fraction of the hairpin remote form the active site could not be built (Figure 5.1D). These findings suggest that the α-helix-based hairpin structure is highly disordered, when *Ca*MnSODc is dimeric.

To investigate structural changes caused by the substitutions of Lys182 (Lys184) and Ala183 (Leu185), we solved the structures of the two RP-mutant proteins. The tetrameric assemblies of wild-type and RP-mutant yeast MnSODs closely resemble each other (Figure S5.4). Superimpositions of all backbone atoms of the mutant subunit onto those of the wild type subunit give root-mean-square deviations (RMSD) of 0.15 Å and 0.34 Å for *Sc*MnSOD and *Ca*MnSODc, respectively, suggesting that the substitutions cause greater structural perturbation to *Ca*MnSODc than to *Sc*MnSOD.

RP-CaMnSODc is Susceptible to Dimer Dissociation. The oligomeric states of the native proteins were investigated by HPLC-SEC. When the protein concentration was varied from 10 μM to 200 nM, wild-type and the RP-*Sc*MnSOD both eluted solely as a tetramer (Figure 5.2A), while wild-type *Ca*MnSODc eluted solely as a dimer (Figure 5.2B). By contrast, the elution profiles of RP-*Ca*MnSODc revealed two peaks corresponding to dimeric and monomeric forms when the protein concentration was below 1 μM (Figure 5.2B). At 200 nM RP-*Ca*MnSODc eluted solely as a monomer (Figure 5.2B). Based on the dimer-monomer equilibrium (Experimental Procedures), K_d of RP-*Ca*MnSODc was determined to be 2.0 ± 0.1 μM, with details of the calculation shown in Table S5.2.

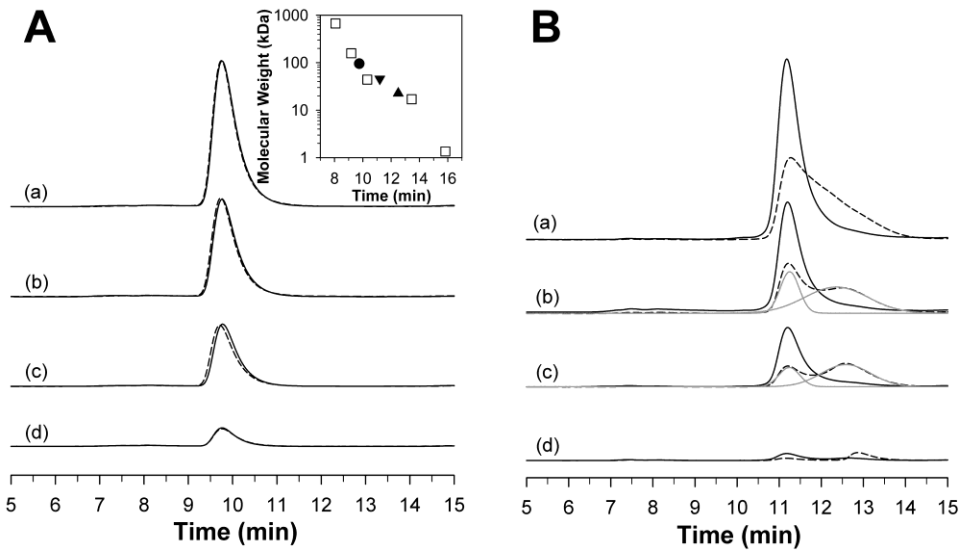

Figure 5.2. Oligomer state of wild-type and RP-mutant *Sc*MnSOD and *Ca*MnSODc. (A) HPLC-SEC profiles of wild-type (solid line) and K182R, A183P (dashed line) *Sc*MnSOD. Inset: The plot of the molecular weight of the five standards (square), *Sc*MnSOD tetramer (circle) and *Ca*MnSODc dimer (triangle down) and monomer (triangle up) versus their retention time. The column was calibrated using five standards: 1) bovine thyroglobulin (670 kDa), 2) bovine γ-globulin (158 kDa), 3) ovalbumin (44 kDa), 4) horse myoglobin (17 kDa), and 5) Vitamin B12 (1.35 kDa). (B) HPLC-SEC profiles of wild-type (solid lines) and K184R, L185P (dashed lines) *Ca*MnSODc. Deconvoluted peaks are shown as grey lines. The protein concentration relative to monomer was 1 μM (a), 750 nM (b), 500 nM (c) and 200 nM (d). The elution buffer contained 10 mM potassium phosphate (pH 6.7).

RP-Mutant Yeast MnSODs Catalyze the Dismutation of O_2^- like Wild-type Enzymes. The substitutions at the dimer interface make yeast RP-MnSODs structurally closer to human MnSOD. To explore whether these substitutions affect the catalysis of yeast MnSODs, wild-type and RP-mutant yeast enzymes were pulsed with various concentrations of O_2^-, and their dismutation efficiencies were compared. At neutral pH and room temperature, the wild types and the mutant proteins have similar kinetics. When $[O_2^-]$ was high relative to enzyme concentration ($[O_2^-]$:[MnSOD] = 41), the decay curves for O_2^- disappearance catalyzed by wild-type or RP-mutant yeast MnSODs were superimposable (Figure S5.4), suggesting that the mutant proteins resemble the wild types in displaying low degrees of product inhibition (16,30).

MnSOD enzymatic activity is represented by the first-order rate constant calculated at low O_2^- doses ($[O_2^-]$:MnSOD = 1 – 3). We previously showed that inactivation by pH is significantly more prominent in yeast MnSODs than in human MnSOD, p*K* of 8.5 and 10.5, respectively (16). Here, although both yeast MnSODs were engineered to imitate human MnSOD, neither of the mutant proteins gain higher resistance to pH compared to the wild types (Figure 5.3).

The profile of RP-*Sc*MnSOD activity as a function of pH closely resembles that of wild-type *Sc*MnSOD (Figure 5.3). The same mutations on *Ca*MnSODc, however, resulted in an enzyme even more sensitive to pH, with the p*K* decreasing from ~8.5 in the wild type to ~ 8 in the mutant protein (Figure 5.3). Loss of activity at high pH is reversible in wild-type yeast enzymes as well as in RP-*Sc*MnSOD, with a restoration of ~50% of their original activity (Figure 5.3). By contrast, when the pH of the sample solution was adjusted from basic (≥ 9) to neutral, no restoration of activity was observed for RP-mutant *Ca*MnSODc (Figure 5.3).

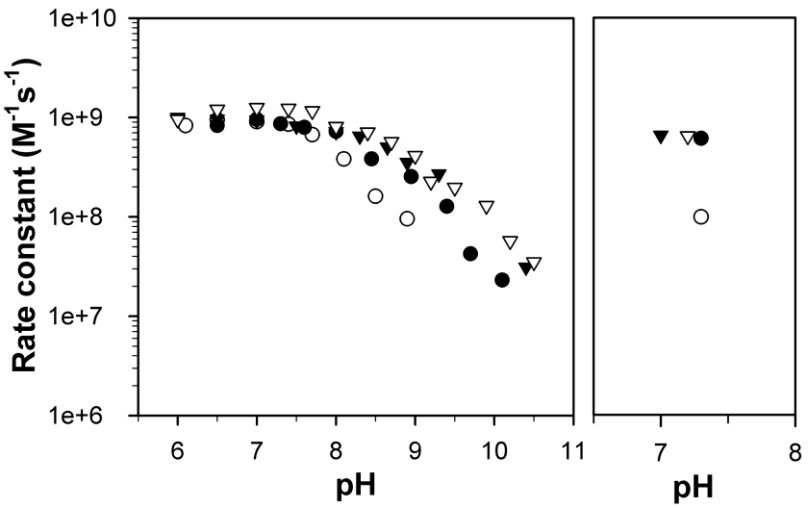

Figure 5.3. RP-*Ca*MnSODc is more subject to inactivation by pH than the wild type. (left) Rate constants as a function of pH determined by fitting the disappearance of low doses of O_2^- ($[O_2^-]$:[MnSOD] from 1 – 3) to first-order processes. The enzymes were wild-type *Sc*MnSOD (solid triangle), K182R, A183P *Sc*MnSOD (hollow triangle), wild-type *Ca*MnSODc (solid circle) and K184R, L185P *Ca*MnSODc (hollow circle). (right) Rate constants of sample solutions with the pH adjusted from 9–9.5 to neutral. The sample solutions contained 1 μM (in Mn) MnSOD in 10 mM potassium phosphate (pH 7), 10 mM sodium formate and 10 μM EDTA.

RP-CaMnSODc is Inactivated by Heat, while RP-ScMnSOD is not. Yeast MnSODs, when treated with heat, do not exhibit loss of function. *Sc*MnSOD retained its activity at full scale up to 75 ℃, the highest temperature allowed in pulse radiolysis measurements. *Ca*MnSODc, with a much lower thermostability than *Sc*MnSOD (see below), retained its full activity as long as the enzyme stayed folded in solution. Protein aggregation was noticeable from decreased initial voltage V0, which quantifies the maximum intensity of UV light that can penetrate the sample cell. Melting of as-isolated *Ca*MnSODc occurs at 50 ℃ (see below), and the enzyme stayed fully active up to 49 ℃ (Figure 5.4).

By contrast, the reactivity of *Ec*MnSOD decreased by ~100 fold after the sample solution was allowed to equilibrate to 68 ℃ (Figure 5.4, see method). Because V0 stayed the same before and after the sample solution was equilibrated, the loss of activity in *Ec*MnSOD resulted from dramatic inactivation by heat rather than aggregation of the enzyme.

The substitutions of Lys182 (Lys184) and Ala 183 (Leu185) at the dimer interface affect the temperature profile of *Sc*MnSOD and *Ca*MnSODc differently. Similar to wild-type *Sc*MnSOD, RP-*Sc*MnSOD retained full activity up to 73 ℃ (Figure 5.4). RP-*Ca*MnSODc, however, differs from the wild type but resembles bacterial MnSODs in terms of inactivation by heat. When RP-*Ca*MnSODc was heated at 41 ℃, a loss of ~70% activity was observed (Figure 5.4). RP-*Ca*MnSODc started aggregating at ~46 ℃ (see below), and stayed soluble in solution at 41 ℃.

Wild-type and RP-mutant CaMnSODc are More Susceptible to Denaturant-Induced Protein Unfolding than Wild-type and RP-mutant ScMnSOD. In order to understand the impact of the quaternary structure and the dimer interface on MnSOD stability, we used CD

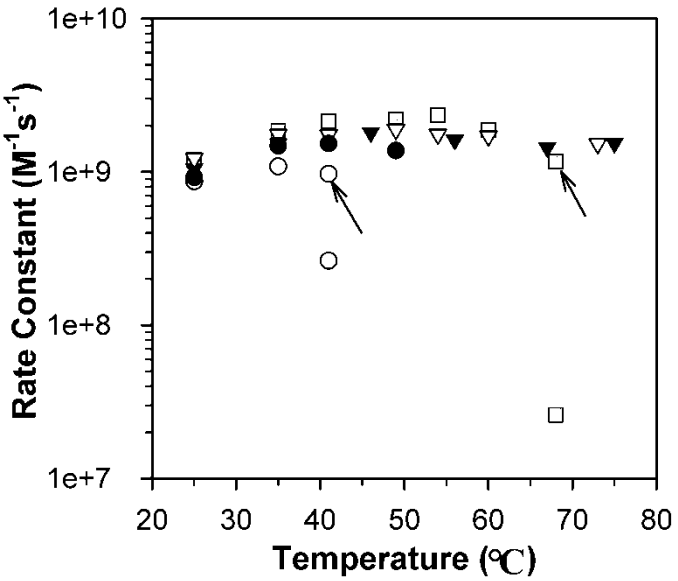

Figure 5.4. RP-*Ca*MnSODc is inactivation by heat like *Ec*MnSOD. The enzymes were *Ec*MnSOD (grey rectangle), wild-type *Sc*MnSOD (solid triangle), wild-type *Ca*MnSODc (solid circle), K182R, A183P *Sc*MnSOD (hollow triangle) and K184R, L185P *Ca*MnSODc (hollow circle). The data points indicated with an arrow were obtained before the sample solution reached the desired temperature. All other data points were obtained after the sample solution was equilibrated to the desired temperature. The sample solutions contained 1 μM (in Mn) MnSOD in 10 mM potassium phosphate (pH 7), 10 mM sodium formate and 10 μM EDTA.

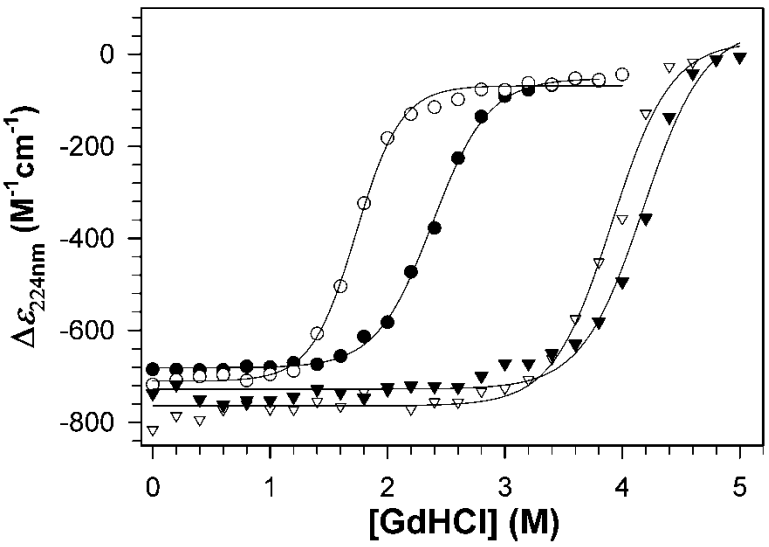

Figure 5.5. RP-*Ca*MnSODc is more subject to GdHCl-induced unfolding than the wild type. The molar CD at 224 nm was used to monitor changes in α-helical structure content as a function of [GdHCl]. The enzymes were wild-type *Ca*MnSODc (solid circles), K184R, L185P *Ca*MnSODc (hollow circle), wild-type *Sc*MnSOD (solid triangle) and K182R, A183P *Sc*MnSOD (hollow triangle). The sample solutions contained 0.2 mg/mL (monomer concentration) MnSOD in 25 mM potassium phosphate (pH 7.4).

spectroscopy to monitor the denaturant-induced unfolding transitions of wild-type and RP-mutant yeast MnSODs. The molar CD at 224 nm was used to monitor changes in α-helical structure content as a function of [GdHCl] (Figure S5.6). In these experimental conditions, *Sc*MnSOD is a tetramer while *Ca*MnSODc is a dimer. The sharp decrease in helical structure content occurred at ~3.4 M GdHCl in *Sc*MnSOD and ~1.6 M GdHCl in *Ca*MnSODc (Figure 5.5). The unfolding of RP-*Ca*MnSODc occurred at ~1.2 M GdHCl and proceeded considerably faster (p*K* ~ 1.7 M) than that of wild-type *Ca*MnSODc (p*K* ~2.4 M) (Figure 5.5). By contrast, the unfolding profiles of wild-type and RP-mutant *Sc*MnSOD are comparable to each other with a p*K* of ~4.2 and ~4.0 M, respectively (Figure 5.5).

Wild-type and RP-mutant CaMnSODc are Significantly Less Thermal Stable than Wild-type and RP-mutant ScMnSOD. To investigate the impact of the quaternary structure and the substitutions at the dimer interface on MnSOD thermostability, we monitored the unfolding transitions of wild-type and RP-mutant yeast MnSODs by DSC (Experimental Procedures). The wild-type and mutant proteins are both partially loaded with Mn and rest predominantly in the reduced (2+) state. The DSC profile of as-isolated *Sc*MnSOD showed a single transition at 91 ℃, corresponding to one irreversible process (Figure 5.6A). This suggests cooperativity in the melting of apo and metallated subunits in *Sc*MnSOD. By contrast, three endotherms with much lower T_ms were observed upon heat treatment of as-isolated *Ca*MnSODc, assigned as Therm 1, 2 and 3 (Figure 5.6B, Table 5.1). Therm 1 corresponded to the cooperative melting of apo- and Mn^{2+}-containing *Ca*MnSODc. Due to the fact that Therm 3 was missing in the thermal stability profile of reduced *Ca*MnSODc (Figure 5.6B), it correlated with the aggregation of Mn^{3+}-containing *Ca*MnSODc. Therm 2 likely resulted from a small portion (~5%) of Fe-containing SOD.

Table 5.1. Thermodynamic Parameters for Unfolding of Yeast MnSODs

	Component Number	T_m (℃)	ΔH^a (kcal/mol)
As-isolated *Sc*MnSOD[b]		91.0	705
Oxidized *Sc*MnSOD[b]		91.5	659
As-isolated *Ca*MnSODc[c]	1	60.3	431
	2	66.0	36
	3	69.7	33
Reduced *Ca*MnSODc[c]	1	60.9	353
	2	64.5	13
Oxidized *Ca*MnSODc[c]	4	66.5	325
	3	72.9	254
As-isolated K182R, A183P *Sc*MnSOD[c]		84.4	563
As-isolated K184R, L185P *Ca*MnSODc[c]	1	57.4	288
	2	62.3	216
	3	66.2	12

[a] ΔH are given per mole of tetramer or dimer. [b] The peaks of the DSC profile were deconvoluted using an irreversible two-state model. [c] The peaks of the DSC profile were deconvoluted using a reversible non-two-state model.

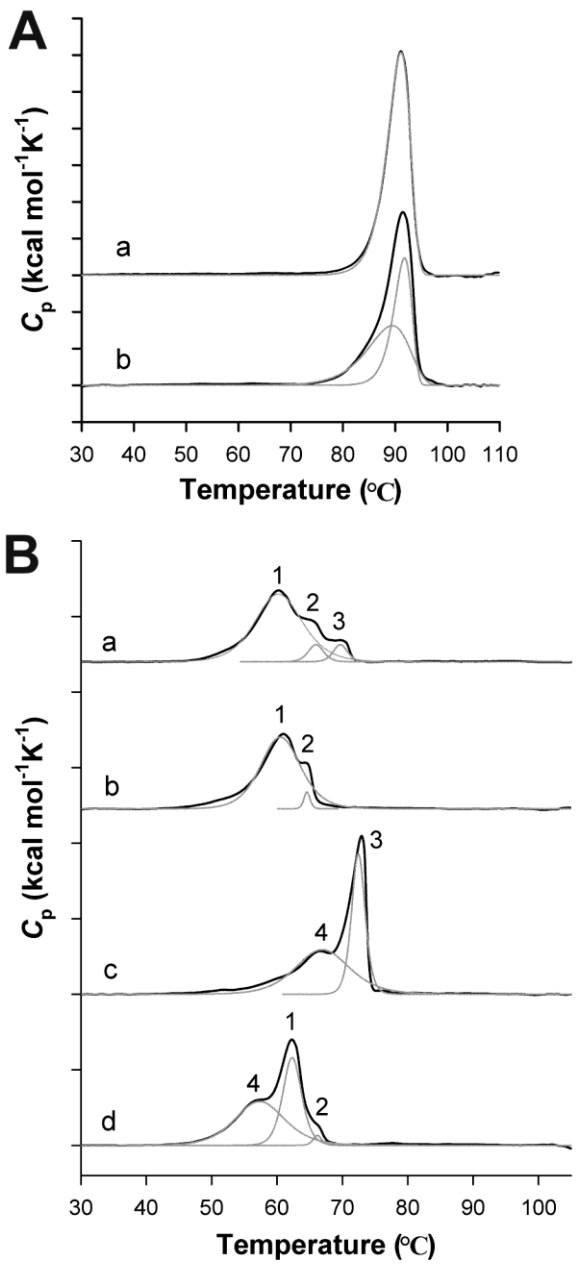

Figure 5.6. Thermostability of wild-type and RP-mutant *Sc*MnSOD and *Ca*MnSODc. (A) Unfolding transitions (black) of as-isolated (a) and oxidized (b) *Sc*MnSOD and as-isolated K182R, A183P *Sc*MnSOD (c). (B) Unfolding transitions (black) of as-isolated (a), reduced (b) and oxidized (c) *Ca*MnSODc and as-isolated K184R, L185P *Ca*MnSODc (d). The components (gray) were deconvoluted using a two-state irreversible model for wild-type *Sc*MnSOD and a non-two-state reversible model for RP-*Sc*MnSOD, and wild-type and RP-*Ca*MnSODc. Reduced or oxidized enzymes were prepared by adding sodium hyposulfite or potassium permanganate to the sample solution prior to the DSC scan.

The stability profile of yeast MnSODs is affected by the protein oxidation state. Chemically oxidized (3+) *Ca*MnSODc gave a wide therm (4) prior to the emergence of Therm 3. To explore the origin of Therm 4, oxidized *Ca*MnSODc was heated at 65 ℃ for 20 min, and the metal content of the resulting supernatant was determined by ICP-MS. Because ~90% of the proteins in the supernatant contained Mn, Therm 4 was likely associated with the aggregation of apo subunits in oxidized *Ca*MnSODc. The separation of apoprotein endotherm from holoprotein endotherm was subtle in oxidized *Sc*MnSOD, although its main transition occurred at a lower temperature (~75 ℃) than the as-isolated protein (~80 ℃) and could well be deconvoluted to two irreversible processes (Figure 5.6A).

The as-isolated RP-*Sc*MnSOD gave a single endotherm like the wild-type enzyme, with the T_m lowered to 84 ℃ (Figure 5.6A). By contrast, the DSC profile of the as-isolated RP-*Ca*MnSODc deviated more dramatically from that of wild-type *Ca*MnSODc, in that the transition of the melting of apo-RP-*Ca*MnSODc occurred at a lower T_m (57 ℃) and was separated from that of the melting of holo-RP-*Ca*MnSODc (Figure 5.6B). The mutant protein maintained the two therms at 62 and 66 ℃, corresponding to the aggregation of Mn^{2+}-containing and Fe-substituted *Ca*MnSODc, respectively (Figure 5.6B, Table 5.1).

Discussion

Tetramerization Stabilizes the Highly Disordered N-terminus of Dimeric CaMnSODc–The two yeast MnSODs, one from *S. cerevisiae* mitochondria and the other from *C. albicans* cytosol, share ~70% sequence similarity. *Sc*MnSOD is always a homotetramer like human MnSOD (2,16). To our surprise, *Ca*MnSODc is a dimer in solution (Figure 5.2B), and it

is either a dimer or a tetramer when crystallized (Figure 5.1B, 5.1D). The only other experiment that suggests *Ca*MnSODc as a tetrameric enzyme is analytical ultracentrifugation, when performed at 30,000 rpm for 24 hrs with a protein concentration of 2 mg/mL (data not shown). Tetrameric MnSODs are in equilibrium between dimers and tetramers, and this kind of equilibrium is usually dependent on factors such as ionic strength, temperature, pH, and concentration of denaturant (8,10). Our results suggest that the tetramer-dimer equilibrium lies toward dimers in *Ca*MnSODc, while it lies toward tetramers in other tetrameric MnSODs.

The monomer of *Ca*MnSODc and *Sc*MnSOD resembles each other, in terms of the well-defined N-terminal α-helix-based hairpin (Figure 5.1C), which has been proposed a critical role in tetramer formation (1,5). However, electron density breaks were observed in the crystal structures of *Ca*MnSODc in the dimeric form. They occur in two loop regions, and most dramatically in the N-terminal helixes, where 20 residues lack electron density (Figure 5.1D). These findings lead to the conclusion that the highly disordered N-terminal region hinders *Ca*MnSODc from forming a tetramer in solution.

The N-terminal helixes are expected to be largely solvent accessible when *Ca*MnSODc is dimeric; upon tetramer formation, these helixes are extensively involved in noncovalent interactions. Examination of the crystal structure of *Ca*MnSODc in the tetrameric form reveals the stabilizing effects of the noncovalent forces at the tetramer interface. Like in *Sc*MnSOD, the tetramerization domain in *Ca*MnSODc contains several hydrogen bonds, between the two N-terminal helical hairpins, and between one helical hairpin and the loop connecting β2 and β3 (Figure 5.7). These hydrogen-bonding interactions, together with hydrophobic and salt bridge interactions, reduce the structural disorder of the N-terminus in tetrameric *Ca*MnSODc, and

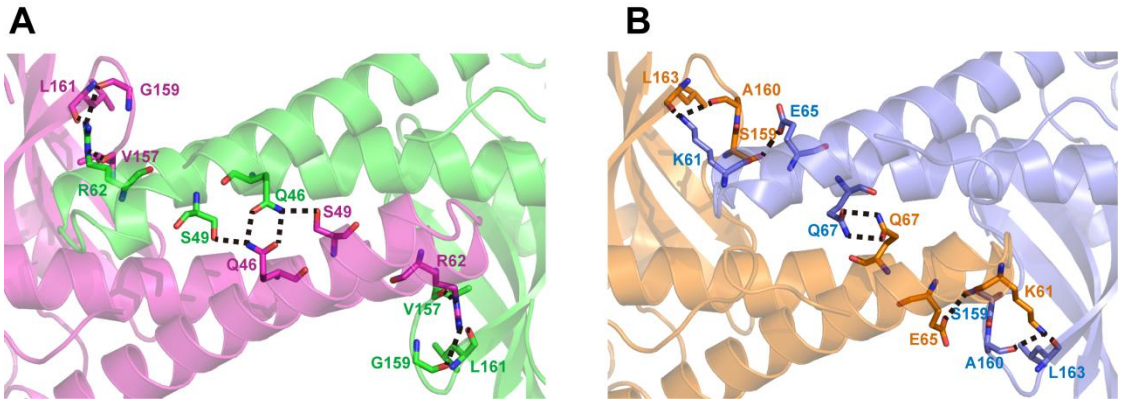

Figure 5.7. Tetramer interface of wild-type *Sc*MnSOD (A) and *Ca*MnSODc (B) with residues that form hydrogen bonds shown in sticks. The asymmetric unit of *Sc*MnSOD has four chains, and here Chain B and C are colored in green and pink, respectively. The asymmetric unit of *Ca*MnSODc has one chain (blue); the other chain (orange) in the figure was generated by a C_2 symmetry operation. Hydrogen bonds across the tetramer interface are shown in dashes.

likely restrain the overall mobility of the polypeptide, leading to the well-defined electron density throughout the entire sequence.

Because the helical hairpins contain two of the active site ligands, it was believed that the tetramer interface played a role in stabilizing the helical hairpins, and that only tetrameric enzymes would be active and stable (1). The I58T (a tetramer interface residue) variant of human MnSOD has a much shorter half life than the wild type at increased temperatures (31). Numerous other dihedral tetrameric proteins and enzymes, such as malic enzyme, chaperone SecB and the RUNX1/ETO fusion protein, display impaired function, when dissociating into dimers or monomers (32-34). *Ca*MnSODc in our kinetics studies was in the dimeric form, since the compositions of the sample solutions in these studies were comparable to those used for determining the oligomer state of *Ca*MnSODc (Figure 5.2B, Experimental Procedures). However, the catalytic properties of dimeric *Ca*MnSODc resemble those of tetrameric *Sc*MnSOD without any indication of activity loss (16). If the subunit of human and *E. coli* MnSOD is assigned as "tetrameric" and "dimeric" subunit, respectively, our studies presents the first MnSOD, which is comprised of "tetrameric" subunits while its functionality is not dependent on tetramer formation. This phenomenon has also been reported for Aristolochene Synthase from *Aspergillus terreus*, which functions as a dimer in solution, but is capable for tetramerization at high enzyme concentrations (35).

It is doubtful that tetrameric *Ca*MnSODc significantly surpasses dimeric *Ca*MnSODc in reactivity, because the latter is already near diffusion-controlled (16). Dimeric *Ca*MnSODc could be the active form that functions in vivo. However, since it is difficult to compare the composition of *C. albicans* cytosol to the in vitro conditions, we are unable to elucidate the in vivo structure of *Ca*MnSODc.

Functional Significance of the Tetramer Structure–Although *Ca*MnSODc is indistinguishable from *Sc*MnSOD in terms of enzyme kinetics, spectroscopy and redox properties (16), dimeric *Ca*MnSODc is considerably less stable than tetrameric *Sc*MnSOD. Compared to tetrameric *Sc*MnSOD, the unfolding of dimeric *Ca*MnSODc occurs at a much lower level of denaturant (GdHCl) (Figure 5), and the T_m of the main components of dimeric *Ca*MnSODc is lower by 30 ℃. These facts suggest the important role of the tetramerization domain in enhancing the MnSOD enzyme's resistance against unfolding in harsh environments.

Several studies suggest a significant role for the dimer interface in both catalysis and stability of MnSOD. Replacement of Glu170 in *Ec*MnSOD, which spans the dimer interface and forms the double glutamate bridge, results in dissociation of the dimer, complete loss of catalytic activity, and a change in metal specificity (36). Substitutions at Glu162 in human MnSOD, the counterpart of Glu170 in *Ec*MnSOD, reduce the catalytic activity to 5–25% of that of the wild-type enzyme (37). The Y166F mutant human MnSOD shows a significant decrease in catalytic activity and a major unfolding transition at a lower T_m (38). Replacements of Phe66 at the dimer interface of human MnSOD reduces the degree of product inhibition in the human enzyme and makes it resemble *Ec*MnSOD (12).

Here, two residues (Lys182 and Ala183 in *Sc*MnSOD, Lys184 and Leu185 in *Ca*MnSODc) were substituted at the dimer interface of the two yeast MnSODs. We show here that the two RP-mutant proteins resemble their wild-type enzymes in terms of SOD activity at room temperature and neutral pH (Figure S5.5), and the role of the two residues appear to be related to protein stability.

Even though one is a tetramer and the other is a dimer in solution, *Sc*MnSOD and *Ca*MnSODc, have >90% sequence similarity at the dimer interface and share most biochemical and biophysical characteristics. The mutations do not result in considerable perturbation in the subunit structure of the two yeast enzymes (Figure S5.4). Nevertheless, the dimer dissociation constant, K_d, which is too low to measure in wild-type *Ca*MnSODc, significantly increases to 2.0 ± 0.1 μM in the mutant protein. RP-mutant *Ca*MnSODc also becomes more sensitive to high pH than the wild type, and this inactivation by increased pH becomes completely irreversible (Figure 5.3). In contrast to wild-type *Ca*MnSODc, the RP-mutant protein exhibits loss of activity at high temperatures (Figure 5.4), and it is more subject to unfolding by GdHCl, with the p*K* of the unfolding profile decreasing by 0.7 M (Figure 5.5).

The destabilization of the dimer interface in RP-mutant *Ca*MnSODc is also suggested by the DSC protein stability data. The oxidized form of *Ca*MnSODc has a higher thermal stability than the reduced form (Figure 5.6B). The dependence of protein stability on the oxidation state was also reported in *Ec*MnSOD, because the enzyme has a larger affinity for Mn^{3+} (39). Based on the DSC data in Figure 5.6B and Table 1, the molar energy required for aggregation of each enzyme species in wild-type *Ca*MnSODc scales as Mn^{3+}-containing *Ca*MnSODc > Fe-substituted *Ca*MnSODc > Mn^{2+}-containing *Ca*MnSODc ~ apo subunits. Since as-isolated wild-type and RP-mutant *Ca*MnSODc contain ~0.6 and ~0.5 Mn per monomer, respectively, each *Ca*MnSODc dimer contains one metal ion. As the 1Mn-*Ca*MnSODc dimer is heated, the apo subunits melt at 57–60 ℃ (Table 1). The remaining manganese-bound subunits then self-associate to create the 2Mn-*Ca*MnSODc dimer, the melting of which occurs at 65–73 ℃, depending on the oxidation state of the manganese (Table 1). This phenomenon has been reported for another type of SOD, copper-zinc SOD loaded with one or two zinc ions (40). In

RP-*Ca*MnSODc, the molar energy order changes to Fe-substituted *Ca*MnSODc > Mn^{2+}-containing *Ca*MnSODc > apo subunits (Figure 5.6B, Table 1). The modifications of the dimer interface lower the energy threshold for dimer dissociation, and thus make aggregation of apo subunits occur more readily in the mutant *Ca*MnSODc.

By contrast, the same residue substitutions at the dimer interface have much milder effects on tetrameric *Sc*MnSOD, although wild-type *Sc*MnSOD and *Ca*MnSODc are similar in many ways (16). RP-mutant *Sc*MnSOD closely resembles the wild type in crystal structure, oligomer state, and resistance to pH, heat and denaturant (Figure 5.2–5.5, S5.4). The only sign of destabilization is the slightly lower thermal stability displayed by the mutant protein relative to the wild type (Figure 5.6A).

The tetramer interface has been reported to contribute to the thermal and pH-dependent stability of numerous dihedral tetrameric enzymes, including malate hydrogenase and serine hydroxymethyltransferase (41-43). Specifically in tetrameric MnSODs, each side of the protein is encircled by one of the two 4-helix bundles at opposite ends of the dimer, which acts as a clamp, holding the dimers in place. In addition to the contribution to protein stability, our results here suggest that the dimer interface, which is critical for MnSOD activity, is strongly reinforced through tetramer formation.

Comparison of *Sc*MnSOD to *Ec*MnSOD, which is a dimer, also suggests the reinforcement of the dimer interface in the former. Levy *et al.* reported recently that the disassembly of protein homooligomers usually leads to stable subcomplexes in which the larger interface is maintained (44). In the case of *Sc*MnSOD, because the buried surface area at the tetramer interface (>1400 $Å^2$) is much larger than that at the dimer interface (>950 $Å^2$) (Table

S2), the dimer interface is expected to dissociate first. The oxidized form of *Ec*MnSOD, which melts at 89.5 ℃ (39), resembles *Sc*MnSOD (T_m = 91.0 ℃, Table 1) in terms of thermostability. The solvation energy ($\Delta^i G$) at the dimer interface is higher for *Ec*MnSOD (-11.9 kcal/mol) than for *Sc*MnSOD (-7.8 kcal/mol) (Table S2), suggesting that dimerization is more favorable in *Ec*MnSOD. Nevertheless, *Ec*MnSOD is completely inactivated at <70 ℃, while *Sc*MnSOD stays fully active at 75 ℃, the highest temperature allowed in the kinetics measurements (Figure 5.4). The deactivation of *Ec*MnSOD at high temperatures likely results from dissociation of the dimer structure, which does not occur in *Sc*MnSOD under the same conditions, due to the stabilizing effects of the tetramer structure.

In conclusion, the tetramer-dimer equilibrium of *Ca*MnSODc lies toward dimers, although its subunit contains the well-defined N-terminal helical hairpin as in other tetrameric MnSODs. This finding is likely due to the highly disordered N-terminal region in *Ca*MnSODc, while its functionality under physiological conditions does not rely on tetramerization. The significance of the tetramer structure lies in the stabilization of protein assembly against harsh environments (heat and denaturant). More importantly, we found that the tetramer structure strongly reinforces the dimer interface. As the dimer interface is critical for MnSOD activity, the reinforcement of the dimer interface through tetramerization could be one of the reasons for MnSOD being tetramers in higher organisms.

A

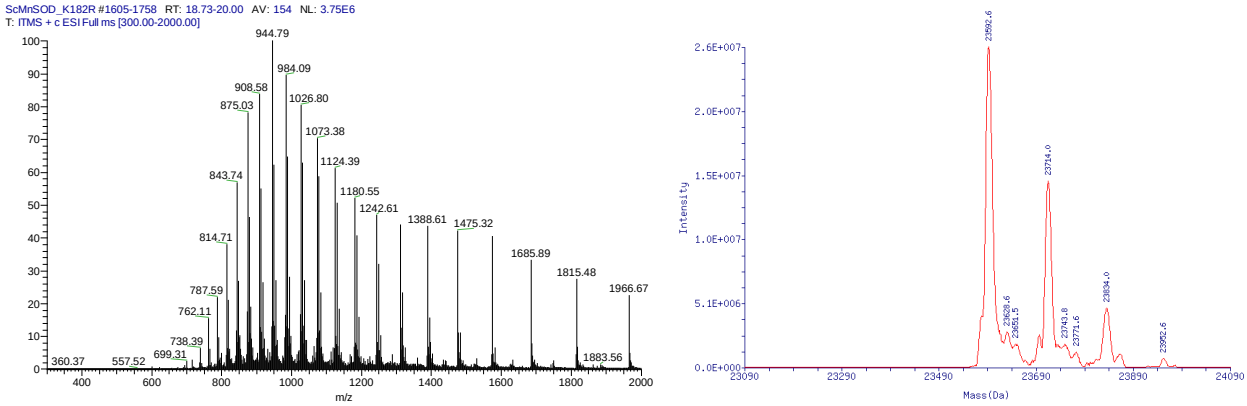

B

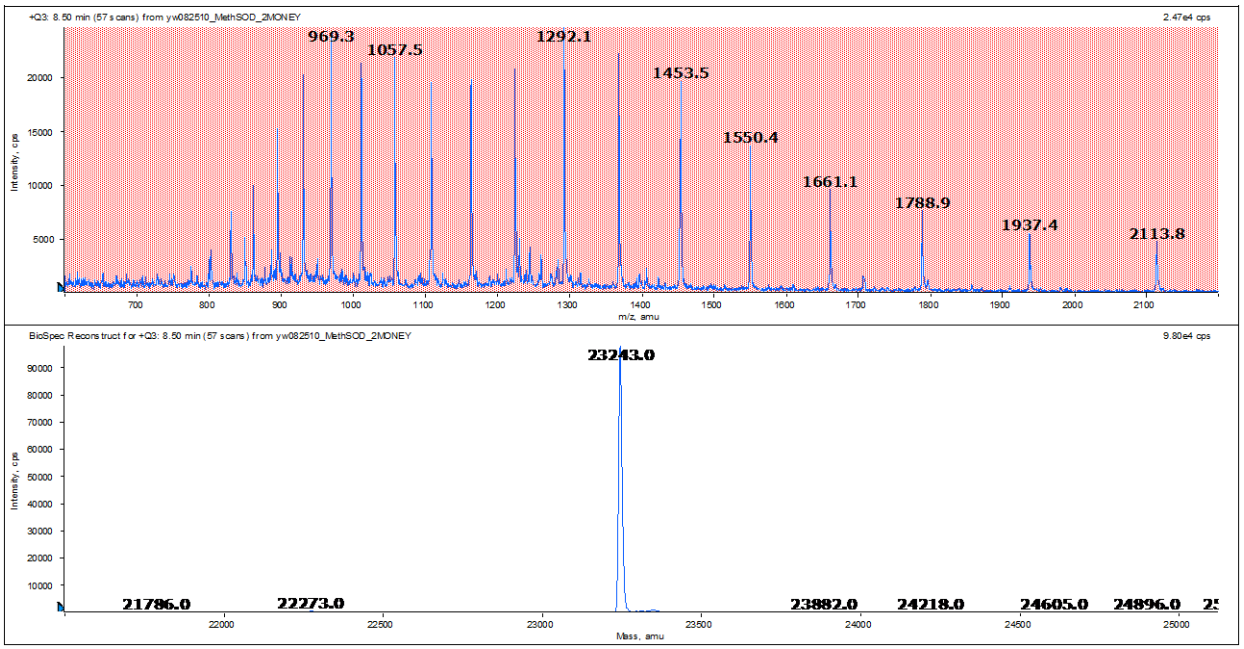

Figure S5.1. Electrospray-ionization mass spectra of methylated RP-mutant *Sc*MnSOD (A) and wild-type *Ca*MnSODc (B) and their reconstructed mass distribution profiles. Ordinate units of intensity are arbitrary and the abscissa units of average molecular mass are in Daltons. The theoretical mass weight of methylated RP-*Sc*MnSOD and wild-type *Ca*MnSODc is 23,589 and 23,239 Da, respectively.

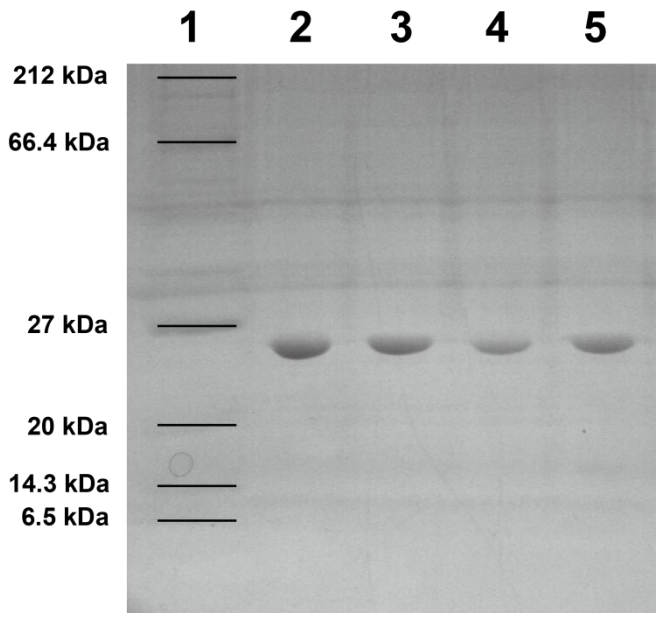

Figure S5.2. SDS-PAGE analysis of the purity of wild-type and RP-mutant *Sc*MnSOD and *Ca*MnSODc: 1) protein ladder (NEB # p7702s); 2) purified wild-type *Sc*MnSOD, 3) K182R, A183P *Sc*MnSOD, 4) wild-type *Ca*MnSODc, and 5) K184R, L185P *Ca*MnSODc.

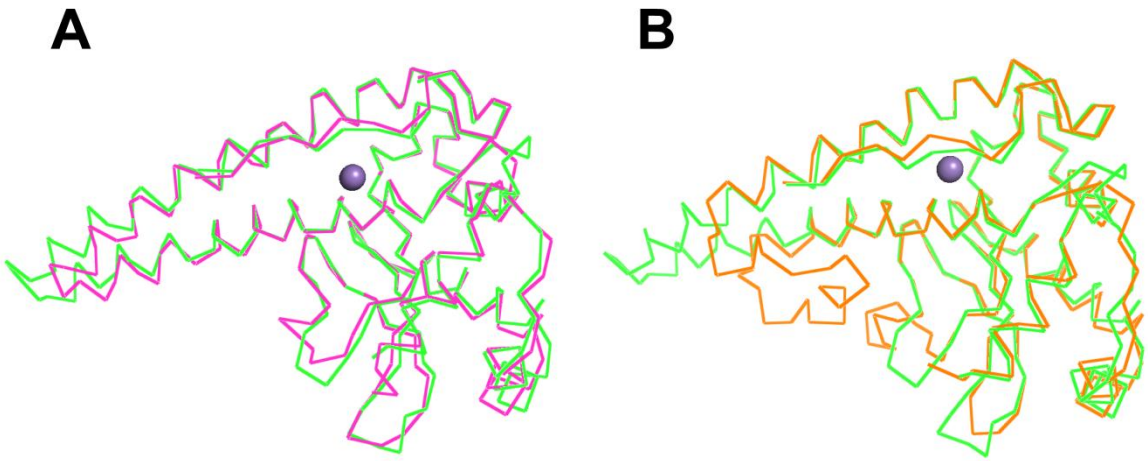

Figure S5.3. Superimposition of the subunit of *Sc*MnSOD (green) over that of human (pink) and *E. coli* (orange) MnSOD. The two subunits are colored in: A, green; B, cyan.

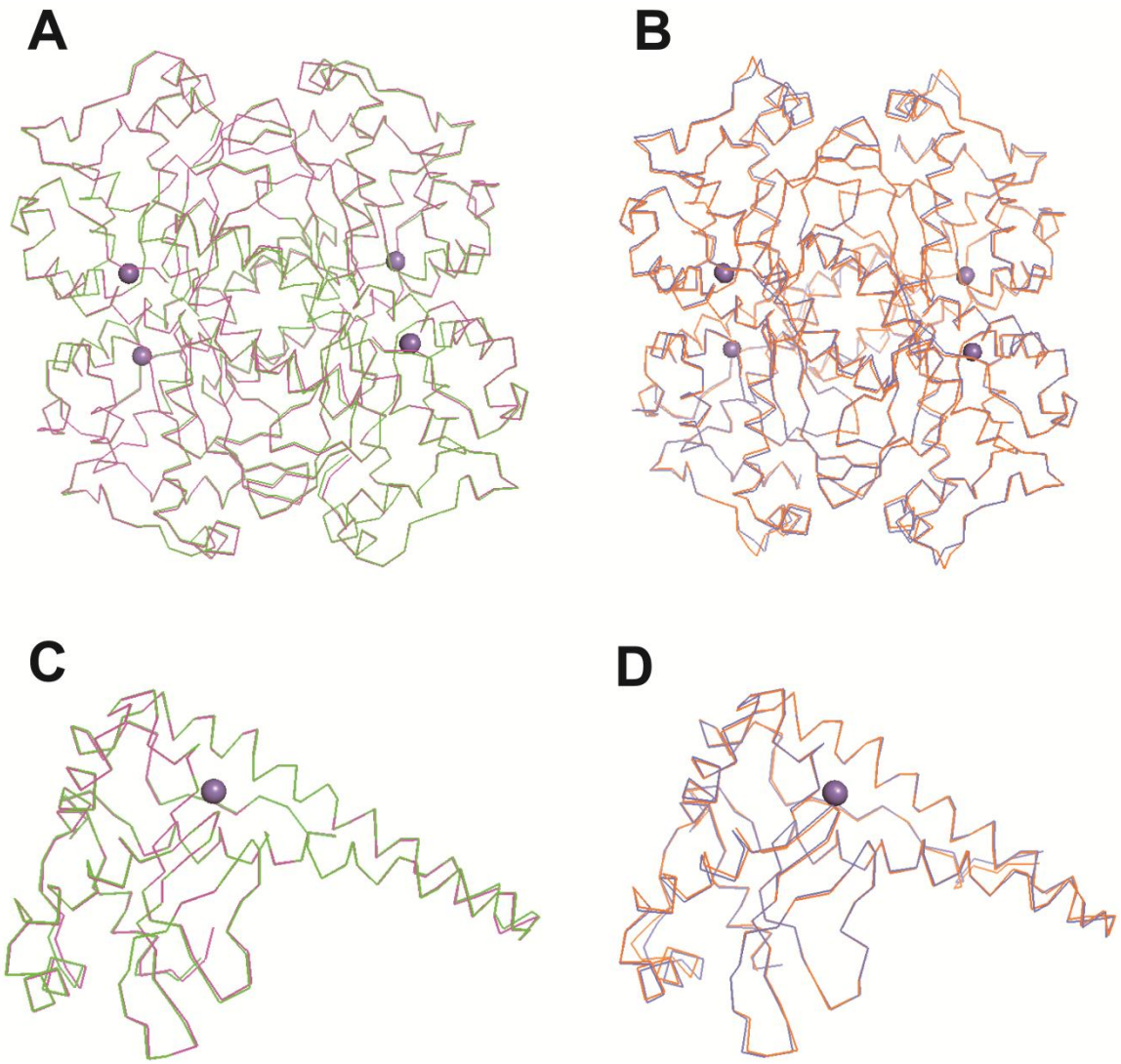

Figure S5.4. Comparison of crystal structures between wild-type yeast MnSODs and their RP-mutant proteins. (A and B). Superimposition of the tetramer of K182R, A183P *Sc*MnSOD (pink) and K184R, L185P *Ca*MnSODc (blue) onto that of wild-type *Sc*MnSOD (green) and *Ca*MnSODc (orange), respectively. (C and D). Superimposition of the monomer of K182R, A183P *Sc*MnSOD (pink) and K184R, L185P *Ca*MnSODc (blue) onto that of wild-type *Sc*MnSOD (green) and *Ca*MnSODc (orange), respectively. Manganese atoms are shown as purple spheres.

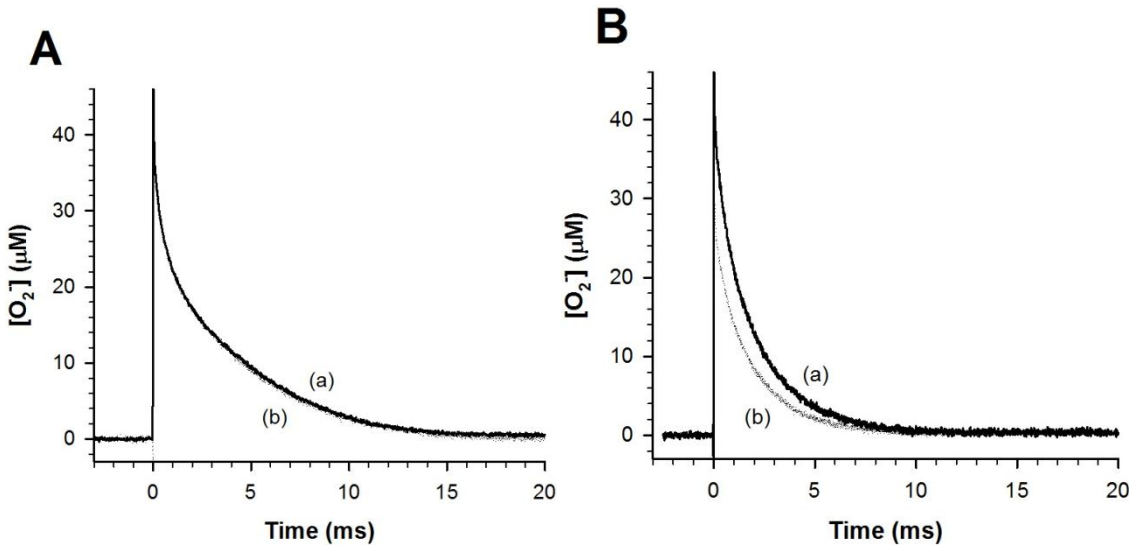

Figure S5.5. Decay of 43 μM O_2^- catalyzed by (A) wild-type *Sc*MnSOD (solid, a), K182R, A183P *Sc*MnSOD (dotted, b), (B) wild-type *Ca*MnSODc (solid, a) and K184R, L185P *Ca*MnSODc (dotted, b). The sample for pulse radiolysis contains 10 mM phosphate (pH 7), 10 mM sodium formate and 10 μM EDTA.

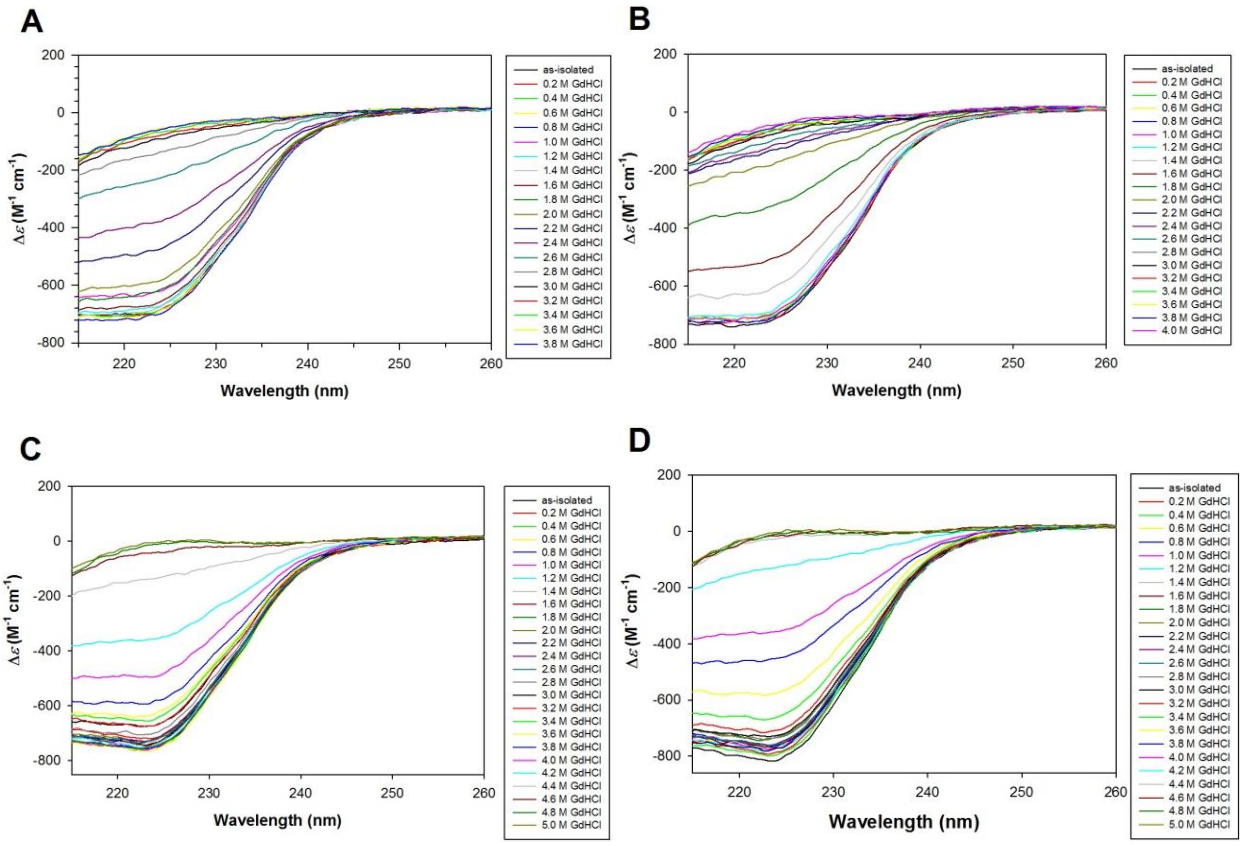

Figure S5.6. CD spectra of wild-type *Ca*MnSODc (A), K184R, L185P *Ca*MnSODc (B), wild-type *Sc*MnSOD (C) and K182R, A183P *Sc*MnSOD (D) at increased concentrations of GdHCl. The solutions contained 25 mM potassium phosphate (pH 7.4). The measurements were carried out at room temperature.

Table S5.1. Interactions of Subunits at Dimer and Tetramer Interfaces in MnSODs from Different Organisms

	*Sc*MnSOD	*Ca*MnSODc	human WT	*A. fumigatus*	*C. elegans*	*E. coli* WT	*T. Thermophilus*	*Drad* WT
Mn•••Mn (A/B, dimer, Å)	18.2 (0.04)	18.3	18.3	18.1 (0.1)	18.3	18.4 (0.01)	18.4	18.3
Mn•••Mn (A/C, tetramer, Å)	39.7 (0.2)	38.4	42.0	39.8 (0.1)	41.6			
Mn•••Mn (A/D, tetramer, Å)	38.7 (0.04)	38.4	41.0	38.7 (0.2)	40.3			
Dimer interface area (Å^2)	956	840	844	883	864	858	878	906
$\Delta^i G$ of dimer interface (kcal/mol)	-7.8	-6.2	-9.6	-8.8	-10.1	-11.9	-11.8	-10.5
Tetramer interface area (Å^2)	1417	1254	961	797	800			
$\Delta^i G$ of tetramer interface (kcal/mol)	-25.0	-12.6	-13.8	-14.9	-14.5			

Table S5.2. Calculation of K_d for K184R, L185P *Ca*MnSODc

Protein Concentration		750 nM		500 nM	
		1	2	1	2
Area integral (mAU×s)	dimer	1405	1519	777	755
	monomer	2939	3216	2114	1932
Concentration of Species (nM)	[D]	121.3	120.3	67.2	70.3
	[M]	507.5	509.4	365.6	359.5
K_d		2.1 μM	2.2 μM	2.0 μM	1.8 μM
Average K_d		2.0 ± 0.1 μM			

References

1. Borgstahl, G. E., Parge, H. E., Hickey, M. J., Beyer, W. F., Jr., Hallewell, R. A., and Tainer, J. A. (1992) The structure of human mitochondrial manganese superoxide dismutase reveals a novel tetrameric interface of two 4-helix bundles. *Cell* **71**, 107-118

2. Ravindranath, S. D., and Fridovich, I. (1975) Isolation and characterization of a manganese-containing superoxide dismutase from yeast. *J Biol Chem* **250**, 6107-6112

3. Trinh, C. H., Hunter, T., Stewart, E. E., Phillips, S. E., and Hunter, G. J. (2008) Purification, crystallization and X-ray structures of the two manganese superoxide dismutases from Caenorhabditis elegans. *Acta Crystallogr Sect F Struct Biol Cryst Commun* **64**, 1110-1114

4. Fluckiger, S., Mittl, P. R., Scapozza, L., Fijten, H., Folkers, G., Grutter, M. G., Blaser, K., and Crameri, R. (2002) Comparison of the crystal structures of the human manganese superoxide dismutase and the homologous Aspergillus fumigatus allergen at 2-A resolution. *J Immunol* **168**, 1267-1272

5. Wagner, U. G., Pattridge, K. A., Ludwig, M. L., Stallings, W. C., Werber, M. M., Oefner, C., Frolow, F., and Sussman, J. L. (1993) Comparison of the crystal structures of genetically engineered human manganese superoxide dismutase and manganese superoxide dismutase from Thermus thermophilus: differences in dimer-dimer interaction. *Protein Sci* **2**, 814-825

6. Edwards, R. A., Baker, H. M., Whittaker, M. M., Whittaker, J. W., Jameson, G. B., and Baker, E. N. (1998) Crystal structure of Escherichia coli manganese superoxide dismutase at 2.1-angstrom resolution. *J Biol Inorg Chem* **3**, 161-171

7. Abreu, I. A., Hearn, A., An, H., Nick, H. S., Silverman, D. N., and Cabelli, D. E. (2008) The kinetic mechanism of manganese-containing superoxide dismutase from Deinococcus radiodurans: a specialized enzyme for the elimination of high superoxide concentrations. *Biochemistry* **47**, 2350-2356

8. Goodsell, D. S., and Olson, A. J. (2000) Structural symmetry and protein function. *Annu Rev Biophys Biomol Struct* **29**, 105-153

9. Andre, I., Strauss, C. E., Kaplan, D. B., Bradley, P., and Baker, D. (2008) Emergence of symmetry in homooligomeric biological assemblies. *Proc Natl Acad Sci U S A* **105**, 16148-16152

10. Ali, M. H., and Imperiali, B. (2005) Protein oligomerization: how and why. *Bioorg Med Chem* **13**, 5013-5020

11. Abreu, I. A., and Cabelli, D. E. (2010) Superoxide dismutases-a review of the metal-associated mechanistic variations. *Biochim Biophys Acta* **1804**, 263-274

12. Zheng, J., Domsic, J. F., Cabelli, D., McKenna, R., and Silverman, D. N. (2007) Structural and kinetic study of differences between human and Escherichia coli manganese superoxide dismutases. *Biochemistry* **46**, 14830-14837

13. Luk, E., Carroll, M., Baker, M., and Culotta, V. C. (2003) Manganese activation of superoxide dismutase 2 in Saccharomyces cerevisiae requires MTM1, a member of the mitochondrial carrier family. *Proc Natl Acad Sci U S A* **100**, 10353-10357

14. Luk, E., Yang, M., Jensen, L. T., Bourbonnais, Y., and Culotta, V. C. (2005) Manganese activation of superoxide dismutase 2 in the mitochondria of Saccharomyces cerevisiae. *J Biol Chem* **280**, 22715-22720

15. Lamarre, C., LeMay, J. D., Deslauriers, N., and Bourbonnais, Y. (2001) Candida albicans expresses an unusual cytoplasmic manganese-containing superoxide dismutase (SOD3 gene product) upon the entry and during the stationary phase. *J Biol Chem* **276**, 43784-43791

16. Sheng, Y., Stich, T. A., Barnese, K., Gralla, E. B., Cascio, D., Britt, R. D., Cabelli, D. E., and Valentine, J. S. (2011) Comparison of two yeast MnSODs: mitochondrial Saccharomyces cerevisiae versus cytosolic Candida albicans. *J Am Chem Soc* **133**, 20878-20889

17. Borders, C. L., Chain, V. W. F., and Bjerrum, M. J. (1991) The Positive Charge at Position-189 Is Essential for the Catalytic Activity of Iron-Containing and Manganese-Containing Superoxide Dismutases. *Free Radical Res Com* **12-3**, 279-285

18. Borders, C. L., Jr., Bjerrum, M. J., Schirmer, M. A., and Oliver, S. G. (1998) Characterization of recombinant Saccharomyces cerevisiae manganese-containing superoxide dismutase and its H30A and K170R mutants expressed in Escherichia coli. *Biochemistry* **37**, 11323-11331

19. Ho, S. N., Hunt, H. D., Horton, R. M., Pullen, J. K., and Pease, L. R. (1989) Site-Directed Mutagenesis by Overlap Extension Using the Polymerase Chain-Reaction. *Gene* **77**, 51-59

20. Walter, T. S., Meier, C., Assenberg, R., Au, K. F., Ren, J. S., Verma, A., Nettleship, J. E., Owens, R. J., Stuart, D. I., and Grimes, J. M. (2006) Lysine methylation as a routine rescue strategy for protein crystallization. *Structure* **14**, 1617-1622

21. Sutherland, M. W., and Learmonth, B. A. (1997) The tetrazolium dyes MTS and XTT provide new quantitative assays for superoxide and superoxide dismutase. *Free Radic Res* **27**, 283-289

22. Otwinowski, Z., and Minor, W. (1997) Processing of X-ray diffraction data collected in oscillation mode. *Method Enzymol* **276**, 307-326

23. Mccoy, A. J., Grosse-Kunstleve, R. W., Adams, P. D., Winn, M. D., Storoni, L. C., and Read, R. J. (2007) Phaser crystallographic software. *J Appl Crystallogr* **40**, 658-674

24. Emsley, P., and Cowtan, K. (2004) Coot: model-building tools for molecular graphics. *Acta Crystallogr D* **60**, 2126-2132

25. Murshudov, G. N., Vagin, A. A., and Dodson, E. J. (1997) Refinement of macromolecular structures by the maximum-likelihood method. *Acta Crystallogr D* **53**, 240-255

26. Adams, P. D., Grosse-Kunstleve, R. W., Hung, L. W., Ioerger, T. R., McCoy, A. J., Moriarty, N. W., Read, R. J., Sacchettini, J. C., Sauter, N. K., and Terwilliger, T. C. (2002) PHENIX: building new software for automated crystallographic structure determination. *Acta Crystallogr D Biol Crystallogr* **58**, 1948-1954

27. Krissinel, E., and Henrick, K. (2007) Inference of macromolecular assemblies from crystalline state. *J Mol Biol* **372**, 774-797

28. Schwarz, H., BNL Pulse Radiolysis Program. Brookhaven National Laboratory

29. Arroyo-Reyna, A., Tello-Solis, S. R., and Rojo-Dominguez, A. (2004) Stability parameters for one-step mechanism of irreversible protein denaturation: a method based on nonlinear regression of calorimetric peaks with nonzero deltaCp. *Anal Biochem* **328**, 123-130

30. Barnese, K., Sheng, Y., Stich, T. A., Gralla, E. B., Britt, R. D., Cabelli, D. E., and Valentine, J. S. (2010) Investigation of the highly active manganese superoxide dismutase from Saccharomyces cerevisiae. *J Am Chem Soc* **132**, 12525-12527

31. Borgstahl, G. E., Parge, H. E., Hickey, M. J., Johnson, M. J., Boissinot, M., Hallewell, R. A., Lepock, J. R., Cabelli, D. E., and Tainer, J. A. (1996) Human mitochondrial manganese superoxide dismutase polymorphic variant Ile58Thr reduces activity by destabilizing the tetrameric interface. *Biochemistry* **35**, 4287-4297

32. Hsieh, J. Y., Chen, S. H., and Hung, H. C. (2009) Functional roles of the tetramer organization of malic enzyme. *J Biol Chem* **284**, 18096-18105

33. Muren, E. M., Suciu, D., Topping, T. B., Kumamoto, C. A., and Randall, L. L. (1999) Mutational alterations in the homotetrameric chaperone SecB that implicate the structure as dimer of dimers. *Journal of Biological Chemistry* **274**, 19397-19402

34. Wichmann, C., Becker, Y., Chen-Wichmann, L., Vogel, V., Vojtkova, A., Herglotz, J., Moore, S., Koch, J., Lausen, J., Mantele, W., Gohlke, H., and Grez, M. (2010) Dimer-tetramer transition controls RUNX1/ETO leukemogenic activity. *Blood* **116**, 603-613

35. Shishova, E. Y., Di Costanzo, L., Cane, D. E., and Christianson, D. W. (2007) X-ray crystal structure of aristolochene synthase from Aspergillus terreus and evolution of templates for the cyclization of farnesyl diphosphate. *Biochemistry* **46**, 1941-1951

36. Whittaker, M. M., and Whittaker, J. W. (1997) Mutagenesis of a proton linkage pathway in Escherichia coli manganese superoxide dismutase. *Biochemistry* **36**, 8923-8931

37. Greenleaf, W. B., Perry, J. J., Hearn, A. S., Cabelli, D. E., Lepock, J. R., Stroupe, M. E., Tainer, J. A., Nick, H. S., and Silverman, D. N. (2004) Role of hydrogen bonding in the active site of human manganese superoxide dismutase. *Biochemistry* **43**, 7038-7045

38. Hearn, A. S., Fan, L., Lepock, J. R., Luba, J. P., Greenleaf, W. B., Cabelli, D. E., Tainer, J. A., Nick, H. S., and Silverman, D. N. (2004) Amino acid substitution at the dimeric interface of human manganese superoxide dismutase. *Journal of Biological Chemistry* **279**, 5861-5866

39. Mizuno, K., Whittaker, M. M., Bachinger, H. P., and Whittaker, J. W. (2004) Calorimetric studies on the tight binding metal interactions of Escherichia coli manganese superoxide dismutase. *J Biol Chem* **279**, 27339-27344

40. Potter, S. Z., Zhu, H., Shaw, B. F., Rodriguez, J. A., Doucette, P. A., Sohn, S. H., Durazo, A., Faull, K. F., Gralla, E. B., Nersissian, A. M., and Valentine, J. S. (2007) Binding of a single zinc

ion to one subunit of copper-zinc superoxide dismutase apoprotein substantially influences the structure and stability of the entire homodimeric protein. *J Am Chem Soc* **129**, 4575-4583

41. Bjork, A., Mantzilas, D., Sirevag, R., and Eijsink, V. G. (2003) Electrostatic interactions across the dimer-dimer interface contribute to the pH-dependent stability of a tetrameric malate dehydrogenase. *FEBS Lett* **553**, 423-426

42. Bjork, A., Dalhus, B., Mantzilas, D., Sirevag, R., and Eijsink, V. G. (2004) Large improvement in the thermal stability of a tetrameric malate dehydrogenase by single point mutations at the dimer-dimer interface. *J Mol Biol* **341**, 1215-1226

43. Appaji Rao, N., Ambili, M., Jala, V. R., Subramanya, H. S., and Savithri, H. S. (2003) Structure-function relationship in serine hydroxymethyltransferase. *Biochim Biophys Acta* **1647**, 24-29

44. Levy, E. D., Boeri Erba, E., Robinson, C. V., and Teichmann, S. A. (2008) Assembly reflects evolution of protein complexes. *Nature* **453**, 1262-1265